



Fabrication of Aluminium Nanostructure for Visible to Ultraviolet Plasmonics

Feifei Zhang

► To cite this version:

Feifei Zhang. Fabrication of Aluminium Nanostructure for Visible to Ultraviolet Plasmonics. Micro and nanotechnologies/Microelectronics. Université de Technologie de Troyes, 2018. English. NNT : 2018TROY0011 . tel-03202328

HAL Id: tel-03202328

<https://theses.hal.science/tel-03202328>

Submitted on 19 Apr 2021

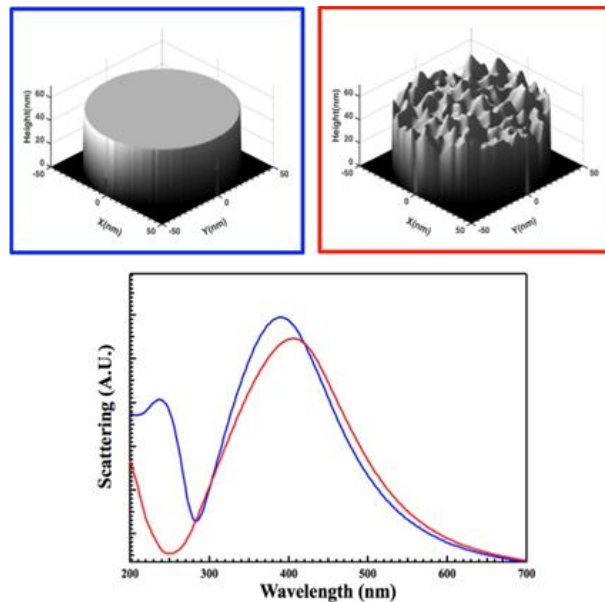
HAL is a multi-disciplinary open access archive for the deposit and dissemination of scientific research documents, whether they are published or not. The documents may come from teaching and research institutions in France or abroad, or from public or private research centers.

L'archive ouverte pluridisciplinaire **HAL**, est destinée au dépôt et à la diffusion de documents scientifiques de niveau recherche, publiés ou non, émanant des établissements d'enseignement et de recherche français ou étrangers, des laboratoires publics ou privés.

Thèse
de doctorat
de l'UTT

Feifei ZHANG

Fabrication of Aluminum Nanostructure for Visible to Ultraviolet Plasmonics



Spécialité :
Matériaux, Mécanique, Optique et Nanotechnologie

2018TROY0011

Année 2018

THESE

pour l'obtention du grade de

DOCTEUR de l'UNIVERSITE DE TECHNOLOGIE DE TROYES

Spécialité : MATERIAUX, MECANIQUE, OPTIQUE ET NANOTECHNOLOGIE

présentée et soutenue par

Feifei ZHANG

le 25 avril 2018

Fabrication of Aluminum Nanostructure for Visible to Ultraviolet Plasmonics

JURY

M. P.-M. ADAM	PROFESSEUR DES UNIVERSITES	Président
Mme A.-L. BAUDRION-BÉAL	MAITRE DE CONFERENCES	Examinateur
M. N. FELIDJ	PROFESSEUR DES UNIVERSITES	Rapporteur
Mme M. FLEISCHER	JUNIORPROFESSORIN	Examinateur
M. M. KOCIAK	DIRECTEUR DE RECHERCHE CNRS	Membre du Jury
M. J. MARTIN	ENSEIGNANT CHERCHEUR UTT	Directeur de thèse
M. J. PLAIN	PROFESSEUR DES UNIVERSITES	Directeur de thèse
M. H. RINNERT	PROFESSEUR DES UNIVERSITES	Rapporteur

Acknowledgements

In my favourite science fiction *The three-body problem*, one of the scientific areas in which the three-body aliens want to prevent the development of human beings is nanoscience and nanotechnology. As a member of Laboratoire de Nanotechnologie et d'Instrumentation Optique (LNIO), now Lumière, Nanomatériaux, Nanotechnologies (L2N), I am so honoured to have a contribution to this area, even if it is only a nanobrick to protect our earth planet. Without the great support from my two supervisors Prof. Dr. Jérôme PLAIN and Dr. Jérôme MARTIN, I would never make it today. I still remember how helpless it was for me as a foreigner during the initial period in France. It was their humor and easygoing that helped me integrate into the group fast. And thanks for their patience, wisdom, and thoughtful guidance during the past years, I always feel much stronger with them.

I should really thank Prof. Hervé RINNERT and Prof. Nordin FELIDJ to give me such a great honor for accepting as my reviewers. And thank Dr. Mathieu KOPIAK, Dr. Anne-Laure BAUDRION BÉAL, and Prof. Pierre Michel ADAM to be the members of my jury. Thanks for all the questions and advice from my jury, and I really learnt a lot from them. I also would like to express my gratitude to Davy, Julien, and Pierre for their cooperative work and inspiring discussions. Thank Anna, Jeremie, Serguei, and Régis for their technical assistances and their trainings of instruments. They are always so helpful to save me from a mess during my experiments.

Special gratitude goes to my research partner Feng Tang for his help in FDTD simulations and fruitful discussion no matter in days or late nights. Thanks a lot to Jiyong Wang and Fang Dai for the inspiring discussion. Thanks Yinping Zhang for helping me during the desperate period of AFM measurement, and I wish that I could forget that miserable memory very soon. I also wish to thank all the colleagues in the L2N to make our lab such a great team full of wisdom and fun. Thank Dimitry, Fred, Lina, Ricardo, Sobhi, Abdo, Ali, Avril, Yi Huang, Binbin Wang, Yunlong Zhu, Xiaolun Xu, Yubing Pu, Quan Liu, Dandan Ge, Lan Zhou and the others more for their help and friendship in the daily life. Thanks to all my Chinese friends

in UTT like Nan Zhang, Yongjian Xue, Dongqing Liu, Chuan Zhang, Shijie Zhu, and Xiaoyi Chen, for their companions during the past years in France. We have so many fabulous meomories together in Troyes, and I will never forget in my life. Special thanks should be given to CSC for funding my PhD study in France.

Finally, I want to thank my parents and my lovely little sister Bingyi. I love you all and you are always the energy for me to march forward without fear and hesitation.

Abstract

Nowadays, the growing interest and demand in the ultraviolet (UV) plasmonic fascinate aluminium (Al), because the popular gold and silver no longer exhibit plasmonic response exceeding visible range to UV range. Additionally, Al is cheap, abundant, non-toxic, and compatible with the complementary metal-oxide-semiconductor technology. Up to now, Al nanoparticles have already been found numerous applications including UV-SERS, nonlinear optics, enhanced fluorescence, optoelectronics, plasmonic-assisted lasing, photocatalysis, and structural colors. In this thesis, we are aiming to study several vital factors affecting the localized surface plasmonic resonances of Al nanoparticles including the oxidation, rapid thermal annealing, surface roughness, and uniform disorder. The contents are arranged as followed:

In Chapter 1, we review the main theoretical concepts of nanoplasmonics and the motivation of Al plasmonics. Then, a comprehensive summary of Al plasmonics to various applications is given. In Chapter 2, we include a studying of the stability of Al nanoparticles exposed to the environment of air and water. In Chapter 3, we introduce a research on the influence of rapid thermal annealing to Al plasmonic resonances. In Chapter 4, we reveal the importance of surface roughness to Al plasmonic resonance. In Chapter 5, we discuss about Al plasmonic resonances from three kinds of uniformly disordered Al nanoparticle array (displacement disorder, size disorder, and rotation disorder). In Chapter 6, we outline some promising applications of completed work. The experimental and numerical methods used in the whole thesis are provided as an appendix in detail. Lastly, an extended French summary is also included.

Contents

Acknowledgements	I
Abstract	III
Contents.....	IV
Chapter 1 Introduction	1
1.1. Plasmonic fundamental	1
1.1.1. Maxwell's equations	1
1.1.2. Drude-Lorentz model	2
1.1.3. Localized surface plasmon	3
1.1.4. Conditions of plasmonic resonance for nanoparticles.....	4
1.1.5. Surface plasmon polaritons	5
1.2. The choice of material for ultraviolet plasmonic.....	6
1.3. Aluminium oxidation	8
1.4. Surface roughness	10
1.5. Aluminium plasmonic applications	11
1.5.1. SERS	12
1.5.2. Enhanced fluorescence	13
1.5.3. Color printing	15
1.5.4. Other applications	16
Chapter 2 Long-term stability of aluminium nanoparticles.....	18
2.1. Model to simulate the oxidation.....	18
2.2. Calculated extinction spectra	20
2.3. Long-time experimental measurement.....	22
2.4. Corrosion in water	26
2.5. Conclusions	27
Chapter 3 Rapid thermal annealing for the improvement of Al nanoparticles plasmonic properties	29
3.1. Blueshifted plasmonic resonance after low temperature RTA	29
3.2. Extinction spectra after RTA treatments.....	30
3.3. TEM measurement and Q-factor	32
3.4. Oxidation after high temperature RTA	35

3.5. Evolution of morphology	36
3.5.1. SEM measurement	37
3.5.2. AFM measurement.....	38
3.6. Conclusions	39
Chapter 4 Surface roughness and substrate induced symmetry-breaking: influence on plasmonic properties of Al nanoparticle arrays	40
4.1. General difficulties to study the influence of roughness	40
4.2. Methods to model the surface roughness	41
4.3. Roughness effect on isolated nanodisk	43
4.4. Substrate influence and Fano lineshape.....	44
4.5. Generalization to periodic arrays	48
4.5.1. Coupling of modes in periodic array.....	48
4.5.2. Experiments: pitch 200 nm	51
4.5.3. Experiments: pitch 250 nm	54
4.5.4. Experiments: pitch 400 nm	55
4.6. Conclusions	57
Chapter 5 Plasmonic resonances of uniformly disordered aluminium nanoparticle arrays	59
5.1. How to generate uniform disorder?	60
5.1.1. Sample fabrication.....	60
5.1.2. Rules to name the samples	61
5.2. Large-area FDTD Calculations	61
5.2.1. Uniform disorder	62
5.3. Displacement disorder	63
5.3.1. Periodic array	64
5.3.2. Radial distribution function.....	65
5.3.3. Influence on optical properties	67
5.3.4. Investigation on the array with different pitch	69
5.4. Size disorder	70
5.4.1. Influence on optical properties	70
5.4.2. Investigation on the array with different pitch	71
5.5. Rotation disorder	72
5.5.1. Extinction spectra.....	72
5.5.2. Electric field distribution.....	74
5.6. Conclusions	75

Chapter 6 Summary and outlook.....	76
Methods	80
a. Electron beam lithography process.....	80
b. Rapid thermal annealing treatment.....	81
c. SEM and TEM measurement	81
d. Atomic force microscopy measurements.....	81
e. Extinction spectra measurement	82
f. FDTD simulation	82
Résumé	84
1. Introduction	84
2. Stabilité des nanoparticules d'aluminium	86
2.1 Modèle pour simuler l'oxydation des nanostructures en aluminium.....	86
2.2 Résultats de la simulation.....	87
2.3 Résultats expérimentaux sur la stabilité	89
3. Amélioration des propriétés plasmoniques de NP d'Aluminium par recuit rapide.....	91
3.1 Spectres d'extinction	91
3.2 Interprétation des spectres d'extinction	92
3.3 Réduction du nombre de joints de grains	93
3.4 Amélioration du facteur de qualité.....	94
3.5 Recuit à haute température ($> 400^{\circ}\text{C}$).....	95
3.6 Caractérisation par MEB	95
4. Influence de la rugosité de surface les résonances plasmoniques de NP d'aluminium	96
4.1 Rugosité sur une nanoparticule isolée	97
4.2 Effet du substrat sur les résonances d'un nanodisque isolé.....	98
4.3 Effet de la rugosité de surface	99
4.4 Réseau de nanocylindres d'Al avec un pas de 200 nm	100
5. Résonances plasmoniques de réseaux de nanoparticules d'Al uniformément désordonnées	102
5.1 Méthode pour introduire le désordre	102
5.2 Etude du désordre sur la position de nanostructures	104
5.3 Etude du désordre sur les dimensions des nanostructures.....	107
5.4 Etude du désordre sur la rotation des nanostructures	108
6. Conclusion.....	110
References	112

Chapter 1 Introduction

In this chapter, an introduction to the fundamental theories of plasmonics and various contents of aluminium plasmonics are presented. First, we begin with the concept of dielectric function from Maxwell's equations, and two important plasmonic features including the localized surface plasmon and surface plasmon polaritons. Then, we introduce the choice of ultraviolet plasmonic material. Next, we focus on two important issues of aluminium plasmonics including the oxidation process and the influence of surface roughness. Finally, various important applications of aluminium plasmonics are summarized.

1.1. Plasmonic fundamental

1.1.1. Maxwell's equations

Metallic nanoparticles (NPs) sustain coherent oscillations of their conduction electrons in response to the incident light. These oscillations are called localized surface plasmon resonances (LSPR). When the incident light matches the resonance wavelength, LSPR will result in a local field enhancement around the NP. This effect allows the confinement and manipulation of electromagnetic waves at the nanoscale. Meanwhile, the resonant wavelength of LSPR depends on the constituting metal, size, shape, and surrounding medium of NPs. These interesting properties lead to numerous fields of research with very different backgrounds, including surface enhanced Raman spectroscopy (SERS), metal enhanced fluorescence, and solar energy harvesting, as we will see in the last section of [Chapter 1](#).

Since plasmonic is actually a study of the interaction between light and metals, it can be thoroughly understood with electromagnetics, thanks to Maxwell's equations¹:

$$\nabla \cdot \vec{D} = \rho \quad (1-1a)$$

$$\nabla \cdot \vec{B} = 0 \quad (1-1b)$$

$$\nabla \times \vec{E} = -\frac{\partial \vec{B}}{\partial t} \quad (1-1c)$$

$$\nabla \times \vec{H} = \vec{J} + \frac{\partial \vec{D}}{\partial t} \quad (1-1d),$$

where \vec{D} , \vec{E} , \vec{B} and \vec{H} stand for the electric displacement, the electric field, the magnetic induction, and the magnetic field respectively with current density \vec{J} and time t . The \vec{D} , \vec{E} , \vec{B} and \vec{H} are further linked via the polarization \vec{P} and magnetization \vec{M} by

$$\vec{D} = \epsilon_0 \vec{E} + \vec{P} \quad (1-2a)$$

$$\vec{H} = \frac{1}{\mu_0} \vec{B} - \vec{M} \quad (1-2b).$$

For linear and isotropic materials,

$$\vec{D} = \epsilon_0 \epsilon \vec{E} \quad (1-3a)$$

$$\vec{B} = \mu_0 \mu \vec{H} \quad (1-3b),$$

where ϵ_0 and μ_0 are the electric permittivity and magnetic permeability of vacuum respectively. Additionally, ϵ is named as the dielectric constant, and μ is named as the relative permeability. For the nonmagnetic medium, $\mu = 1$. Now, to solve Maxwell's equations in various situations, the complex dielectric function of the material $\epsilon = \epsilon_1 + i\epsilon_2$, which is frequency dependent, becomes the essential parameter to describe the plasmonic phenomena. The real part ϵ_1 represents the degree of polarization inside the material when it is subjected to an electric field. The imaginary part ϵ_2 quantifies the loss of electromagnetic wave in the medium.² In experiments, ϵ can be obtained via the ellipsometry. Theoretically, it has been widely described by Drude-Lorentz model over a large frequency range, which will be discussed in the next section.

1.1.2. Drude-Lorentz model

Drude-Lorentz model is a classical free electron gas model used to study the optical response of metals. Since that the nucleus of the atom is much more massive than the electrons, it is assumed that when light impinges on the metal, only electrons move around the fixed nucleus. Then we can use the model of a damped harmonic oscillator to depict the situation where light interacts with electrons of metal. The damping terms from collisions and radiations of the accelerating electrons are represented by the damping factor γ . Additionally, the interband

Chapter 1

transitions are described as a bound electron with the natural resonance frequency ω_0 . When applying an harmonic time dependent electric field $\vec{E} = \vec{E}_0 e^{-i\omega t}$, the electron (q) movement can be then described as³:

$$m \frac{d^2 \vec{x}}{dt^2} + m\gamma \frac{d\vec{x}}{dt} + m\omega_0^2 \vec{x} = -q\vec{E} \quad (1-4)$$

On the left of [Equation 1-4](#), the first term stands for the acceleration force; the second term stands for the frictional force of damping, while the third term represents the restoring force. The solution of this equation is

$$\vec{x} = -\frac{q}{m} \frac{\vec{E}}{\omega_0^2 - \omega^2 - i\omega\gamma} \quad (1-5).$$

With the free electrons of number density n , the displaced electrons contribute to the macroscopic polarization

$$\vec{P} = -nq\vec{x} \quad (1-6).$$

Combining [Equation 1-2a](#) with [Equation 1-5](#) and [Equation 1-6](#),

$$\vec{D} = \epsilon_0 \left(1 + \frac{\omega_p^2}{\omega_0^2 - \omega^2 - i\omega\gamma} \right) \vec{E} \quad (1-7),$$

where the plasma frequency ω_p of the free electron gas is defined as

$$\omega_p^2 = \frac{nq^2}{m\epsilon_0} \quad (1-8).$$

Now, comparing with [Equation 1-3a](#) we come to find the dielectric function

$$\epsilon(\omega) = 1 + \frac{\omega_p^2}{\omega_0^2 - \omega^2 - i\omega\gamma} \quad (1-9a).$$

This gives $\epsilon_1 = 1 + \frac{\omega_p^2(\omega_0^2 - \omega^2)}{(\omega_0^2 - \omega^2)^2 + \gamma^2\omega^2}$ $(1-9b)$

$$\epsilon_2 = \omega_p^2 \frac{\gamma\omega}{(\omega_0^2 - \omega^2)^2 + \gamma^2\omega^2} \quad (1-9c).$$

When considering the background due to the response of nucleus and eliminating ω_0 , [Equation 1-9a](#) becomes what is called Drude model,

$$\epsilon(\omega) = \epsilon_\infty - \frac{\omega_p^2}{\omega^2 + i\omega\gamma} \quad (1-10).$$

If multiple interband transitions exist, [Equation 1-9a](#) can be adapted to

$$\epsilon(\omega) = \epsilon_\infty + \sum_m \frac{f_m \omega_p^2}{\omega_m^2 - \omega^2 - i\omega\Gamma_m} \quad (1-11),$$

where f_m is the oscillator strength of the transition at ω_m with damping factor Γ_m .

1.1.3. Localized surface plasmon

When light wave incidents on a metallic NP, the electron cloud will be displaced periodically by the electric field of light wave. The separated positive charge (nucleus) and negative charge (electrons) attract each other and thus result in the restoring force. The quantum of this collective electron oscillation is named plasmon, just like the definition of phonon to the lattice vibration. The schematic of this concept is depicted in Figure 1.1a. The plasmonic effect on the metallic NP is usually called localized because of the non-propagating feature owing to the restriction of NP to electrons. Localized surface plasmon fascinates metallic NPs with the ability to support the confinement and enhancement of electromagnetic wave into sub-wavelength volume, resulting in so-called hot spots near the nanostructures. As exemplified in Figure 1.1b, a vicinity with enhanced electric field is formed around the nanostructure with bright hot spots formed on the corners of NP. This is actually the foundation of many applying fields of nanoplasmonics like SERS, as we will see.

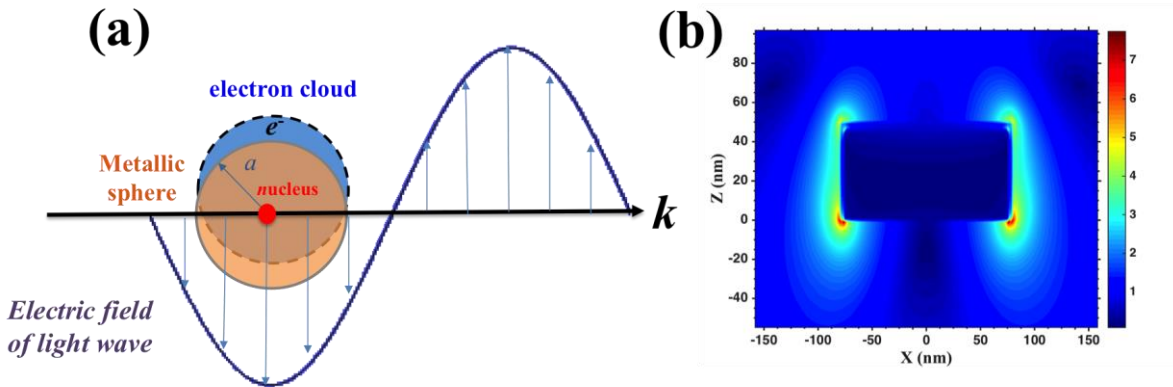


Figure 1.1. (a) Schematic of localized surface plasmon. (b) Electric field distribution of Al NP calculated by FDTD. The colorbar stands for the electric field intensity.

1.1.4. Conditions of plasmonic resonance for nanoparticles

To analyse the conditions of plasmonic resonance, electrostatic approximations are regularly used to derive an analytical formula with relatively good accuracy for a small metallic sphere of radius a ($a \ll \lambda$, λ is the wavelength of light). Thus, the scattering (C_{sca}) and absorption (C_{abs}) cross sections can be determined from³:

$$C_{sca} = \frac{8\pi}{3} k^4 a^6 \left| \frac{\epsilon - \epsilon_d}{\epsilon + 2\epsilon_d} \right|^2 \quad (1-12a)$$

Chapter 1

$$C_{abs} = 4\pi k a^3 \operatorname{Im} \left[\frac{\varepsilon - \varepsilon_d}{\varepsilon + 2\varepsilon_d} \right] \quad (1-12b),$$

where \mathbf{k} is the wavevector of the incident wave, and ε_d is the dielectric function of the surrounding medium. Moreover, the plasmonic resonance is usually described by the extinction cross section $C_{ext} = C_{sca} + C_{abs}$.

It is apparent that the resonance will occur when the denominator of [Equation 1-12](#) becomes zero *i.e.* $\operatorname{Re}(\varepsilon) = -2\varepsilon_d$. This explains why the plasmonic resonance of NP is sensitive to the local dielectric environment, since that a change of ε_d will alter the value of ε to match the condition. This is actually the basic idea of using plasmonic resonances for refractive index sensing.⁴ For most dielectrics, the value of ε_d is usually larger than zero, which indicates that the real part ε_1 of the metallic material should be less than zero to meet the criterion. For bigger NPs, the retardation effects due to the variations in the amplitude and phase of electromagnetic field result in a redshifted resonance.⁵ As for NPs with different shapes, the denominators of [Equation 1-12](#) will be changed, leading to the different resonance condition. However, these conditions are always linked to the negative real part of ε . Meanwhile, the strength of resonance depends on the imaginary part of ε . Therefore, to obtain an excellent plasmonic performance at certain wavelength, the material is generally expected to have a negative value in the real part and relatively small value in the imaginary part of dielectric function. In brief, the plasmonic resonance of the metallic NP is a function of the size, shape, and type of metal, as well as the environment. This gives a great flexibility to manipulate the optical properties of metallic NPs.

1.1.5. Surface plasmon polaritons

In contrast to the mode of localized surface plasmon supported by nanoparticles, the metal-dielectric interface supports a propagating plasmonic mode known as surface plasmon polaritons (SPP).⁶ It is essentially the coupling between photons and the collective oscillations of electron *i.e.* plasmon. [Figure 1.2](#) gives the basic concepts of SPP. First of all, SPP is a transverse magnetic wave of which the magnetic field is perpendicular to its wavevector \mathbf{k}_{spp} . Meanwhile, the generation of surface charge requires an electric field normal to the surface. From [Figure 1.2b](#), it can be seen that the electric field is enhanced near the interface and

decayed exponentially with distance away from it. This reflects that SPP is evanescently decayed in the direction perpendicular to the planar metallic surface. It prevents the power from propagating away from the interface and finally confines SPP in the plane of the interface between metal and dielectric. This also induces the definition of skin depth δ_m , which means the penetration length of electromagnetic wave into metal (the field falls to $1/e$). For example, the value of aluminium is about 13 nm over the optical region.⁷

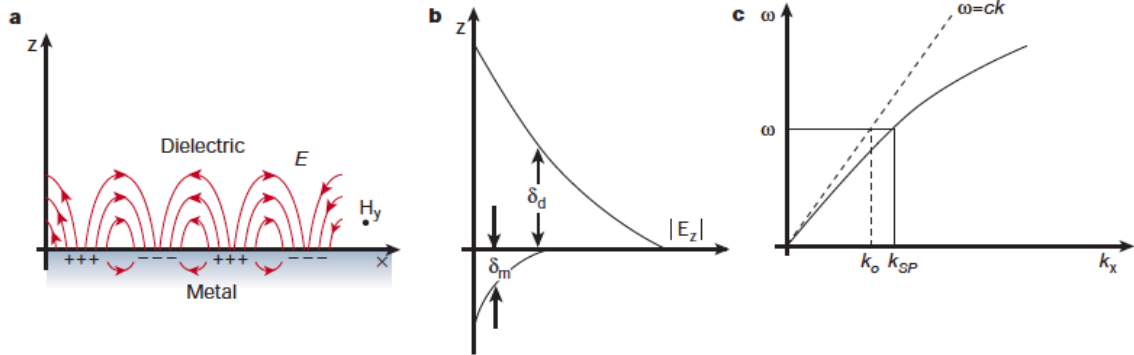


Figure 1.2. (a) Schematic of SPP with illustrating the surface charge distribution. H is in the y direction. (b) The electric field intensity with distance away the interface. (c) The dispersion curve for a SPP mode shows the momentum mismatch problem.⁸

The wavevector of SPP ($k_{SPP} = \frac{2\pi}{\lambda_{SPP}}$, λ_{SPP} is the wavelength of SPP mode) is given by³

$$k_{SPP} = k_0 \sqrt{\frac{\epsilon_m \epsilon_d}{\epsilon_m + \epsilon_d}} \quad (1-13),$$

where ϵ_m and ϵ_d are the dielectric functions of metal and dielectric respectively, k_0 is the free-space wavevector ($k_0 = \frac{2\pi}{\lambda_0}$, λ_0 is the wavelength of light in free space). The square root term in Equation 1-13 is usually greater than one, which means that the wavevector of SPP mode is greater than that of light. Therefore, as shown in Figure 1.2c, the freely propagating light is unable to couple to SPP mode due to the mismatch of wavevector. Usually, methods like prism coupling, grating coupling and near-field excitation are generally applied for matching the momentum.³ The waveguiding feature of SPP can be employed in a variety of fascinating system, to name a few, for the integration of plasmonic components for sensing and for efficient single-photon source.^{9,10,11}

1.2. The choice of material for ultraviolet plasmonic

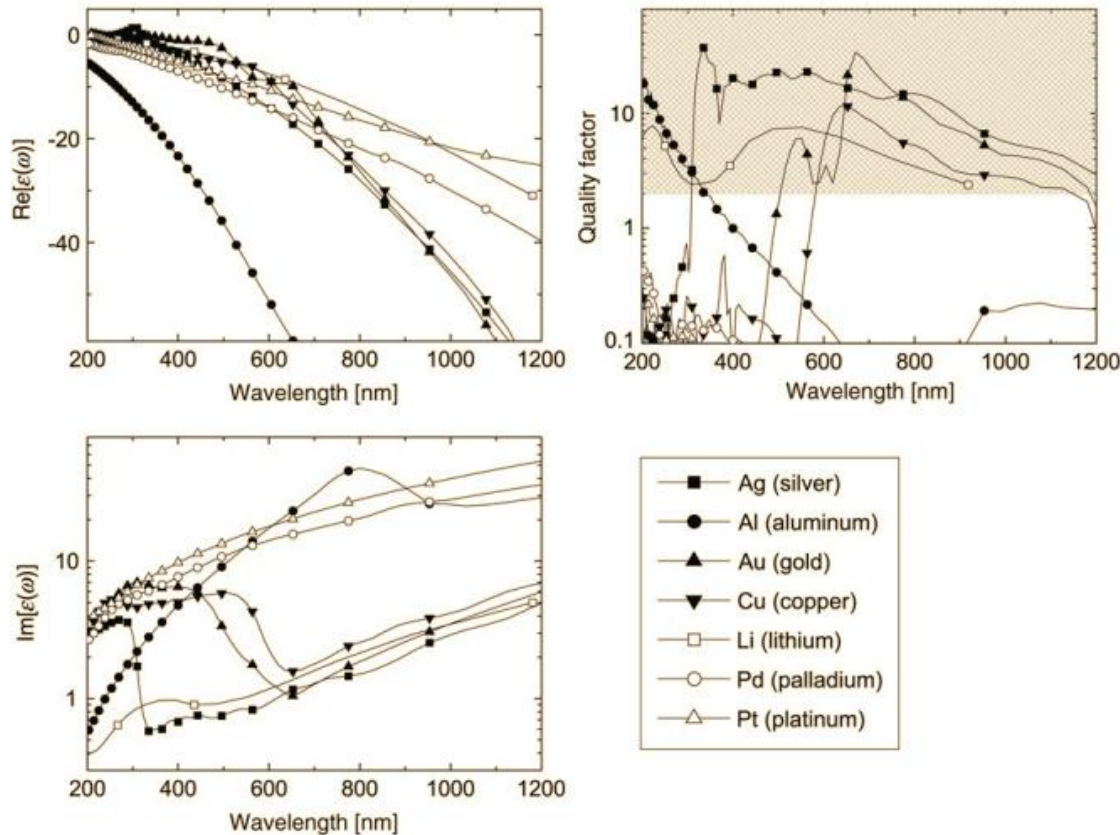


Figure 1.3. Comparison of the dielectric function ϵ for various metals. The real part ϵ_1 (top) and imaginary part ϵ_2 (bottom) are plotted as a function of wavelength on the left. The top-right figure shows the predicted quality factor Q calculated by $Q = \frac{\omega(d\epsilon_1/d\omega)}{2(\epsilon_2(\omega))^2}$. The shaded area with high Q is of interest to many plasmonic applications.¹²

Up to now, NPs made of noble metals, typically like Au and Ag, have been investigated thoroughly, due to their excellent plasmonic performance in the visible and infrared region. Nevertheless, future applications will require the extension of plasmonics toward lower wavelengths, particularly in the ultraviolet (UV) range. Actually, aluminium (Al) has been known for a long time to exhibit plasmonic properties, as it is the metal on which the surface plasmon was firstly evidenced back in the 1950s.¹³ However, it is only in recent years that a significant number of papers started to develop what is now called “aluminium plasmonics”.¹⁴ The main reason behind this regain of interest stems from the excellent optical properties of aluminium in the UV spectrum, a region where the classical plasmonic metals (i.e., gold and silver) cannot be used. As shown in Figure 1.3, gold does not exhibit plasmonic resonances at

wavelengths shorter than 520 nm due to its interband transitions. Silver nanostructures exhibit plasmonic resonances down to the very near UV (350 nm) but suffer from the strong oxidation and lose their plasmonic properties over time. Another major interest of aluminium as a plasmonic material lies in its broadband nature: Apart from a small region around $\lambda = 800$ nm (corresponding to the interband transition near 1.4 ev), aluminium sustains plasmonic resonances from the infrared to the deep-UV.¹⁵ As a result of the negative dielectric constant at UV wavelengths (down to 80 nm) while keeping a relatively low loss coefficient, aluminium is one of the most appealing metal for pushing nanoplasmatics up to UV energies. Beside Al, various other metals like gallium (Ga), indium (In), lead (Pb), tin (Sn), and magnesium (Mg) have also been proposed to be applicable candidates for UV plasmonic materials.^{16,17}

Additionally, aluminium is cheap and abundant, since it is the third most abundant element on the earth. Meanwhile, aluminium is industrially recyclable and its nontoxicity indicates the potentiality in the bio-applications. Last but not the least, the compatibility with metal-oxide-semiconductor (CMOS) technology is also a key factor, which paves the way to the massive industrial production. Surely, Al also endures the oxidation like Ag, however Al does not oxidize in depth as it naturally forms a few nanometers thick self-protecting oxide layer, making it chemically stable in time.¹⁸ The Al oxidation process will be discussed in detail in the next section.

1.3. Aluminium oxidation

Because of the wide use of Al particles as solid propellants and explosives, the oxidation process of Al NPs has been investigated intensively since last century.¹⁹ It is well known that Al suffers from an unavoidable oxidation process. When exposed to air, Al surface oxides quickly, resulting in a 2-5 nm amorphous passivated layer. This has been proved by many previous researches. As shown in [Figure 1.4](#), the transmission electron microscope (TEM) images show the native oxide layer outside Al NPs with normal thickness about 2-5 nm. This natural oxidation process is deemed as self-terminating because the formed oxide layer will prevent the further penetration of oxygen. To further prevent the natural oxidation and improve the stability, effective surface passivation agents like transition metal and organic

Chapter 1

coating were studied in the wet-chemical method.^{20,21} A detailed investigation of the natural stability of Al NPs will be given in the [Chapter 2](#).

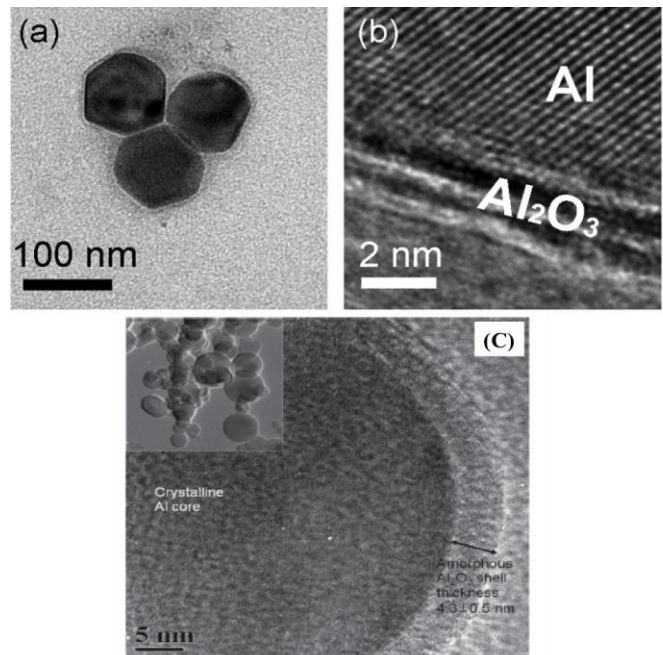


Figure 1.4. TEM measurement of the native oxide layer of Al NP from reference [22] for (a) and (b), and reference [23] for (c).

Moreover, Al NPs during the fabricating process or the applications are always exposed to the environment at varying temperatures. Therefore, the stability of Al NPs at different temperatures is also a critical issue. Actually, owing to the interest on propellants, the thermal oxidation procedure of Al NPs at different temperatures has been studied in depth for many years, and one representative result is shown in [Figure 1.5](#). The process could be summarized as followed. After the annealing at low temperature (below 400 °C), the natural oxide layer will keep amorphous, while the thickness of oxide layer remains almost constant.²⁴ At about 500 °C, the crystalline oxide $\gamma\text{-Al}_2\text{O}_3$ is nucleated at the metal-oxide interface at low rate. Meanwhile, this crystallization gives rise to the slightly increased thickness of oxide layer (about 10 nm).²⁵ At about 600 °C, more Al_2O_3 crystalline phases are formed at relatively huge rate resulting in a greatly increased Al_2O_3 thickness.²⁶ It is also suggested that the different coefficients of linear expansion between the oxide and metal phases would result in the formation of cracks in the oxide layer, which further brings a higher rate of diffusion.²³ In all, the Al_2O_3 thickness during Al oxidation does not increase linearly with the annealing

temperature. The response of Al plasmonic resonance to the varying annealing temperatures will be fully discussed in the [Chapter 3](#).

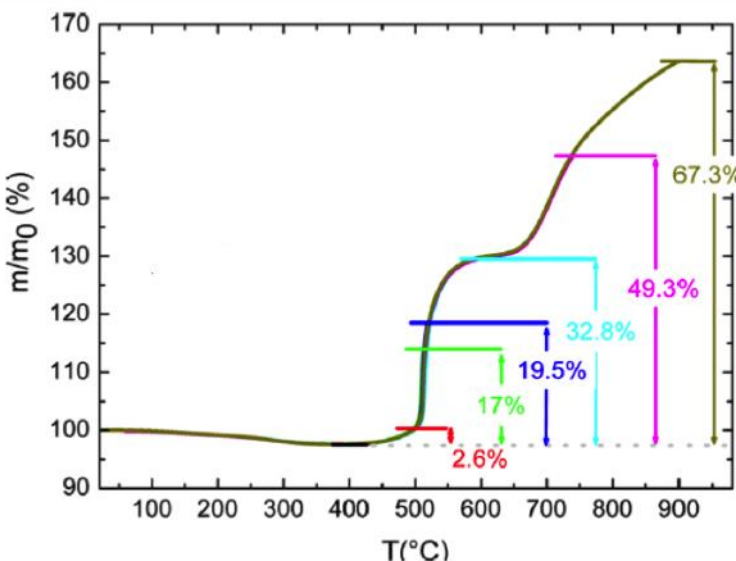


Figure 1.5. Thermogravimetry analyses of 100 nm Al powders. The number in % corresponds to the mass gain associated with each sample preparation.²⁵

1.4. Surface roughness

Another extremely important factor affecting the plasmonic properties of metallic NPs is the surface roughness. Especially, the NPs made by electron beam lithography (EBL) are observed to have a rougher surface than the chemical synthesized NPs. In particular, this issue is even critical for Al than Au. Generally, gold NPs deposited by the thermal evaporation method during the EBL procedure have the root-mean-square (RMS) value of top surface around 1 nm.²⁷ However, this value increases to about 5 nm for Al.¹⁸ The increment might be attributed to the smaller density and the polycrystallinity of Al material compared to Au material. In some occasion, the surface roughness might be preferred. For instance, roughened metallic surface were found to give a tremendous enhancement on the SERS effect.²⁸ Otherwise, roughened surface morphology always deteriorates the plasmonic properties. Numerous investigations have shown that the surface roughness can sensibly degrade the optical properties of nanostructures, such as the performance of nanolaser^{29,30}, nonlinear optics³¹ and so on.

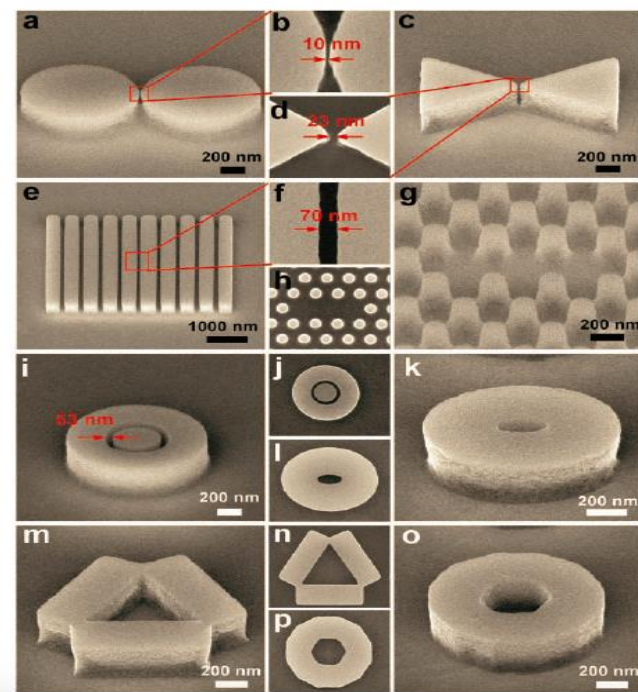


Figure 1.6. SEM images of various silver nanostructures fabricated by template stripping method. The height of all the patterns is 300 nm.³²

To obtain the smooth surface, one effective technique to improve the flatness of patterned nanostructures is the template stripping method, which exploits adequately the flatter surface of substrates including mica and silicon.³² The typical morphology with ultrafine top surface improved by this method is shown by the scanning electron microscope (SEM) images in Figure 1.6. Other experimental methods have also been proposed to obtain the ultrasmooth surface.^{33,34,35} However, the improved surface quality is regularly at the expense of the cost, time consuming, and higher requirement of advanced equipment. Therefore, theoretical analysis on the influence of surface roughness becomes extremely important. An extensive study of the influence of top surface roughness on Al plasmonic resonance will be introduced in the Chapter 4.

1.5. Aluminium plasmonic applications

Al plasmonics have been demonstrated efficient for numerous potential applications including SERS, enhanced fluorescence, structural color, and photocatalysis. As a consequence, Al

plasmonics has emerged quite recently. In this section, some important applications will be exemplified in detail.

1.5.1. SERS

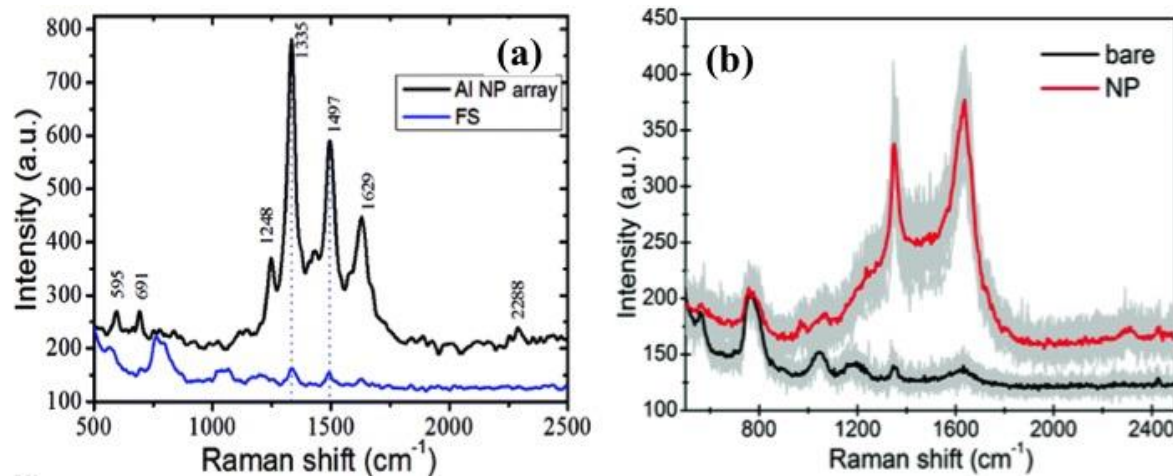


Figure 1.7. (a) Raman spectra of 1 nm Adenine layer sublimated onto fused silica (FS) and Al NP array.⁴⁰ (b) Raman spectra of TNT deposited on bare and Al NP array by drop coating.⁴¹

When molecules are located near the metallic NP's surface, the enhancement of the electromagnetic field due to the LSPR will give a great rise to the scattering of molecules and boost the Raman signal. The SERS enhancement factor is proportional to the fourth power of the local electric field intensity and proportional to the wavelength power minus four, which is therefore very interesting in the UV range.¹² This technique even can be used to detect a single molecule.^{12,36} Up to now, numerous SERS studies have been focused on the Au and Ag in the visible and near-infrared region. However, biomolecules such as DNA and proteins that absorb UV light enable Al plasmonic nanostructures operating in UV for the label-free detection of those biomolecules. On the other hand, most molecules do not fluoresce in the UV or deep-UV range, which brings about another advantage of the UV SERS as a result of the increased spatial resolution owing to the reduced fluorescent background.³⁷

During the SERS test of noble metals, one important process is the surface functionalization with traditionally used thiol or amine groups to facilitate the targeted molecules to bind with the metallic surface.³⁸ However, this could be hard for Al NP due to the existence of the

Chapter 1

nanoscale oxide layer. On the other hand, this oxide layer could also be turned into an advantage for shell-isolated nanoparticle enhanced Raman spectroscopy (SHINERS), and the oxide layer could also provide new binding sites for a variety of functional groups including carboxylic/ phosphoric acids, and silanes.³⁹ By utilizing the oxide-molecule binding through carboxyl and silane functional groups, Shu Tian and et al have studied the Al nanocrystal near-infrared SERS substrate for detecting single-stranded DNA under 785 nm excitation.³⁸ By avoiding the surface functionalization, Shankar et al reported the successful ultrasensitive detection of adenine and TNT as deep-UV SERS sensing on Al nanostructures excited at 257 nm, as shown in [Figure 1.7](#).^{40,41} Using Al film-over-nanosphere substrate (AlFON), Bhavya's results proved that AlFON supported plasmonic enhancement in the 200 - 400 nm range with total enhancement up to 10^5 - 10^7 range.⁴² Ximei Li et al fabricated a 3D Al hybrid nanostructured film using millisecond laser direct writing method (millisecond-pulsed Nd: YAG laser). By the simple drop-cast of crystal violet aqueous solution, the dense hot spots over a large area about 1 cm^2 were found to support the UV SERS enhancement with a six orders of magnitude.⁴³

Although Al still displays a plasmonic response in the visible range, it is predicted that Al is no longer suitable for the SERS application due to the smaller value of Q factor. As shown in [Figure 1.3](#), the calculated Q factor for Al is continuously decreased with wavelength in the visible range.¹² Raymond and et al studied experimentally the performance of Al nanocylinder for SERS in the visible range.⁴⁴ Measured Q factors from experimental extinction spectra showed much higher values than the theoretical calculation. However, no obvious Raman enhancement was observed in the visible range. Possible reasons might be due to the natural oxide layer outside Al NP, which prevents molecules from the near-field enhanced region. On the contrary, Klaus and et al have observed strong non-resonant SERS on the discontinuous nanostructured films excited at 785 nm.⁴⁵

1.5.2. Enhanced fluorescence

Surface plasmons can increase the density of states and the spontaneous emission rate, thus metallic enhanced fluorescence has been a classical application of plasmonics.⁴⁶ As shown in [Figure 1.8](#), by depositing a 10 nm aluminium layer above the InGaN light-emitting layer, a

sixfold enhancement of photoluminescence was obtained due to the coupling of electron–hole pairs excited within the quantum and the electron vibrations at the metal/semiconductor interface.⁴⁷ Cho C Y found that the output power of AlGaN-based ultraviolet light-emitting diodes was enhanced by 45% assisted by the surface plasmon of Al layer.⁴⁸ Al dimple arrays fabricated by focused-ion beam milling were found to have a broadband enhancement of the emission from CdSe/ZnS quantum dots.⁴⁹ Here, the natural oxide layer of Al NPs was supposed to prevent the emission quenching due to the contact of quantum dots with the metallic surfaces. The low radiative emission of biomolecules limits the use of the intrinsic fluorescence in biology and medicine.^{50,51} With the help of metallic nanostructures of films, spontaneous emission rates and the directionality of the emission can be modified, leading to metal-enhanced fluorescence in the labelfree detection.⁵² Krishanu Ray et al showed that Al films as substrates could significantly enhance the UV emission intensity of DNA base analogue 2-AP. Maximum of about 9-fold increase in the emission intensity was obtained.⁵³ Strong coupling between Al nanoantennas and J-aggregating molecules helped to investigate the bright hybrid exciton-LSP states, and lager Rabi energy splitting of 0.4 eV was observed.⁵⁴ Davy Gérard et al studied the strongly enhanced fluorescence from the emitters near the Al nanoaperture of various diameters. However, gold apertures exhibited significantly higher fluorescence enhancement factors than Al apertures in the visible range.⁵⁵

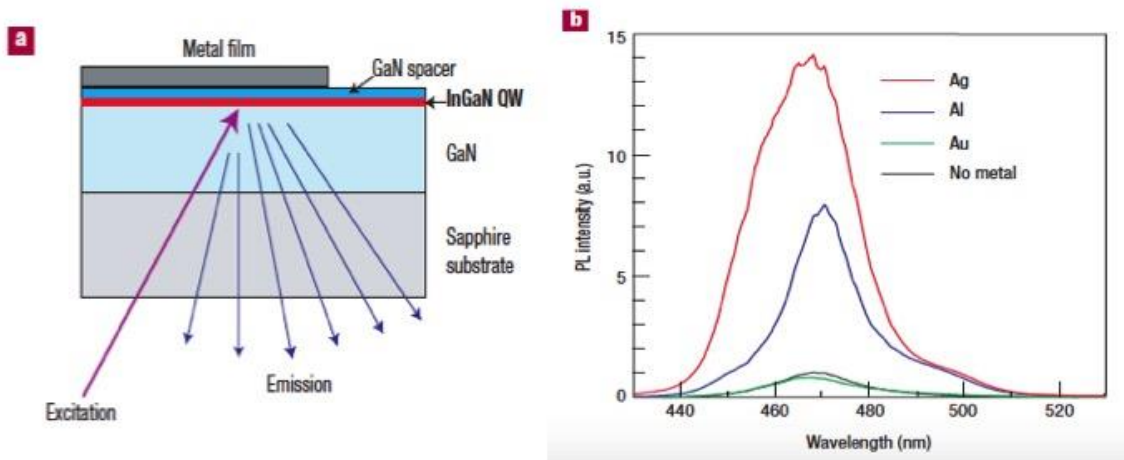


Figure 1.8. Surface-plasmon-enhanced light emitters. (a) Sample structure and excitation/emission configuration of photoluminescence measurement. (b) Normalized photoluminescence spectra of InGaN/GaN quantum wells coated with Ag, Al and Au. The distance between the metal layers and quantum wells was 10 nm.⁴⁷

1.5.3. Color printing

The use of metallic nanoparticles for the structural coloration can trace back to the antiquity like the famous Lycurgus Cup.⁷ Aluminium supports a strong scattering in a large spectral window spanning the whole visible range. Shawn J. Tan et al firstly used Al plasmonic pixels to reproduce one of Monet's paintings, as shown in Figure 1.9.⁵⁶ Since then, color printing using Al plasmonics has been a hot topic in recent years. Based on the array of asymmetric cross-shaped Al nanoapertures, Zhibo Li et al demonstrated that this nanopixels had polarization-switchable color properties. The dualcolor selectivity enabled a single nanoaperture to encode two information states within the same physical nanoaperture.⁵⁷

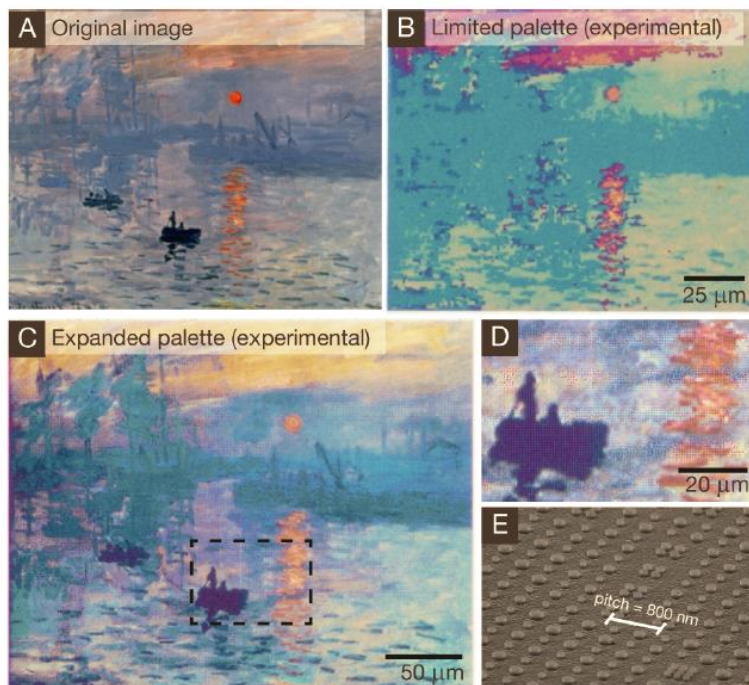


Figure 1.9. Reproduction of Monet's Sunrise using Al plasmonic color print. (A) Original image. (B) Experimental reproduction using only the limited plasmonic pixels. (C) Realistic reproduction using an expanded plasmonic pixel. (D) Higher magnification image of dotted box in (C). (E) Tilted SEM image of pixels.⁵⁶

Various advantages of nanoparticle color printing include subdiffraction-limited resolutions and the convenient generation of full colors without color pigments.⁵⁶ However, challenges still remain to pursue the higher quality of Al plasmonic structural color. Firstly, the broad plasmonic resonance of Al NP in the visible range with low Q factor will reduce the spectral

purity, and also decrease the color saturation or brightness. Because the red pixel supported by the bigger Al NPs, which usually exhibit a very wide spectrum (resulting a near white vision), it is even more crucial to suppress the wide spectra at the red part.⁵⁸ Secondly, the incident angle dependence needs to be reduced for larger viewing angle. Thirdly, polarization-independent spectra from plasmonic pixels will be beneficial for the wide applicability.⁵⁹ Therefore, increasing new strategies to enhance Al nanostructures for color printing have been proposed to achieve high color saturation and wide gamut. By coating a protective PMMA layer on the nanohole structures, it was found that the polymer layer helped to satisfy the impedance matching to free space and thus yielded high color saturation.⁶⁰ To obtain the narrow spectra for the RGB pixels, periodic arrays of Al nanorods were designed to exploit far-field diffractive coupling and suppress the scattering response at the short wavelength.⁶¹ Color mixing technique of cyan magenta yellow key (CMYK) printing was also adapted to Al nanorod structures. The printed image was found very sensitive to polarization, but maintaining the viewing angle insensitivity.⁶²

1.5.4. Other applications

The applications of Al plasmonics certainly are not limited to the above-mentioned areas. In this section, several examples will be listed to show the widespread applications and promising prospects of Al plasmonics. By using the self-assembly of Al nanoparticles into a three-dimensional porous membrane, a plasmon-enhanced solar desalination device was designed and fabricated, as shown in [Figure 1.10a](#). The porous plasmonic absorber could efficiently absorb a broad solar spectrum and enable the efficient and effective desalination of seawater.⁶³ Linan Zhou et al used chemically synthesized Al nanocrystals as a photocatalyst for hydrogen dissociation ([Figure 1.10b](#)). The hot electrons transfer from Al NPs to the antibonding orbitals of hydrogen molecules, which weakens the H–H bond, and thus induces molecule dissociation.²² The enhanced scattering of metallic NP will improve light trapping and energy conversion efficiency of solar cells.⁶⁴ A reliable light-harvesting platform based on Al nanostructures was stably utilized in a corrosive aqueous environment ([Figure 1.10c](#)), which resulted in a 300 % efficiency increase in the solar-to-chemical energy conversion.⁶⁵ Meanwhile, Al plasmonics have also been demonstrated efficient for numerous potential applications including non-linear optics⁶⁶, optoelectronics⁶⁷ (plasmonic assisted lasing, by

Chapter 1

coupling Al with wide band gap semiconductors such as GaN), photocatalysis^{68,69} and data storage⁷⁰.



Figure 1.10. (a) Experimental setup for solar desalination.⁶³ (b) Scheme of hydrogen dissociation using Al nanocrystals.²² (c) Scheme of Al nanoarrays for plasmonic-enhanced light harvesting.⁶⁵

Chapter 2 Long-term stability of aluminium nanoparticles

The oxidation process is one inevitable issue, which must be taken into account in Al plasmonics. Upon exposure to the atmosphere, the natural oxidation process generates an amorphous oxide layer of about 3-5 nm immediately at the surface of the Al NPs. This dense layer is believed to dramatically slow down the subsequent oxidation by preventing oxygen diffusion, acting as a passivation layer.⁷¹ Due to the large surface to volume ratio of nanoparticles, the natural stability of Al NPs might be different with previously studied Al films, and has not been studied thoroughly. Additionally, the previous studies about Al NP oxidation were mostly performed for combustion-based issues and did not involve the optical properties. In this chapter, an investigation of the plasmonic performance of Al nanodisk arrays over a long period of time was achieved. This is not only important for the proper use of Al NP for scientific researches but also very important for further commercial productions of Al plasmonics-based applications.

2.1. Model to simulate the oxidation

To give a better understanding on the evolution of the plasmonic properties with the increase of the oxide layer (alumina, Al_2O_3), finite-difference time-domain (FDTD) simulations were used to calculate the extinction spectra of Al nanodisk arrays. In order to obtain the extinction spectrum for each configuration, a simplified model is adopted, as described in [Figure 2.1](#). The first approximation is to consider that the global geometrical shape is kept constant during the oxidation, *i.e.* Al_2O_3 has the same volume with Al. Then, we continuously increase the uniform Al_2O_3 layer (thickness L) from zero until the disappearance of metallic core. In detail, the increasing thickness of Al_2O_3 shell is achieved by gradual decreasing both the radius and height of the Al core and by replacing the corresponding volume by Al_2O_3 .

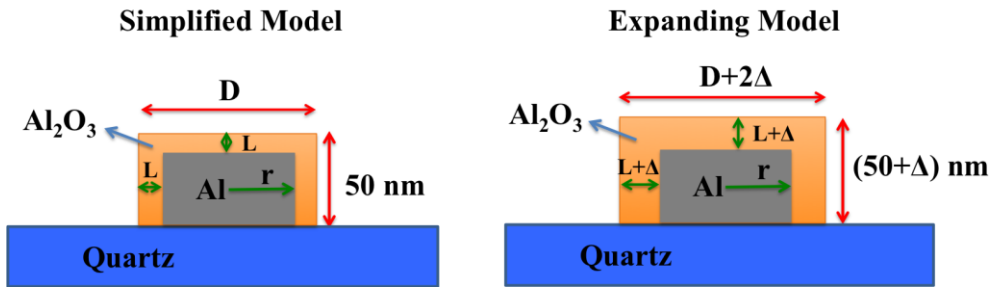


Figure 2.1. Schematic representation of the simplified model and expanding model used to simulate the oxidation of Al nanodisk with a diameter D , a metallic core radius r , an oxide layer thickness L , and additional thickness Δ of oxide layer due to the expanding volume between Al_2O_3 and Al in the expanding model.

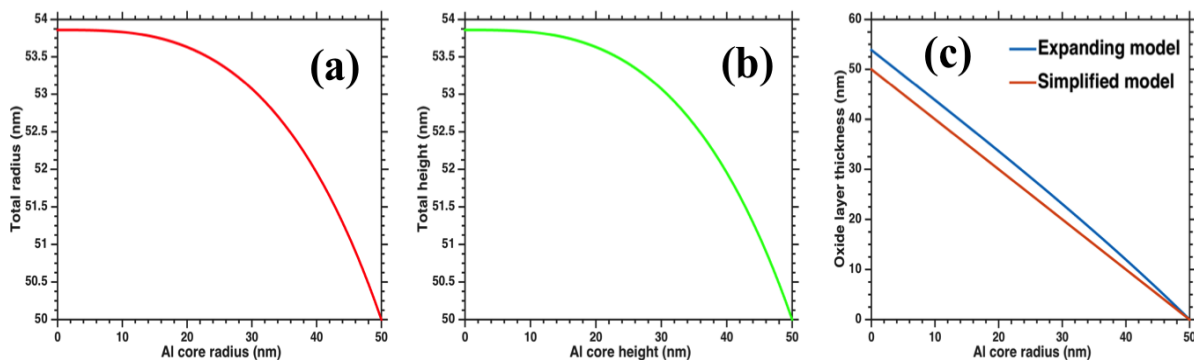


Figure 2.2. Calculations obtained for an Al nanodisk (radius 50 nm and height 50 nm) with the expanding effect between Al and Al_2O_3 . Total radius (a) and height (b) respectively plotted as a function of the Al core radius and height. (c) Comparison of oxide layer thickness between the simplified model (no volume extension) and the expanding model (taking the volume extension into account).

Nevertheless, for a certain volume of Al, an extension of the volume during the oxidation occurs ($V_{\text{Al}} : V_{\text{Al}_2\text{O}_3} \approx 80\%$, simply calculated using the densities of Al (2.7 g/cm^3) and Al_2O_3 (4 g/cm^3)). If we consider this expanding effect, additional thickness Δ of oxide layer is introduced, as depicted in the expanding model of Figure 2.1. Presuming that a uniform oxide layer is formed during an isotropic linear expansion process without shape deforming (the height and radius have the same increment of oxide), the change of NP's height and radius as the function of metallic height or radius can be calculated. The calculated results of an Al nanodisk (radius 50 nm and height 50 nm) are depicted in Figure 2.2. Comparing with the

simplified model under the condition of unchanged geometry (no volume expansion), additional thicker Al_2O_3 layer Δ is introduced in the expanding model, which will further induce a redshift of LSPR in the extinction spectrum.⁷² At the initial stage of oxidation (metallic core radius decreased by 10 nm), the difference of oxide layer thickness between two models is about 1.5 nm. Even if considering the full oxidation (the metallic core is completely oxidized), the difference between two models is only about 4 nm. Similar results are observed for varying sizes of nanodisks (not shown here). For smaller disk (diameter 50 nm, height 50 nm), the maximum difference is less than 2.5 nm. For bigger disk (diameter 160 nm, height 50 nm), the maximum difference is around 5 nm. In all, the deviations between two models are relatively small and can be tolerated. However, to take into account the expanded volume due to oxidation, a much thinner mesh will be demanded in the FDTD simulation, thus improving the requirement of calculating memory and time. Meanwhile, the simulated extinction spectra obtained from the simplified model are in good agreement with experimental results, as will be shown below. Thus, the simplified model is used in the following to perform the FDTD calculations.

2.2. Calculated extinction spectra

The extinction spectra of Al nanodisk arrays (diameter $D = 50, 70, 100, 130$, and 160 nm, height 50 nm, pitch 2.5D, named after D50, D70, D100, D130, and D160 respectively) were calculated with an increasing thickness of oxide layer. The extinction spectra obtained from the simulations are displayed in [Figure 2.3a](#). First, it appears that smaller nanodisks lose their optical properties at relatively thinner oxide layer (half of the maximum resonance intensity is lost at 10 nm oxide thickness for D50). Comparatively, the plasmonic resonances of bigger nanodisks still hold with high intensity even if the oxide layer is over 30 nm thick. Notice that higher modes appear at the shorter wavelength in the extinction spectra. Here, we are only interested in the dipolar mode at longer wavelength. Therefore, the peak shift and intensity of the dipolar resonance, which are normalized with the spectra corresponding to the nanodisk with no oxidation ($L = 0$ nm), are extracted and plotted in [Figure 2.3 \(b\)](#) and [\(c\)](#). At first, the resonances of the smaller nanodisk arrays (D50, D70, and D100) initiate with a redshift for a thin oxide layer (up to about 10 nm). For thicker oxide layer, a blueshift happens until the disappearance of LSPR (meaning that the Al core is almost completely transformed to oxide). Furthermore, the maximum redshift decreases with increasing size of nanodisk. The smaller

Chapter 2

nanodisk (D50) presents a maximum redshift of 20 nm, while the bigger nanodisk (D100) presents one of only 5 nm. For nanodisks with higher diameters (D130 and D160), the behaviour is different. Indeed, the peak wavelength keeps almost constant until an oxide layer thicker than 30 nm, then followed by a tremendous blueshift until the fading of the LSPR.

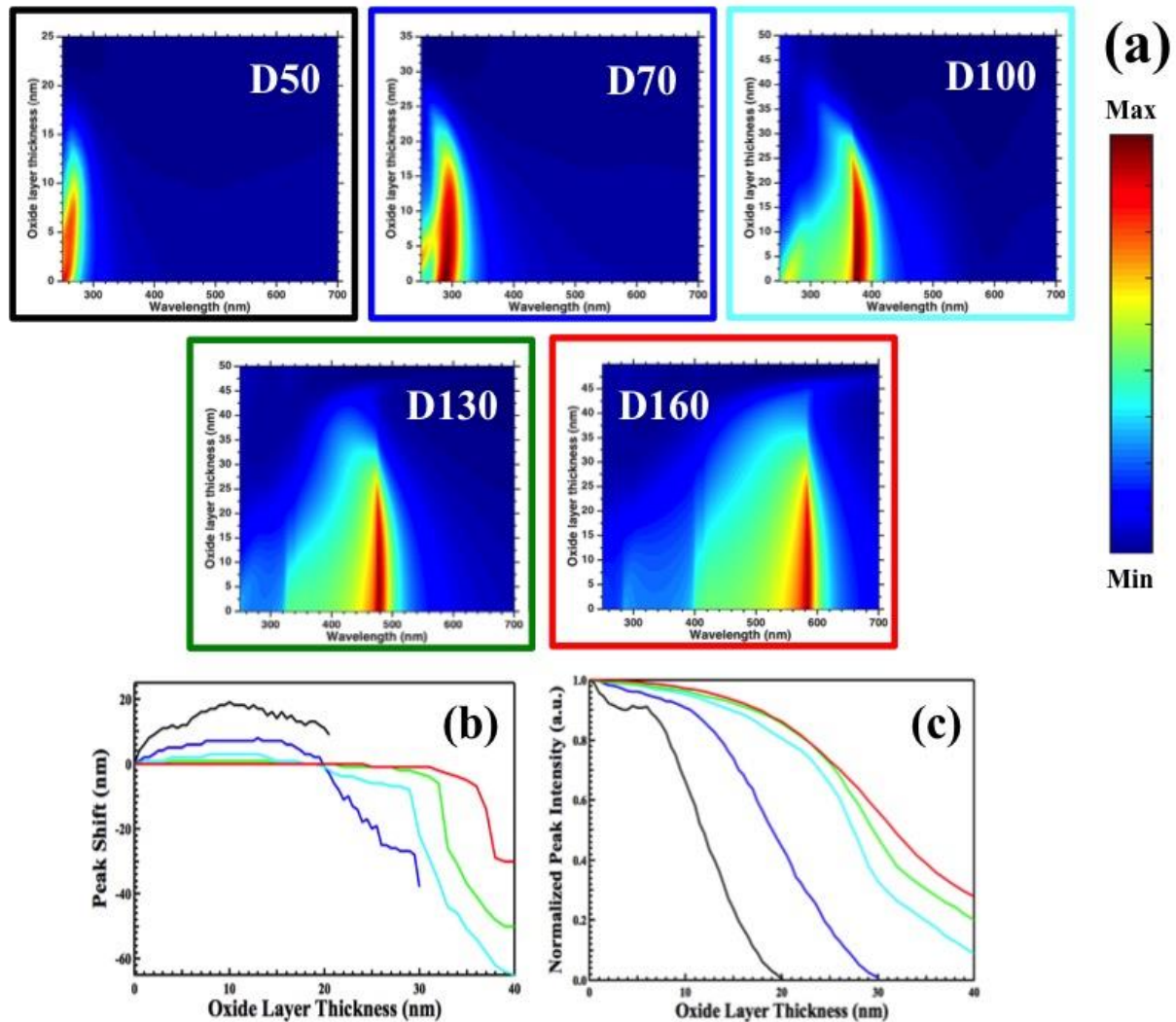


Figure 2.3. (a) Calculated extinction spectra of Al nanodisk arrays (diameter $D = 50, 70, 100, 130, 160$ nm, height 50 nm, pitch 2.5D) with increasing oxide layer. The scale bar stands for the extinction intensity. (b) Peak shift and (c) peak intensity of the dipolar mode normalized with the spectrum of each nanodisk without oxide layer are plotted as a function of oxide layer thickness. The color of each box in (a) corresponds the line color indicating the size of nanodisk in (b) and (c).

In the FDTD simulations, Al oxidation process is actually simulated by two main mechanisms: shrinkage of metallic Al core and increasing thickness of Al_2O_3 shell. The decreasing size of Al core will certainly induce a blueshift, while the increase of the Al_2O_3 layer will produce a redshift.⁷³ For the smaller nanodisks (D50, D70 and D100), the augmentation of oxide layer within about 15 nm dominates the process with a redshifted resonance, and then the shrinkage of Al core dictates the total effect leading to a blueshifted resonance until the surrounding Al_2O_3 layer eliminates the plasmonic properties completely. In the case of the bigger nanodisks (D130 and D160), these two mechanisms reach into a balance until the metallic volume is greatly reduced ($L \approx 30$ nm). This counterbalanced effect between blueshift and redshift, which at certain conditions results in no shift with increasing oxidation, actually has been previously reported by another group.¹⁷ As already pointed out in the previous section, additional redshift will be generated with considering the expanding effect of Al_2O_3 .

By analysing the normalized peak intensity with increasing Al_2O_3 layer as shown in [Figure 2.3c](#), it appears that the peak intensity decreases continuously as increasing the thickness of Al_2O_3 layer regardless of diameters. However, the smaller nanodisks present much faster decreasing rates of the peak intensity than the bigger nanodisks as a function of oxide layer thickness. This is obviously due to the ratio between the metallic core and the increasing oxide layer, which decreases much faster for smaller NPs during oxidation. The peak intensity is normally not considered in the previous studies, however it should be a relevant parameter to determine the degree of oxidation since the bigger nanodisks show no shift in their LSPR wavelength even for a strong oxidation. For instance, we could imagine a calibration process giving the oxidation degree based on the resonance intensity decrease. Meanwhile, we are going to using this criterion in order to exclude other effects like self-annealing, which will be encountered in experiment. As a conclusion of our simulations for the oxidation process of Al nanodisk arrays, Al NPs with higher dimensions or volumes are expected to have longer stability than smaller nanodisks. Moreover, we clearly demonstrate that FDTD simulation is an interesting tool to obtain the basic interpretation of plasmonic-resonance evolution during the Al oxidation procedure.

2.3. Long-time experimental measurement

Chapter 2

The nanodisk arrays (diameter D = 70, 100, 130, and 160 nm, height 50 nm, pitch 2.5D) were fabricated using electron beam lithography process. The SEM images obtained at the second day after fabrication are exhibited in [Figure 2.4](#). The corresponding dark field images shown in [Figure 2.4 \(insets\)](#) are in good accordance with the extinction spectra ([Figure 2.5a](#)). Al NP array of D70 is barely visible due to the extinction resonance peak and diffusion located in the UV region. Meanwhile, the Al NP arrays of D100, D130 and D160 exhibit a blue, cyan, and white-yellow diffusion respectively due to their optical properties located in the visible region. For biggest diameter (D160), the broad resonance centred at 605 nm gives rise to a whitish diffusion in the dark-field microscopy.

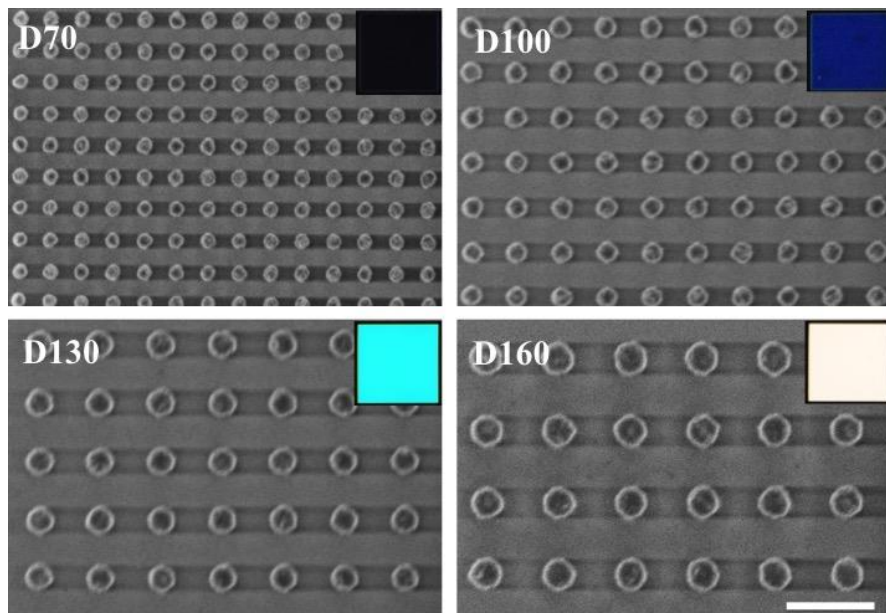


Figure 2.4 SEM images of nanodisk arrays at the second day after their fabrication. Scale bar 500 nm. Inset shows corresponding dark-field image of the array.

After fabrication, the samples were totally exposed to the ambient air in cleanroom ($T=21\text{ }^{\circ}\text{C}$, relative humidity around 40 %) and extinction spectra were measured continuously in a long-term period (250 days). [Figure 2.5](#) depicts experimental extinction spectra plotted as a function of time. A slight enhancement in the extinction intensity is observed in [Figure 2.5c](#), which could be ascribed to the self-annealing effect of Al nanodisks. Meanwhile, self-annealing effect also has a contribution to the blueshifted resonances in [Figure 2.5b](#). Self-annealing effect is a common phenomenon widely observed for various materials with different fabrication methods during their long-term storages at room temperature.^{74,75,76,77} The driving force of this natural recrystallization is believed to be related with the internal

strains and defects down to atomic dislocations. Factors like deposition conditions and impurities play an important role in the natural grain growth rate. Metallic nanostructures made by EBL process generally contain more defects (such as grain boundaries) than those obtained by chemical methods.^{78,79} Meanwhile, the thermal evaporation could induce a high strain inside the Al NP, which results in a higher enthalpy state.^{80,81} Therefore, due to thermodynamic effect, NP could release energy by increasing grain sizes naturally, leading to a slow spontaneous annealing at room temperature over a long period of time.

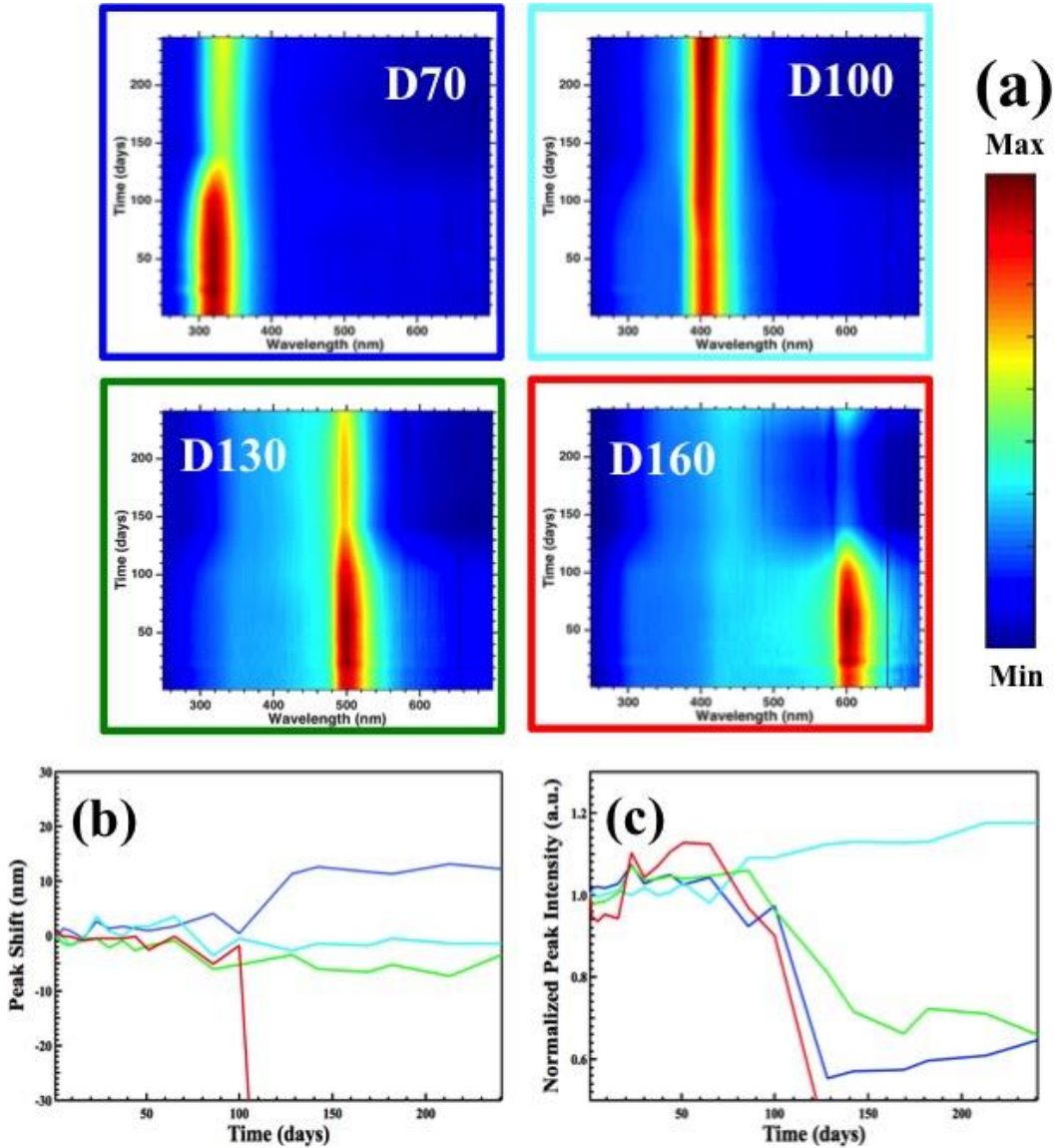


Figure 2.5. (a) Experimental extinction spectra of Al nanodisk arrays (diameter D= 70, 100, 130, and 160 nm, height 50 nm, pitch 2.5D) as a function of time. The scale bar stands for the extinction intensity. **(b)** Peak shift and **(c)** peak intensity of the resonance normalized with the spectrum measured on the first day. The color of each box in (a)

Chapter 2

corresponds the line color in (b) and (c) indicating the size of NP. Fluctuation arises from slight differences in the alignment during individual measurement.

Generally, [Figure 2.5](#) shows a competition between the self-annealing and oxidation effects. After a relative stability of 90 days, the small nanodisk (D70) clearly shows redshifted spectrum and a decreased intensity due to the oxidation. Indeed, the larger surface to volume ratios of smaller nanodisks could increase the oxidation rate. For bigger nanodisk (D130 and D160), the predicted resonance maximum wavelength is nearly constant during the initial oxidation as shown by simulation in [Figure 2.3b](#). This behavior doesn't change in experiment for 90 days as shown in [Figure 2.5b](#). However, D130 and D160 show increased oxidation after about 90 days, confirmed by blueshifted peaks and continuously decreased extinction intensities. The diffusion of atoms during the oxidation process is likely to occur along the grain boundaries and defects inside the NPs. Therefore, more defects inside bigger nanodisks will facilitate the oxidation. The balance happens for D100 by keeping a relatively stable resonance wavelength and a weak enhancement on intensity due to self-annealing. These results prove that oxidation has minor effect on D100 during the observing period. In contrast with the prediction of FDTD simulations in [Figure 2.3](#), smaller nanodisks and bigger nanodisks show relatively shorter stability in experiment.

The optical stability of Al NP is an important consideration for their potentially commercial utility. In our experiments, nanodisk arrays made by EBL show relatively good stability within 90 days after the total exposure to ambient air. The samples made by different methods might show different performances due to changes inside the nanostructure like grain sizes. Actually, the natural subsurface oxidation of Al NP during the period of storage is driven by a complicate process, involving the environment (like humidity and temperature), interface diffusion of Al cations and O anions, possible morphology change due to the different mechanical properties of metallic core and oxide shell, and phase transformation.^{23,43,82,83} Although the oxide layer of Al is believed to be very efficient at stabilizing the optical property, a complex result including self-annealing phenomenon was obtained for Al NP arrays in experiment as shown in [Figure 2.5](#). The experimental results remind the crucial importance when involving the long-time stability of nanostructures used in Al plasmonics. If

longer stability is further required, new strategies like encapsulation should be developed to prolong and stabilize the plasmonic properties of Al NPs.^{20,21,84}

2.4. Corrosion in water

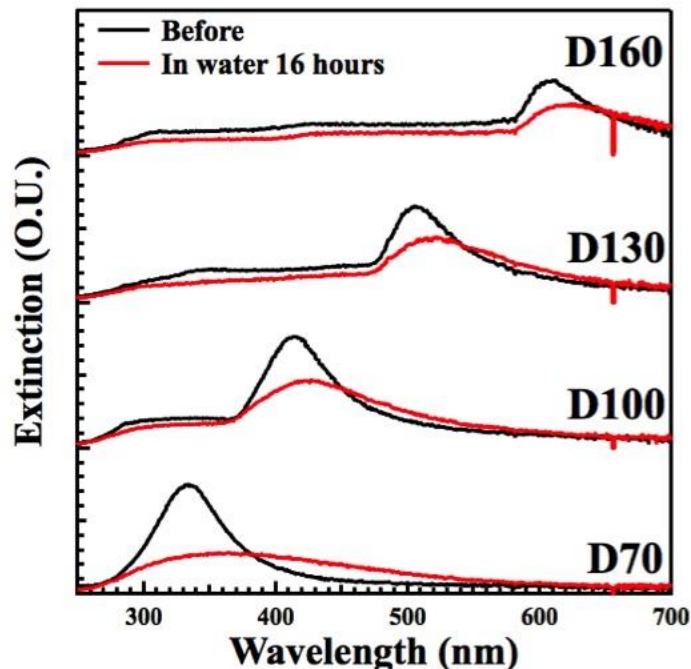


Figure 2.6. Experimental extinction spectra of Al nanodisk arrays (diameter D= 70, 100, 130, and 160 nm, height 50 nm, pitch 2.5D) before (black line) and after (red line) being stored in water for 16 hours.

Al nanodisk arrays were also fabricated and stored in distilled water (40 ml in a beaker) to test their resistance to water corrosion. Measured extinction spectra are plotted in Figure 2.6. It is clear that the after the 16-hour immersion in water, extinction spectra were strongly modified. Obvious diminution on the extinction peak intensities and redshifted peak wavelengths are observed. Due to the reaction between water and Al, immersing in water could accelerate the oxidation process with various oxidation products. Hence, a drastic change in the oxide shell will occur with possible morphology alteration and plasmonic resonances no longer follow the prediction of previous FDTD simulation. After 5 days, there are no plasmonic resonances at all, indicating the total elimination of metal inside the NP.

Measured SEM images after 5 days storage in water (Figure 2.7) prove the strong corrosive effect of water to Al NP. It is clear that NPs became highly inhomogeneous with a rough surface if compared with pristine NPs in Figure 2.4. The SEM characterizations confirm the strong corrosion of Al NPs revealed by the optical measurements shown above. Markus Schwind et al did a full investigation of corrosion kinetics on Al nanodisk arrays in a well-controlled chamber filled with degassed water, and an initial slow growth of homogeneous oxide within 2 days was observed followed by a rapid oxidation.⁸⁵ Our results well correspond with their experiment. Obviously, the lifetime of Al NP in air is much longer than it in water, and the results remind us the vital role of environment to store or use Al NPs. For example, in the SERS measurement with the common drop casting or immersion method, the appearance of water should be avoided to protect the Al NPs. Moreover, LSPR chemical sensing, based on the functionalization of NP with key molecules in water based solutions will be not trivial with Al due to the corrosion effect.

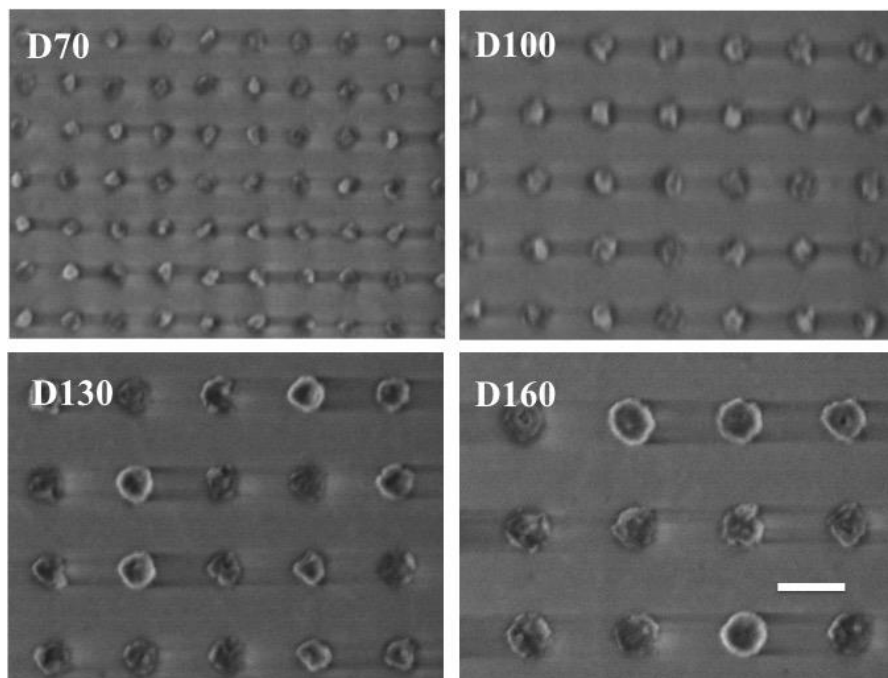


Figure 2.7 Nanodisk arrays (diameter D= 70, 100, 130, and 160 nm, height 50 nm, pitch 2.5D) after 5 days in the distilled water. Scale bar 250 nm.

2.5. Conclusions

The optical properties of aluminium nanoparticles over time is crucial for further applications like structural color and biosensing, and it should be even the first consideration for large-scale commercial production in the future. In this chapter, the long-term stability of aluminium nanodisk arrays with varying sizes (diameter from 50 to 160 nm, height 50 nm) is investigated. Plasmonic resonances during the oxidation vary with geometrical parameters of nanodisk and bigger nanodisks are predicted to have stronger stability by the FDTD simulation. In a long-term experiment where Al nanodisk arrays were exposed to ambient air, a 90-day period of stability was observed whatever the diameter of the nanodisks. The shorter optical activity of larger nanodisks is probably due to more defects lying inside them. The nanodisk array with 100 nm diameter was found to be more stable than others because of counterbalanced effects. When immersing samples into the water, the strong corrosion shortens the lifetimes of Al plasmonic within 5 days. The results remind us the crucial role of the stability of Al nanoparticle and the suitable usage of Al nanoparticle. In the future, appropriate treatments should be studied to prolong the lifetime of Al NPs and stabilize the plasmonic resonance for a commercially large-scale product.

Chapter 3 Rapid thermal annealing for the improvement of Al nanoparticles plasmonic properties

Even if a self-limited oxide layer protects Al nanostructures, their stability when exposed to various industrial processes is a critical point for their systematic use in commercial systems. For instance, it is relevant to study the effect of temperature elevation on the optical properties of Al nanoparticles, as they can experience strong local heating in future devices or during fabrication processes used in industry. For these reasons, it is of importance to study the effect of thermal annealing on Al nanostructures. In this part, nanodisk arrays with diameter 80, 100, and 120 nm and height 40 nm were fabricated by electron beam lithography method. The pitch between the circular apertures is set to 250 nm. Rapid Thermal Annealing (RTA) in the ambient air was done at 300, 400, 500 and 600 °C successively. We investigate the optical response of Al nanodisks when annealed in a RTA furnace at different temperatures.

3.1. Blueshifted plasmonic resonance after low temperature RTA

The general principle of the experiment is depicted in [Figure 3.1](#), showing two typical extinction spectra measured on arrays of Al nanoparticles before ([Figure 3.1a](#)) and after ([Figure 3.1b](#)) annealing at 400 °C. A peak centred around 420 nm corresponding to the plasmonic dipolar resonances sustained by the Al nanoparticles is evidenced on the pristine sample. After annealing, the peak wavelength is shifted to a value slightly below 400 nm, while its FWHM is reduced by a factor ~ 1.5 . As evidenced in the following, we attribute this effect to a reduction of grain boundaries inside the metal during the annealing. Other studies²³

have shown that at this temperature no additional or very little oxidation occurs inside the metal core of the nanoparticles. The native oxide layer remains amorphous under 400 °C, with a constant thickness.

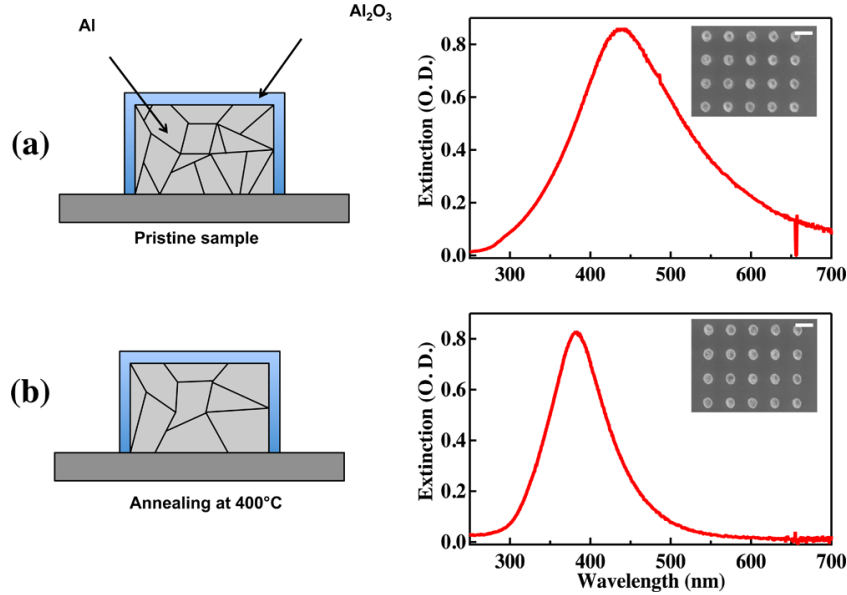


Figure 3.1. Principle of the experiment: extinction spectra on arrays of Al nanoparticles (diameter 100 nm) before (a) and after (b) RTA annealing at 400 °C. Insets: corresponding SEM images. Scale bars 200 nm.

It is worth noticing that the SEM images (Figure 3.1, insets) evidence that the RTA process at 400 °C does not affect the shape of the nanoparticles, whose cross-section remains circular. We can therefore argue that the effect of RTA on the plasmonic properties is not due to a deformation or reshaping of the nanoparticles. This stability is actually due to the high adhesion coefficient between Al and the substrate, hindering any efficient dewetting process even at high temperature. Besides reducing the damping factor, the effect of recrystallinity introduced by RTA has been reported to increase of the free electron density or decrease the effective electron mass in Drude's model, which increases the plasma frequency and thus causes a blueshifted extinction spectrum.⁷⁴ Notice that elimination of the incorporated gases and lattice defects was also deduced by other researchers.⁸⁶

3.2. Extinction spectra after RTA treatments

We now present a more detailed investigation of the plasmonic properties depending on the annealing temperature. Extinction measurements on the Al nanoparticles after successive

Chapter 3

RTA treatments with increasing temperature have been carried out. Results are summarized in [Figure 3.2](#). Extinction spectra measured on arrays of Al nanoparticles after each step of the RTA process with temperatures ranging from 300 to 800 °C are plotted in [Figure 3.2 a–c](#) for three different diameters. Whatever the diameter of the structure, a clear trend is discernible: the dipolar plasmonic resonances experience an increasing blue shift accompanied by a reduction of their FWHM for annealing temperatures of 300 and 400 °C. Above this temperature, the resonances behave differently. With RTA at 500 °C, resonances then experience a more or less pronounced red shift and a decrease in intensity; this effect is more pronounced for the smaller diameters. For temperatures equal to or above 600 °C, the intensity of the resonances further decreases while they experience a slight blue shift. This effect is particularly pronounced for small diameters where the dipolar resonances almost vanish, resulting in a weak and asymmetrical peak. For larger diameters (≥ 100 nm), the optical signature remains even for 700 and 800 °C RTA and keeps an almost constant intensity and shape.

As developed in the following, we attribute the evolution of the plasmonic properties under RTA treatments to two main mechanisms: (i) the diminution of the number of grain boundaries inside the metal and (ii) its oxidation. The former is dominant at lower temperatures (up to 400 °C) and induces a blue shift and an increase in the oscillator strength of the resonances reducing their width, as previously shown for gold and silver nanoparticles.^{87,88} The latter, dominant at higher temperatures (above 400 °C), increases the thickness of the alumina shell at the expense of the metallic core. The subsequent shrinkage of the metallic core induces a blue shift of the LSPR as well as a decrease in the scattering cross-section and thus of the peak intensity. Simultaneously, the increasing oxide shell thickness tends to red shift the spectral position of the LSPR due to the higher refractive index of the surroundings.^{18,73} Increasing the oxidation layer therefore leads to a more complex behavior where a red shift followed by a blue shift is experienced by the resonances, as shown further by calculations. Such a behavior has been numerically predicted in the case of aluminium hemispheres.⁸⁹

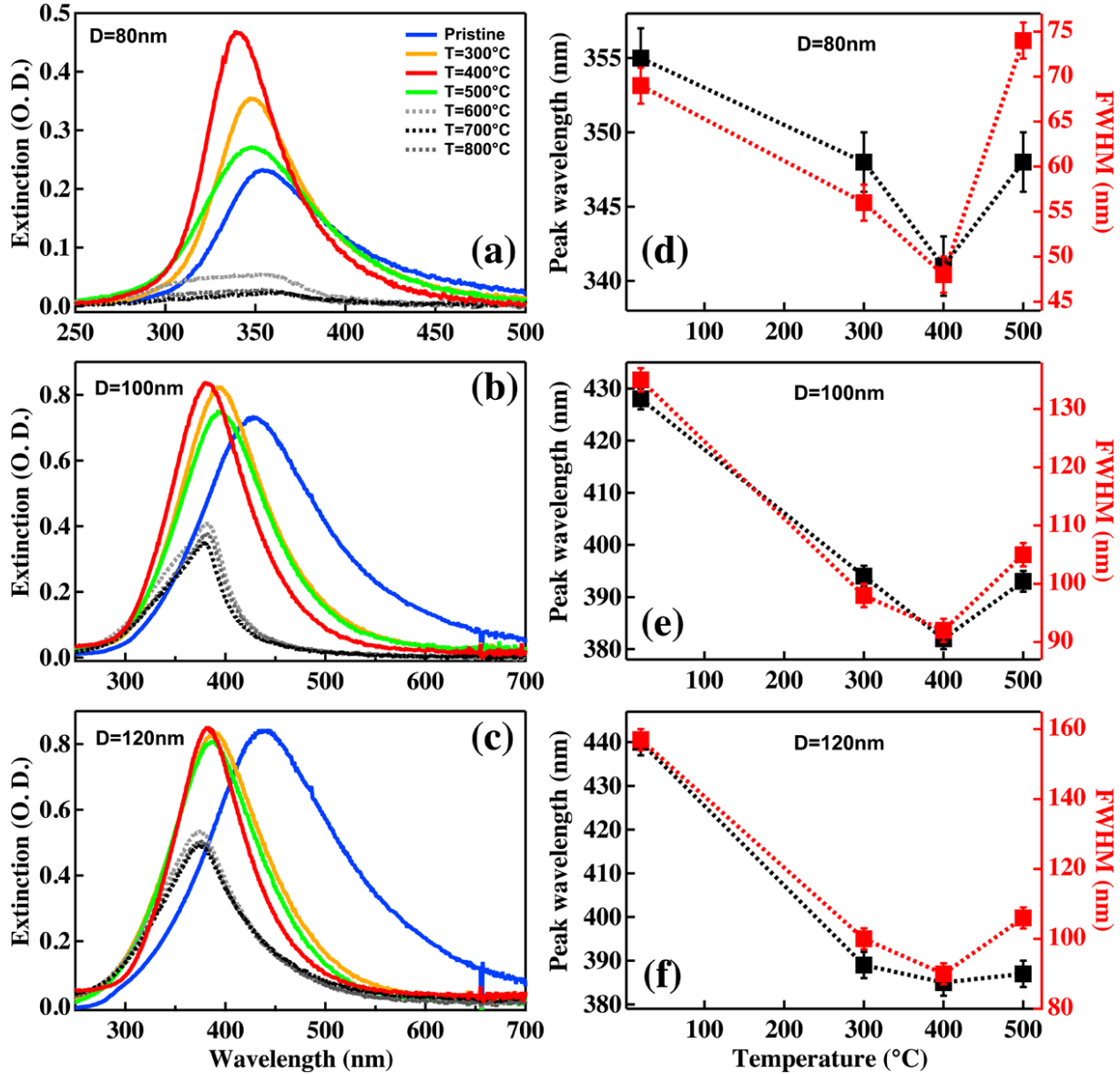


Figure 3.2. Column (left), for each box: extinction spectra of Al nanoparticles with fixed diameter after successive RTA treatments with increasing temperature. Column (right): evolution of the peak wavelength and line width with RTA treatment.

3.3. TEM measurement and Q-factor

Depending on the temperature range, two distinct regimes are observed, where one or the other of the two above mentioned mechanisms dominates. This is also illustrated in Figure 3.2 d–f, where the evolution of both the resonances' peak wavelength and FWHM has been plotted as a function of RTA temperature for each diameter. In the first temperature range (between 300 and 400 °C), oxidation is extremely weak and the number of grain boundaries

Chapter 3

decreases. Hence, the dipolar resonances experience a blueshift with a significant reduction of FWHM. At 400 °C, FWHM is reduced by a factor ~ 1.5 for every diameter and the blue shift is maximum. Above this threshold value (RTA at T = 500 °C), the resonances experience a red shift while their intensity decreases, indicating that oxidation becomes predominant. Simultaneously, a slight increase in the FWHM is evidenced. The FWHM and the peak wavelength value are not plotted for RTA at highest temperatures (from 600 to 800 °C) because the spectra present more complex behavior due to the simultaneous shrinkage of the metallic core and increase in the oxide layer as explained above. In addition, this behavior at the high temperatures will be further explained in next section.

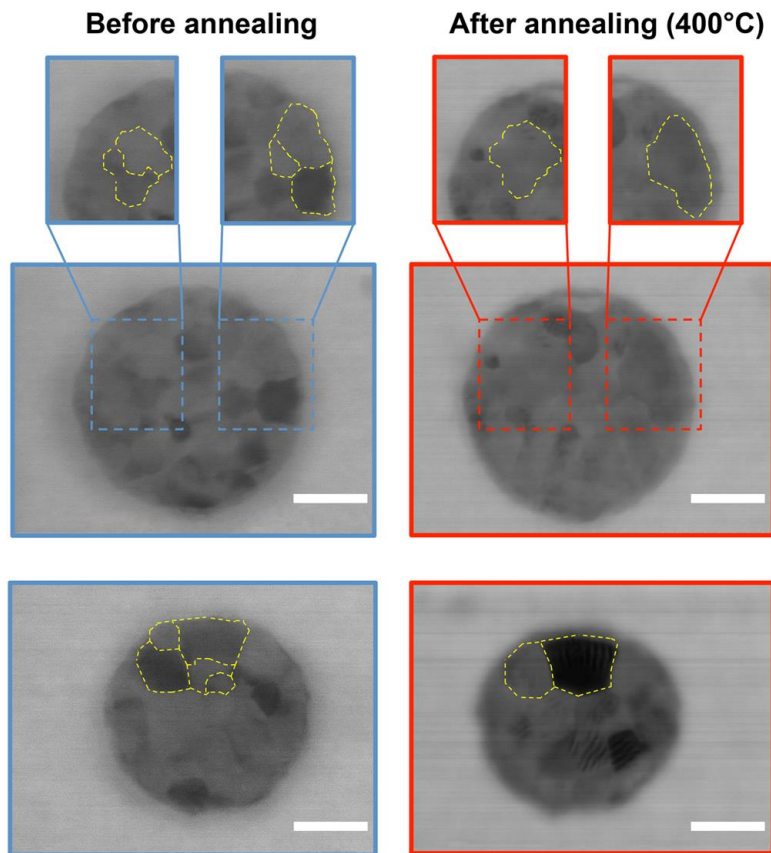


Figure 3.3. TEM images on the same single Al nanoparticles with diameter 150 nm (upper boxes) and 120 nm (lower boxes) pristine (blue boxes) and after RTA treatment at 400 °C (red boxes). Scale bars 50 nm.

The previous assumption concerning the evolution of grain boundaries under thermal annealing has been ascertained by characterizing the structural properties of Al nanoparticles by using TEM mode of the SEM-FEG microscope in our laboratory ([Figure 3.3](#)). Two pristine

Al nanoparticles (before annealing) and the same nanoparticles after 400 °C RTA treatment were characterized. The polycrystallinity of the pristine structures is evidenced in the TEM image by the grains, highlighted by the dashed yellow lines on Figure 3.3. The same nanoparticles after annealing exhibit fewer grain boundaries, likely due to grain-boundary migration at high temperatures, as already shown for gold nanoparticles.⁸⁷ However, in the aforementioned work the gold nanoparticles needed to be encapsulated prior to annealing. In our case, the native oxide layer self-encapsulates the aluminium nanoparticles, removing the need for this step. The diameter and morphology of the nanoparticles after 400 °C RTA remain the same as the pristine one, as expected. Consequently, the improvement of the dipolar plasmonic resonances quality factor Q, defined as

$$Q = \frac{\lambda_{LSPR}}{FWHM},$$

can be attributed to a decrease in the number of grain boundaries inside the Al core. This leads to a lower number of scattering centers for electrons, increasing their mean free path and subsequently the lifetime of the plasmonic resonances. Meanwhile, it also results in the lowering of the imaginary part of the metallic core's dielectric function. This was recently observed in epitaxially grown aluminium thin films compared with conventional thermally evaporated films.⁹⁰

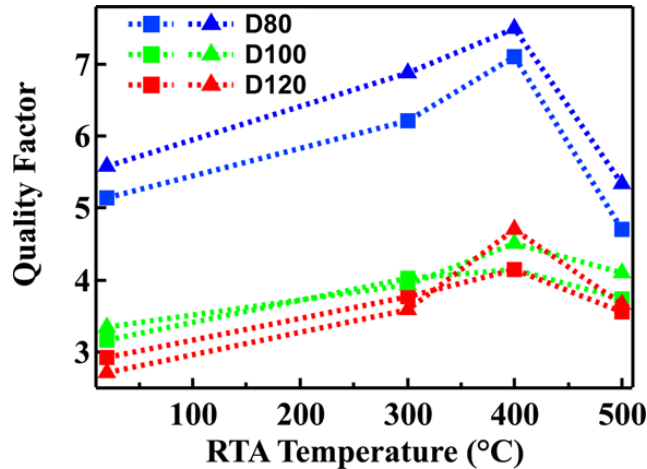


Figure 3.4. Quality factors of the dipolar resonances calculated from experimental spectra plotted as a function of the RTA temperature.

We summarize the improvement of the plasmonic dipolar resonances in Figure 3.4 by plotting the quality factor Q for several nanoparticles as a function of the RTA temperature. For every nanoparticle array, a clear improvement in Q at 400 °C is evidenced, with a relative increase by a factor of ~ 1.4 . The Q factor is even higher than the ones measured for the dipolar modes

of Al nanorods.⁹¹ For smaller nanoparticles, even if the relative improvement is the same, the absolute values of Q are globally higher. We attribute this to the intrinsic losses in Al, which are lower for shorter wavelengths (for instance, $\varepsilon_2 (\lambda = 450 \text{ nm}) \approx 2\varepsilon_2 (\lambda = 350 \text{ nm})$). Whatever the diameter of the nanoparticles, the Q factor decreases for RTA at temperatures above 500 °C due to the increased oxidation and deformation, as shown below.

3.4. Oxidation after high temperature RTA

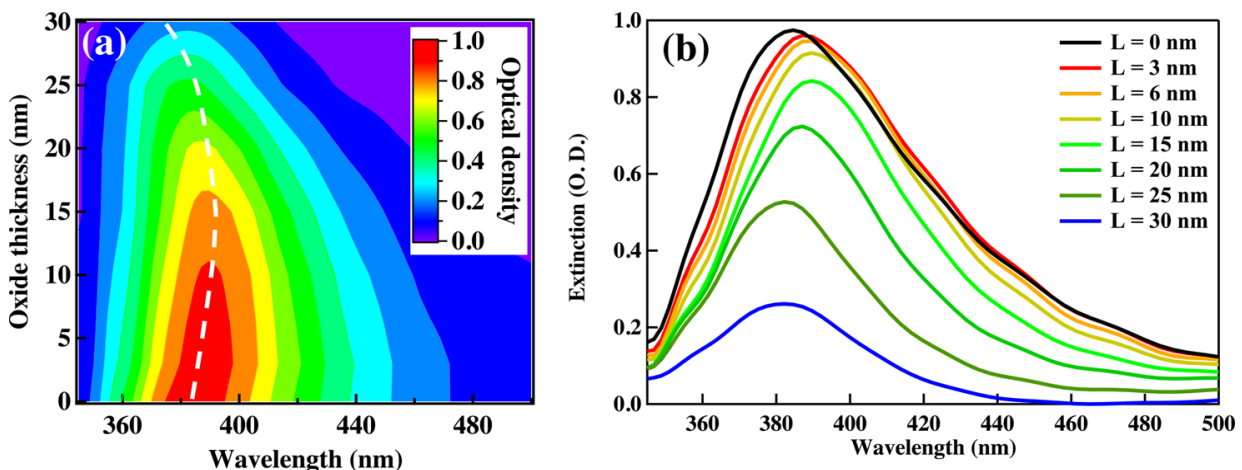


Figure 3.5. (a) Extinction spectra calculated with FDTD for a square array of Al nanoparticles with diameter $d = 100 \text{ nm}$ and thickness $h = 40 \text{ nm}$ for different ratios between the volume of Al core and the volume of oxide layer (from oxide thickness $L = 0 \text{ nm}$, no oxidation, to $L = 30 \text{ nm}$). **(b)** Corresponding extinction spectra for several oxide thicknesses.

The in-depth oxidation initiated during RTA at high temperatures induces both a reduction of the aluminium core and an increase in the surrounding alumina layer. To quantify this effect on the optical properties of aluminium nanoparticles, FDTD calculations have been performed, as illustrated in Figure 3.5. The calculations were done using *OptiFDTD software* (Optiwave Company). 3D modeling has been used with PML (Perfect Matched Layers) as boundary conditions on both the top and bottom sides of the simulation box, while PBC (Periodic Boundary Conditions) were used on the remaining four sides in order to take into account the array in the plane of the substrate. Refractive indices were taken from ref 92. Incident light is a plane wave, impinging from the substrate side. Different extinction spectra

were calculated for an array of Al nanoparticles (diameter 100 nm) with different thicknesses of oxide layer. In the simulations, we assume that the oxide thickness is gradually increasing while maintaining a constant overall diameter of the particles. As we already discussed in [Chapter 2](#), it is worth noticing that aluminium oxide exhibits a slightly larger volume than metallic Al. Therefore, the nanoparticle diameter actually increases under ongoing oxidation, while the number of Al atoms in the nanoparticles remains the same.⁹³ However, as demonstrated below, this assumption yields a good agreement with the experimental trends.

The lower spectrum in [Figure 3.5a](#) corresponds to pure Al nanoparticles (Al diameter 100 nm, oxide thickness 0 nm) and the upper one corresponds to strongly oxidized nanoparticles (Al diameter 40 nm, oxide thickness 30 nm). The dipolar resonance first experiences a red shift due to the oxidation (actually due to the high refractive index of alumina) until the metallic core reaches a diameter of 80 nm, corresponding to an oxide layer of 10 nm. At this point, the red shift value is ~ 8 nm. If the diameter further decreases, then the blue shift due to the reduction of the metal core size overcomes the red shift due to the refractive index of alumina, resulting in a net blue shift of the resonance position as well as a decreasing intensity. Finally, when the metal core reaches a diameter of 40 nm, a maximum blue shift of the dipolar resonance is obtained as well as a dramatically decreased intensity, which is lowered by a factor ~ 5 . For lower diameters of the metal core, the optical signature of the dipolar resonance further decreases and eventually vanishes away. As mentioned above, a similar behavior has been numerically observed for Al/Al₂O₃ hemispheres.⁸⁹ Halas's group has also experimentally studied the effect of oxidation on the plasmonic properties of Al nanoparticles.⁷² They showed a similar trend as observed here: red shift and decrease in resonances' amplitude. These calculations explain the behavior of experimental data in [Figure 3.2](#) for RTA from 400 to 800 °C. Once Al nanoparticles have reached their maximum structural improvement due to the reduction of grain boundaries, oxidation starts to dominate during RTA at higher temperatures and the oxide layer starts increasing. Consequently, dipolar resonances first experience a red shift and then a blue shift, while their intensity decreases. Eventually, oxidation is strong enough during the 5 min of RTA to almost transform the entire metallic core, resulting in very weak optical signature as experimentally shown for the smallest diameters.

3.5. Evolution of morphology

3.5.1. SEM measurement

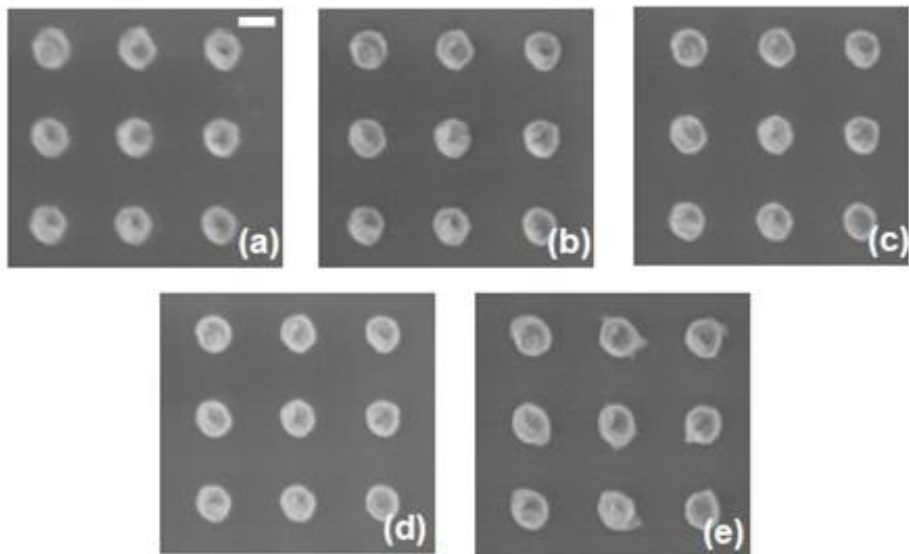


Figure 3.6. SEM images of the same Al nanoparticles (diameter 100 nm) pristine (a) and after RTA processes (300°C (b), 400°C (c), 500°C (d), 600°C (e)). Scale bar 100 nm.

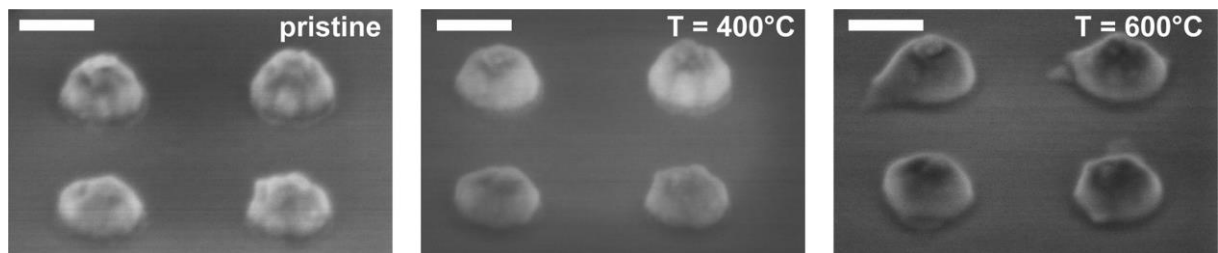


Figure 3.7. 45° tilted SEM images of Al nanoparticles arrays pristine and after RTA processes at $T = 400$ and 600°C . Scale bar 100 nm.

To explain the modification of the resonance shape at high temperature, both the surface roughness and the morphology of the structures were characterized with SEM as a function of the annealing temperature. Results are shown in [Figure 3.6](#). In the SEM pictures, no significant change is observed, except for RTA at 600°C . At this temperature and higher, the nanodisks are deformed, indicating major structural changes. To determine if any dewetting has occurred at the substrate-particle interface, SEM images were also done under a tilted angle (45°), as shown in [Figure 3.7](#). The similar tendency is observed.

3.5.2. AFM measurement

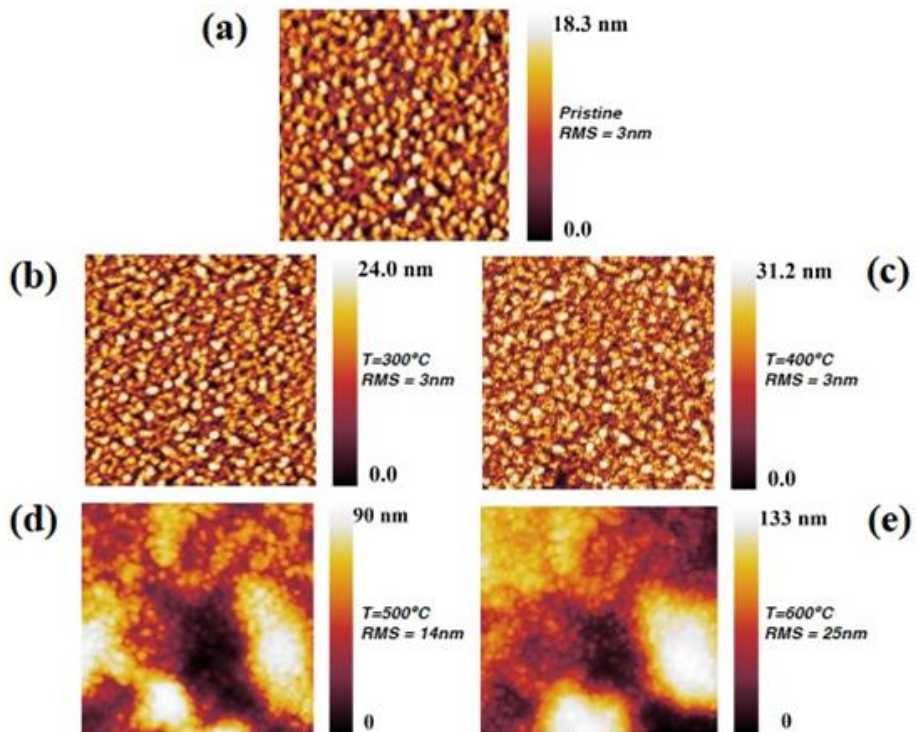


Figure 3.8. Evolution of Al thin film ($1 \times 1 \mu\text{m}^2$ area) with RTA.

Atomic force microscopy (AFM) measurements were also performed on thin films of Al deposited under the same conditions as the nanoparticles to retrieve the value of the surface roughness. While the thermal behavior of a continuous film may be different from the one of a nanoparticle, their average surface roughness should follow similar trends. The morphology over the same $1 \times 1 \mu\text{m}^2$ area is shown in Figure 3.8 and the value of the RMS roughness is extracted. The measured RMS roughness value is the same from the pristine sample up to the film annealing at 400°C ($\text{RMS} = 3 \text{ nm}$); then, it abruptly increases to $\text{RMS} = 14 \text{ nm}$ for 500°C and $\text{RMS} = 25 \text{ nm}$ for 600°C . The surface of the Al film is also significantly deformed with the emergence of grooves and bumps in the film. This effect is attributed to Al oxidation, as the volume occupied by aluminium oxide is larger than the volume occupied by aluminium for a constant number of Al atoms. Indeed, oxidation at the interface results in an increasing alumina layer inside the nanoparticle, resulting in distorted surface and shape, as shown by both SEM and AFM characterization at the highest temperatures.

3.6. Conclusions

In this chapter, a study on the evolution of plasmonic resonances sustained by aluminium nanoparticles under RTA in ambient air has been reported. The results evidenced the existence of two regimes during annealing. The first regime occurs with RTA temperatures ≤ 400 °C, where dipolar resonances sustained by the nanoparticles experience a blue shift due to a reduction of the number of grain boundaries inside the Al core. The second regime appears for RTA with temperatures > 400 °C. Here the higher level of oxidation results in the increase in the aluminium oxide layer thickness and a decrease in the aluminium core. As unveiled by FDTD calculations, this oxidation induces a more complex evolution of the dipolar resonances. The latter first experience a red shift and then a blue shift while their intensity decreases. The resonances eventually vanish away for small nanoparticles, as they may be fully oxidized. Finally, in the case of 5 min of RTA in air, an optimal annealing temperature of 400 °C is evidenced, at which the quality factor of plasmonic dipolar resonances in the blue to near-UV range is significantly improved. Above this temperature, the RTA process may become detrimental due to the increased role of oxidation. This effect has to be taken into account in any fabrication process involving heated Al plasmonic nanostructures.

Chapter 4 Surface roughness and substrate induced symmetry-breaking: influence on plasmonic properties of Al nanoparticle arrays

Regardless of the experimental methods, the geometric defects of NPs including shape deformation and disorder are always inevitable.^{94, 95} Besides, the surface roughness, detrimental to plasmonic properties, is also a common phenomenon involved. Furthermore, this issue is even severer for Al nanostructures prepared by the electron beam lithography (EBL) and classical deposition techniques such as thermal or electron beam deposition. Several models and methods have been applied to describe the influence of roughness on gold nanostructures.^{96,97} The substrate, leading to a high symmetry breaking, especially when there is a large contact between the nanostructure and itself, also has to be taken into account to fully understand the plasmonic properties, especially for Al ones where this effect has seldom been studied. In this chapter, a modeling method is proposed using Finite-Difference-Time-Domain (FDTD) method to investigate the influence of both the substrate and the surface roughness on the plasmonic performance of Al nanodisk. The RMS (Root Mean Square) roughness value of top surface is considered with a uniform oxide layer. Experimental results are then compared to FDTD calculations.

4.1. General difficulties to study the influence of roughness

In general, possible modifications on the parameters other than RMS surface roughness value should be excluded during the numerical studying to get reliable results. For example, the volume and total mass of nanostructures need to be constant.⁹⁸ In practical terms, the different fabrication processes may alter the surface roughness of the nanostructures, consequently

Chapter 4

inducing a variation in the dielectric function of the metal in the meantime.^{90,99} Similar issues also exist when using etching techniques to modify the surface roughness, which might also diminish the total mass of NPs in the meantime.⁹⁶ Meanwhile, possible diffusion of impurities inside the metal may also occur during the etching process. The oxide layer, formed once Al surface is exposed to the ambient air, has to be taken into account if we want to subtly tune the plasmonic properties of Al nanostructures. Consequently, a solid theoretical and experimental analysis of such parameter is very important to get a perfect control of optical properties that Al plasmonics offer.

4.2. Methods to model the surface roughness

In the software *Lumerical FDTD solution*, a seed number was first defined to generate a random matrix as the future surface fluctuation (RMS amplitudes). The same seed number will ensure us to recall the same matrix to generate the same rough surface every time. Then Fourier transform is applied in order to transform the matrix back to the real space with a Gaussian filter into a rough surface. Subsequently, the generated rough surface will be truncated into the desired core part (Al) and shell part (Al_2O_3). Thanks to the powerful ‘mesh order’ in *Lumerical* script language, the core and shell parts are now combined to generate our uniform core-shell model of Al nanodisk with a rough top surface. In detail, the Al core with ‘mesh order 2’ has the priority to replace the Al_2O_3 shell part with ‘mesh order 3’ when overlapping. Meanwhile, by shifting the two surfaces into different centre reference height (i.e. Al_2O_3 at 50 nm and Al at 46 nm) and making a 4 nm difference in the radius between Al_2O_3 shell (diameter 100 nm) and Al core (diameter 92 nm), a 4 nm uniform oxide layer will be eventually created. The schematic diagram to generate the designed nanodisk with top surface roughness is depicted in [Figure 4.1a](#). Although the results shown in this chapter are for nanodisks, the proposed method can also be applied to various geometries. In the following parts, without specific explanation the nanodisks used in calculations are all designed with 50 nm in the center height and with a 4 nm uniform oxide layer.

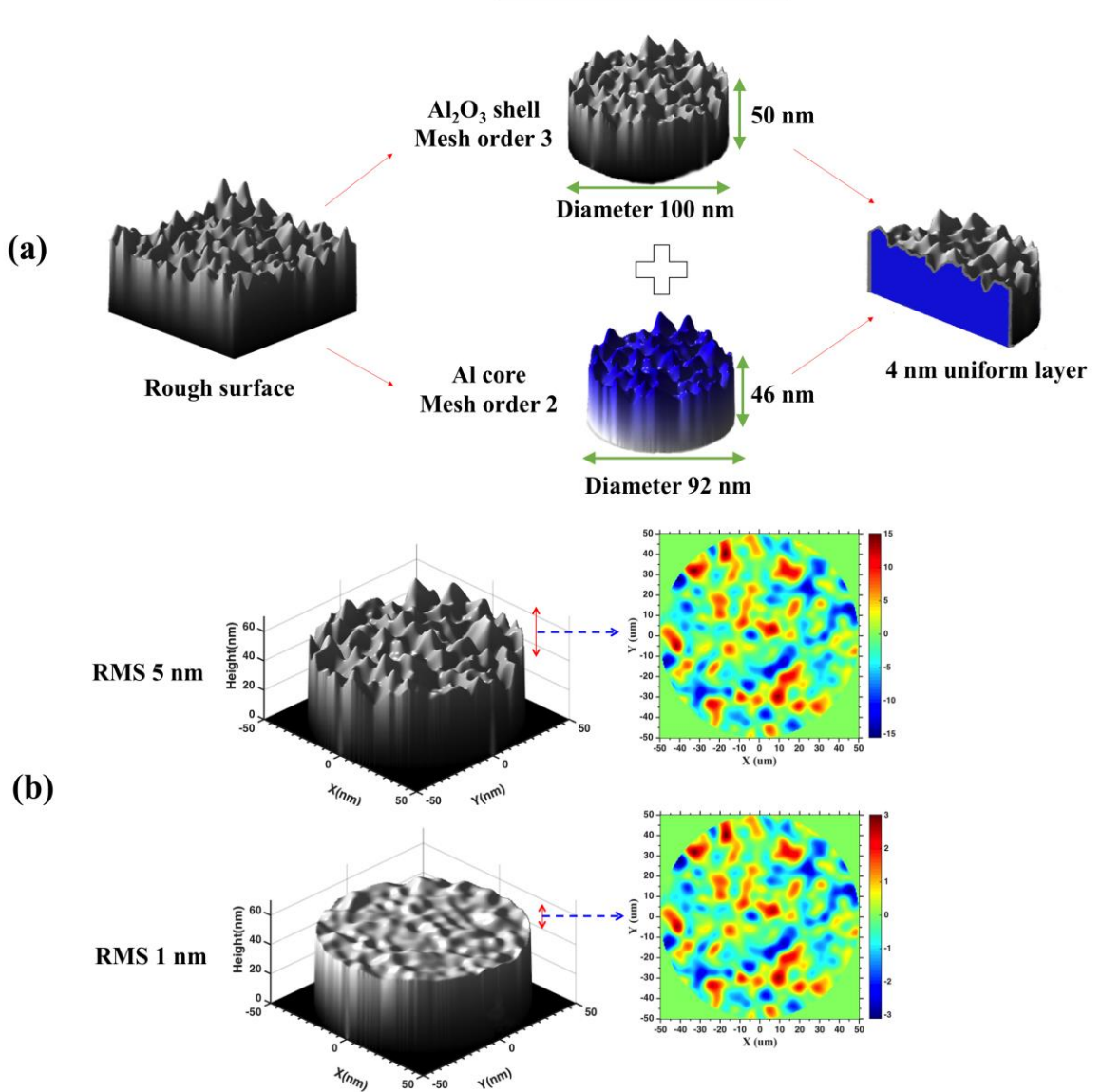


Figure 4.1. (a) Modeling schematic used to introduce the top surface roughness and to add the 4 nm native oxide layer to an Al nanodisk (diameter 100 nm, height 50 nm). **(b)** Exampled nanodisks with RMS 1 nm and 5 nm top surface roughness and their surface fluctuation amplitudes.

To fully gain insight on the effect of top surface roughness on the plasmonic properties of NPs, only the random amplitudes of the rough surface (i.e. the RMS value) varies. The surface fluctuation with RMS values equal to 1 nm and 5 nm are given as examples in [Figure 4.1b](#). As it can be seen from the colormap, the amplitudes of surface fluctuations increase without damaging the top morphology when the RMS value increases from 1 nm to 5 nm. Here, it should be emphasized that the random number matrix used to produce the surface roughness is uniformly distributed. Therefore, the total average value is maintained as zero

when the RMS amplitude change, which guarantees that the total volume of the material (Al or Al₂O₃) is kept constant at all time. In addition, the calculation was done with 0.5 nm minimal mesh size in the modeling region. To obtain the scattering spectrum of an isolated nanodisk, total-field scattered field (TFSF) source was used with boundary conditions of perfect matched layer (PML) at x, y and z directions. For periodic structures, the plane wave source was used with periodic boundary conditions at x and y directions, and PML at z direction.

4.3. Roughness effect on isolated nanodisk

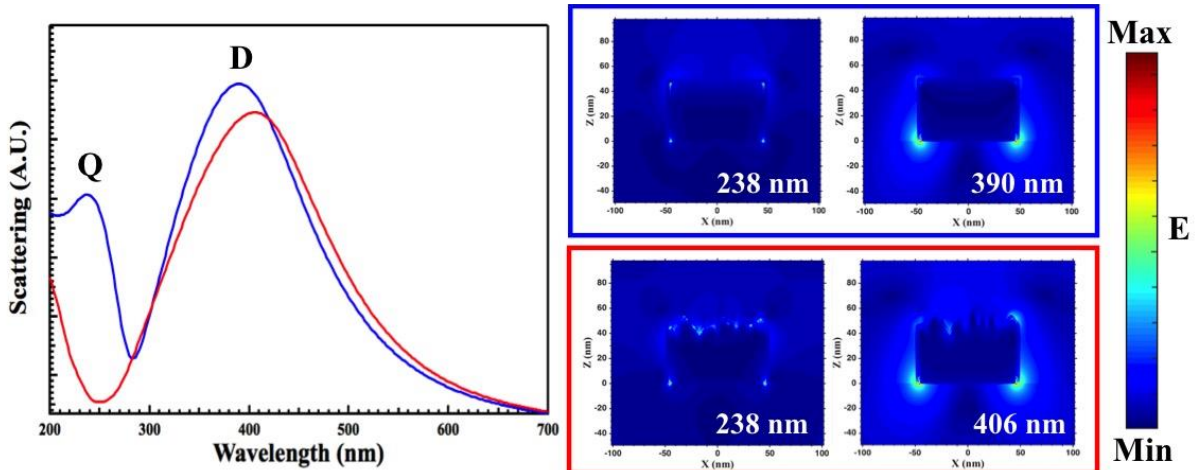


Figure 4.2. (Left) Calculated scattering spectra of an isolated nanodisk (diameter 100 nm) on the quartz substrate with top surface roughness RMS 0 nm (blue) and 5 nm (red). (Right) Electric field distribution of isolated 100 diameter nanodisk with top surface roughness RMS 0 nm (blue box) and 5 nm (red box). The inset gives the corresponding wavelength of the excitation. The polarization is along x direction, and the area below Z = 0 nm stands for the quartz substrate.

The top surface roughness effect on the scattering spectrum of an isolated Al nanodisk with diameter 100 nm is shown in Figure 4.2. For the single nanodisk with smooth top surface (*i.e.* RMS 0 nm, blue line in Figure 4.2), two obvious peaks appear at 238 nm (labelled as mode Q) and 390 nm (labelled as mode D). When a rough top surface is included on the isolated nanodisk (*i.e.* RMS 5 nm, red line in Figure 4.2), the mode D is redshifted with higher

FWHM, unveiling more losses due to the surface scattering on the rough surface. Mode D is also weakened as it decreases in intensity. Mode Q is greatly decreased with roughness as it almost vanishes away. By investigating the electric field (E-field) distribution in the vicinity of the nanodisk without top surface roughness, two bright and intense hot spots oriented toward the air side are observed for mode Q, while the hot spots are oriented near the substrate for mode D. In contrast to the hot spots focused on the top corners of flat nanodisk, more hot spots are created on the top surface by introducing the roughness. Meanwhile, no distinct effect is observed on the distribution of hot spots located near the substrate in the appearance of top surface roughness. The confinement of the near field is also revealed, especially for the mode Q at 238 nm where it is confined in the oxide layer. The origins of the modes labelled D and Q related here are explained in the following.

4.4. Substrate influence and Fano lineshape

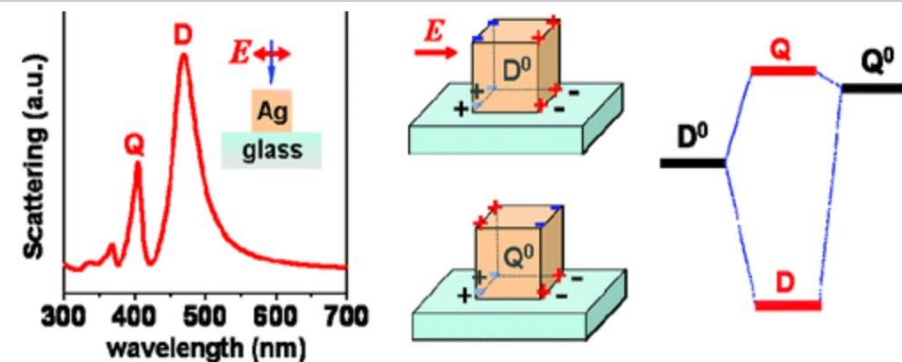


Figure 4.3. Illustration of Fano lineshape in the scattering spectrum of an Ag nanocube due to the substrate-induced symmetry breaking and interferences between D⁰ and Q⁰ modes. Figure extracted from reference [100].

By analysing the orientation of the hot spots for the two modes and the Fano lineshape in Figure 4.2, it can be figured out that the mode Q is actually a substrate-induced resonance, and the mode D is the dipolar mode sustained by the nanodisks.^{100,101} Indeed, symmetry breaking introduced by an adjacent dielectric plane (the substrate) underneath the NP is known to introduce coupling and hybridization of the plasmon modes sustained by the NP. This effect is high for nanostructures with a large contact area adjacent to the dielectric plane.¹⁰² For a nanodisk, the nearby dielectric environment under the NP mediates an

Chapter 4

interaction between bright dipolar and dark quadrupolar modes, resulting in bonding and antibonding hybridized modes. As shown in the following, the Fano resonance dominating the scattering spectrum is linked to the interference of these modes. This effect of interference is illustrated in [Figure 4.3](#), here for Ag nanocubes, taken from reference 100.

The scattering spectra of isolated Al nanodisk with or without a quartz substrate as a function of the diameter are calculated, as shown in [Figure 4.4](#). Without the quartz substrate, the scattering spectra of isolated Al nanodisks (black line) show only one peak, regardless of the diameter, attributed to the usual dipolar mode D. With increasing size of the nanodisk, this plasmonic resonance is shifted towards higher wavelengths and broadened due to phase retardation.

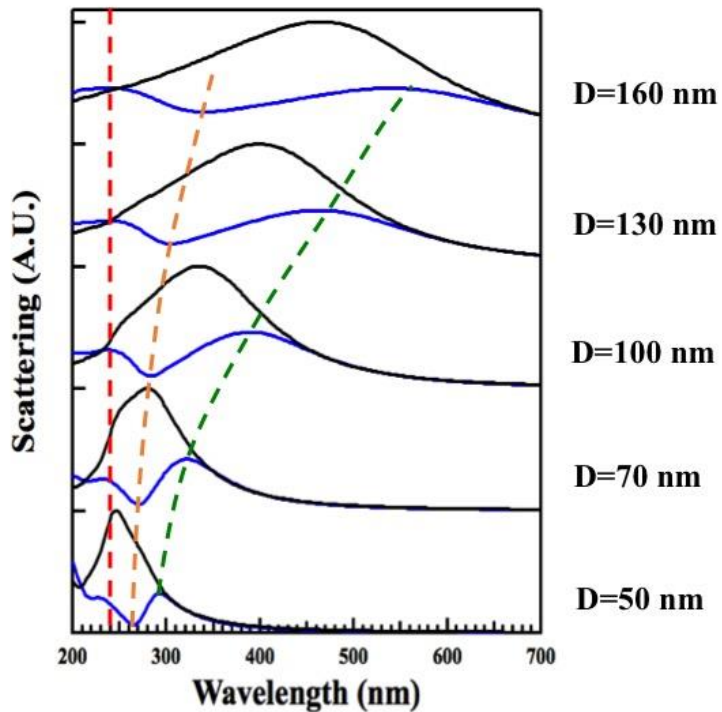


Figure 4.4. Simulated scattering spectra of isolated Al nanodisk (RMS 0 nm, height 50 nm) as a function of diameter with (blue) and without (black) substrate. The spectra of isolated nanodisk in same diameter are normalized to the maximum of the one without substrate, and then the spectra of nanodisks in different sizes are shifted for better vision. Corresponding diameters are indicated on the right. View guiding line for mode Q (vertical red dashed line at 240 nm), mode D (green dashed line), and the Fano dip (orange dashed line).

When the calculations are done taking into account of the quartz substrate, two plasmonic resonances are unveiled as shown in [Figure 4.4](#). The mode Q emerges at the shorter wavelength side of mode D. Due to the substrate effect and the subsequent interference discussed above, the resonance of mode D is redshifted (conveniently checked by the green dashed line in [Figure 4.4](#)) and attenuated. Moreover, the mode D is also narrowed comparing to the relevant spectrum without substrate. As for the mode Q around 240 nm, it is found that the peak wavelength does not shift much when the diameter of nanodisk increases from 50 nm to 160 nm, as confirmed by the red dashed line in [Figure 4.4](#). The broadening mode Q with increasing diameter is also revealed by the orange dashed line in [Figure 4.4](#). Furthermore, by comparing the total spectral width of free-standing nanodisk and the one of nanodisk with a quartz substrate, it is easy to realize that the appearance of substrate actually causes a Fano shape on the spectrum of free standing nanodisk, which finally brings about the new mode Q of quadrupole. As a matter of fact, it is very interesting to note that this mode Q sustained by Al nanodisks has already been observed experimentally before, although it is weak for the Al NP with low height.⁷² And it has even been used for the deep-UV SERS in the periodic Al NP array with large height, where mode Q is relatively strong.^{40,41}

To further ascertain the origin of modes Q and D, the charge distribution has been calculated by taking the divergence of the electric field, using the embedded analysis group in the software. The obtained results are plotted in [Figure 4.5](#). For the nanodisk with flat surface (blue box), it is obvious that mode Q has a quadrupolar behavior as unveiled by the spatial distribution of charge in [Figure 4.5a](#). And mode D corresponds to the dipolar charge distribution of the plasmonic dipolar mode sustained by the Al nanodisk, as shown in [Figure 4.5b](#). When a top surface with 5 nm RMS value roughness is imposed on the nanodisk, the top surface charge distribution is totally distorted by the surface roughness, as can be clearly compared in the XZ profiles of [Figure 4.5 c-d](#). Meanwhile, the charge distribution on the bottom surface of Al nanodisk seems to be less influenced. Artificial perturbation arises due to the discretization of FDTD cubic mesh to the non-cubic shape of the nanodisk.

Once that we understand the nature of the quadrupolar mode Q and the dipolar mode D, it is readily to comprehend the influence of top surface roughness on the plasmonic resonances of Al nanodisk. The oscillation of the free electron inside the nanodisk is confined by the geometry of the NP, therefore any change of the surface topology will alter the spatial distribution of charges. Due to the hybridization effect, mode Q is more sensitive to the top

Chapter 4

surface charge distribution, and consequently to the top surface roughness. As a result, the charges on the top surface are no longer fully located on the edge of nanodisk, and they are distributed more dispersedly on the rough surface. Therefore, mode Q will be highly decreased by dephasing due to this perturbation to top charge distribution. As for the mode D, it is more affected by the bottom surface charge distribution. The top surface roughness will weaken the collective oscillation of free electrons. The more radiative damping and diffusion scattering of the roughened nanodisk result in the redshifted and broadened mode D with decreased scattering in [Figure 4.2](#).¹⁰³

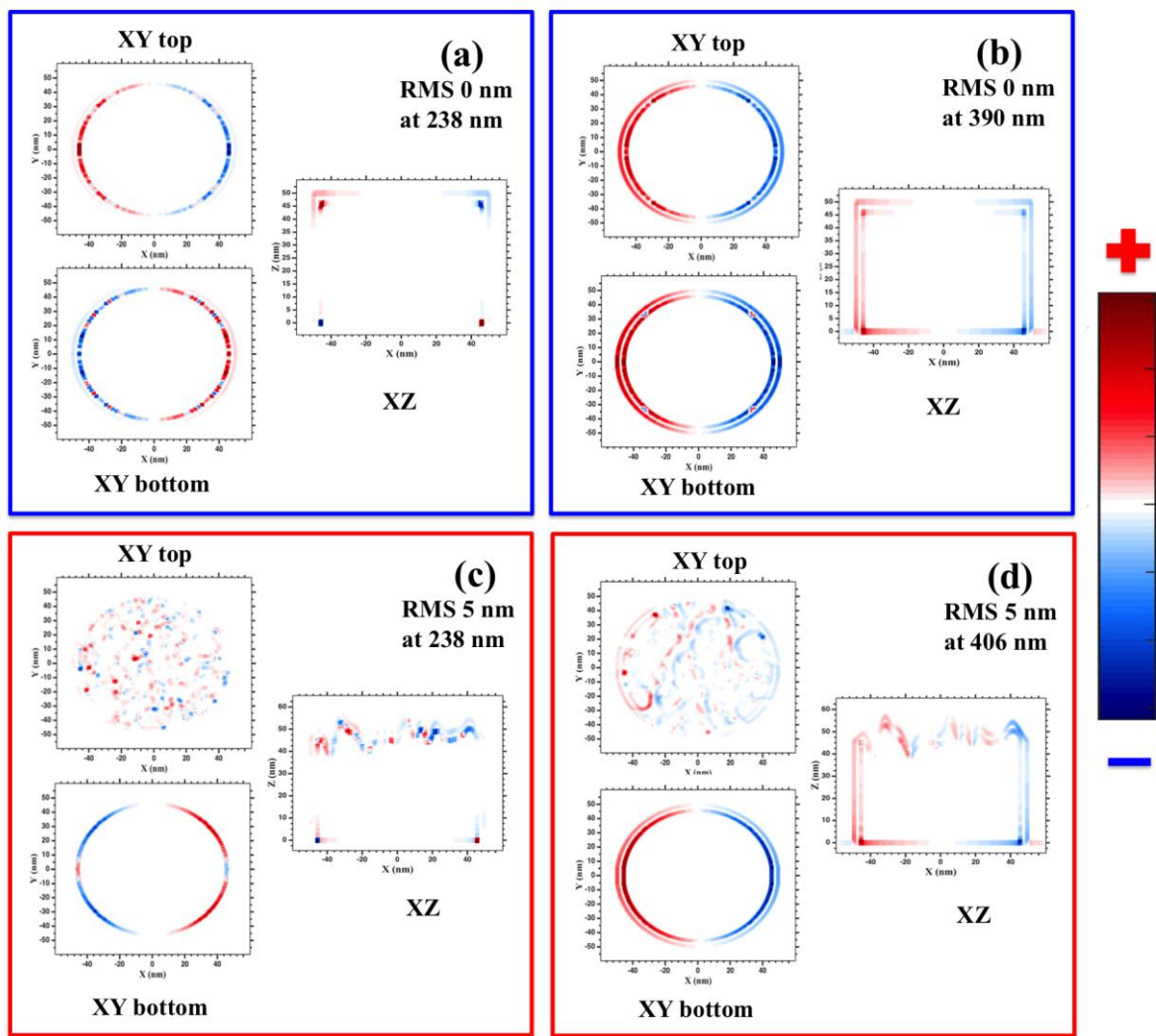


Figure 4.5. Calculated charge distribution of an isolated nanodisk with diameter 100 nm on the quartz substrate without (blue box, (a) and (b)) and with (red box, (c) and (d)) top surface roughness. The exciting wavelength is inserted in the box with three profiles of XY top surface ($Z=46$ nm), XY bottom surface ($Z=0$ nm), and XZ profile ($Y=0$ nm).

4.5. Generalization to periodic arrays

4.5.1. Coupling of modes in periodic array

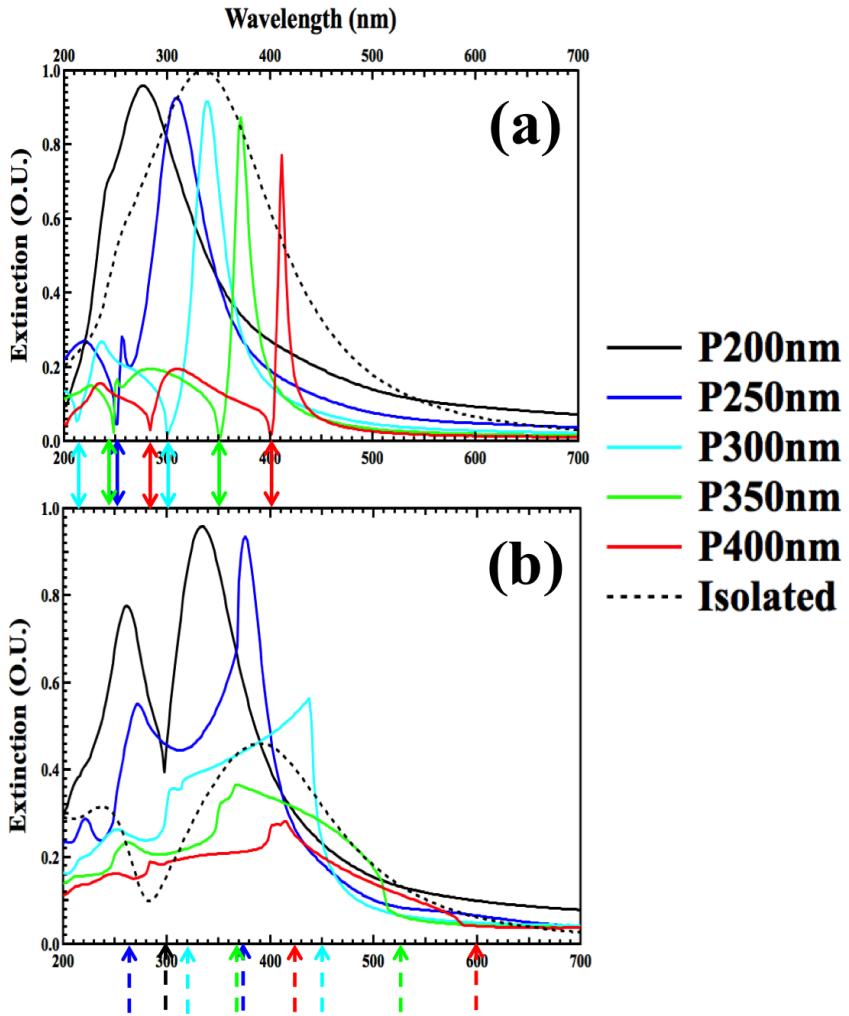


Figure 4.6. Calculated extinction spectra of periodic Al nanodisk (diameter 100 nm, without roughness) array with different pitches (P) from 200 nm to 400 nm without (a) and with (b) substrate; the spectra of isolated nanodisk are normalized to the maximum of the one without substrate. The arrows with solid lines indicate the lattice modes from the air side, and the arrows with dashed lines indicate the lattice modes from the substrate side. The color of each arrow corresponds to the associated spectrum.

A last important thing to consider before comparing our calculations with experiments is that our lithographed Al NPs are arranged in arrays, and each NP will be influenced by

Chapter 4

neighbouring NPs. In a periodic array, grating effect will appear due to the strong far-field diffractive coupling. This is so-called lattice mode in plasmonic literatures, which is actually a hybridized mode due to the coupling between grazing diffractive modes (or Rayleigh anomaly in lattices, depending on the pitch of the array) and plasmonic resonances. The in-plane incident wavevector \mathbf{k}_{inc} and diffracted wavevector \mathbf{k}_{ij} are linked with the diffraction orders {i, j} by^{6,104}

$$\mathbf{k}_{ij} = \mathbf{k}_{inc} + i \frac{2\pi}{d_1} \mathbf{u}_1 + j \frac{2\pi}{d_2} \mathbf{u}_2 \quad (4-1),$$

where d_1 (d_2) is the array pitch along the direction of the unit vector \mathbf{u}_1 (\mathbf{u}_2). For the square array with $d_1=d_2=P$ at the normal incidence ($\mathbf{k}_{inc} = 0$), the grazing diffracted wave with $|\mathbf{k}_{ij}| = \frac{2\pi n}{\lambda}$ will propagate in the plane of nanostructures without being radiated back into the free space. Therefore, the wavelength of lattice modes will occur at

$$\lambda = \frac{P \times n}{\sqrt{i^2 + j^2}} \quad (4-2),$$

where n is the refractive index from the air side ($n=1$) or from the quartz substrate side ($n \approx 1.5$). When the wavelength of lattice mode matches with the broad plasmonic resonance of single NP, a Fano-shape resonance will emerge in the extinction spectrum due to the hybridized nature of lattice modes.

We investigate here the effect of Al NPs with array configuration on the quartz substrate, which is the real experimental configuration, combined with the effect of top surface roughness. First of all, to decompose the effect of lattice modes, periodic arrays with flat top surface are simulated without or with substrate, and the results are shown in [Figure 4.6](#). Without the substrate, a continuously redshifted peak is evidenced with increasing pitch as displayed in [Figure 4.6a](#). The discrete lattice modes superimposed on the unique broad plasmonic resonance of single Al nanodisk without substrate are clearly observed, leading to the asymmetrical shapes of hybridized modes. As predicted by [Equation 4-2](#), the wavelengths of lattice modes from the air side ($n=1$) are indicated by the arrows with solid lines. In detail, obvious Fano shapes appear at 250, 300, 350 and 400 nm in the spectra of pitch 250, 300, 350 and 400 nm respectively. These wavelengths correspond to the (1, 0) or (0, 1) lattice mode from the air side. Moreover, (1, 1) lattice modes from the air side also exist at 212, 248 and 283 nm for pitch 300, 350, and 400 nm respectively. Additionally, the NP density per unit area also decreases with increasing pitch, which results in less light scattered and absorbed

per unit area. That is why the main peaks show a slowly decreased intensity with increasing pitch. The hybridization of plasmonic resonances are very strong for higher pitch, giving rise to very nice and sharp lattice resonances, especially for pitch of 350 and 400 nm, with Q factor equals to 30, which is very high for Al plasmonic dipolar resonances.

When including the quartz substrate in the simulation, mode Q from 200 nm to 280 nm located on the shorter wavelength side of mode D arises in the spectrum of single nanodisk as shown in [Figure 4.6b](#). Therefore, now we have to consider the coupling of lattice modes on the two different modes Q and D. Moreover, two kinds of lattice modes both from quartz ($n \approx 1.5$) and air ($n=1$) side appear in the extinction spectra. Using [Equation 4-2](#), the wavelengths of lattice modes from the substrate side are indicated by the arrows with dashed lines in [Figure 4.6b](#). For the coupling with mode D in the periodic array, the (1, 0) or (0, 1) lattice mode from the quartz side is exactly distinct at 375, 450, 525, and 600 nm respectively in the spectrum of corresponding pitch 250, 300, 350, and 400 nm. The slightly blueshifted lattice modes around 525 nm and 600 nm in [Figure 4.6b](#) are due to the decreased refractive index of quartz substrate at longer wavelength. When the lattice mode wavelength matches with mode Q from 200 nm to 280 nm, an enhanced peak will appear in the corresponding range. For the spectrum of pitch 200 nm, the first order lattice mode from the quartz side at 300 nm and from the air side at 200 nm, which centers the peak of mode Q, results in an extremely strong peak of mode Q with a clear Fano shape due to the enhancement of lattice modes at two ends. For the spectrum of pitch 250 nm, the (1, 1) mode from quartz side at 265 nm combining with the (1, 0) or (0, 1) lattice mode from air side at 250 nm result in a very intense peak of mode Q around 270 nm. Due to the interference of various modes, the spectra in [Figure 4.6b](#) show more complex signatures than [Figure 4.6a](#). Nevertheless, based on the spectrum of single nanodisk and comparing with [Figure 4.6a](#), similar analysis can be executed using lattice mode to explain the spectra in [Figure 4.6b](#). For instance, the (1, 1) mode from the air side at 248 nm for pitch 350 nm also gives rise to a distinct peak around 250 nm in [Figure 4.6b](#). Unlike slowly damped peaks in [Figure 4.6a](#), the extinction peaks are extremely weakened when the pitch exceeding 250 nm. Beside mentioned reason of the decreased NP density per unit area, this is probably due to the induced loss by the substrate both for mode D and mode Q. This weakening interaction can be also demonstrated in [Figure 4.2](#) by the decreased scattering intensity of spectra considering with the quartz substrate.

Chapter 4

In the following part, we are going to investigate the effect of top surface roughness on the periodic arrays with pitch equal to 200 nm and 250 nm (the spectra display intense extinction peaks both for mode Q and mode D), and also with pitch 400 nm (the spectrum displays weak extinction peaks both for mode Q and mode D). Artificial roughness with RMS value from 0 to 5 nm is taken into account in the calculations. Since the experimentally fabricated Al NP shows a surface roughness about 5 nm, as we have discussed in [Chapter 1](#) and [Chapter 3](#), we will extract the spectra of perfect disk (RMS 0 nm) and the roughened disk (RMS 5 nm) and compare them with the experimental spectra. The Al nanodisk arrays used in the experiments were fabricated by the standard EBL procedure on quartz substrate followed by an annealing treatment at 400 °C for 5 minutes. As discussed in [Chapter 3](#), this annealing step improves the quality of plasmonic resonances from Al nanodisks thanks to the diminished number of grain boundaries in the metallic core.⁷⁹

4.5.2. Experiments: pitch 200 nm

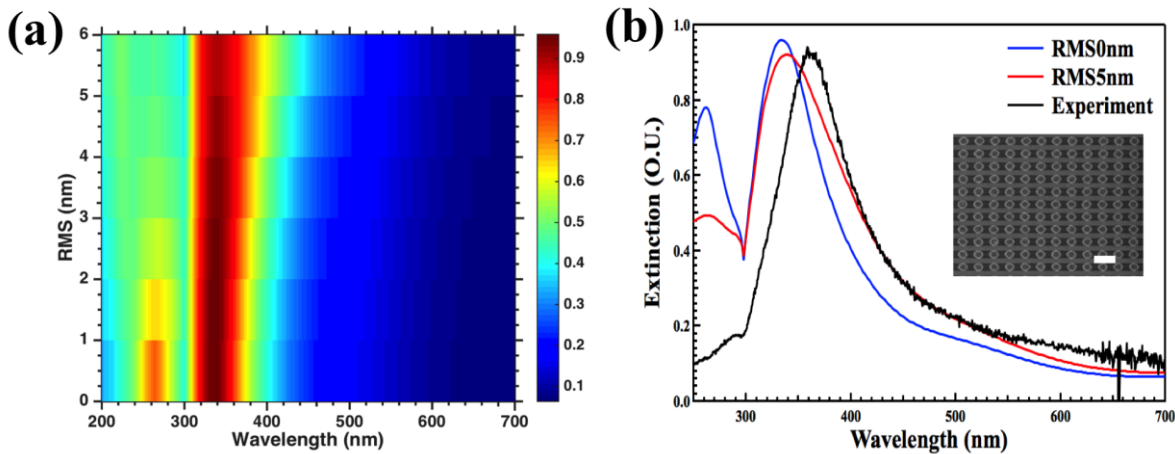


Figure 4.7. (a) Calculated extinction spectra of Al nanodisk array (diameter 100 nm and pitch 200 nm) as a function of RMS value. **(b)** The calculated extinction spectra of RMS 0 nm (blue) and RMS 5 nm (red) are compared with the experimental result (black). Inset SEM image shows the fabricated array. Scale bar 250 nm.

The extinction spectra of periodic array (diameter 100 nm) with pitch 200 nm as the function of RMS value are simulated and plotted in [Figure 4.7a](#). Here, we emphasize again that the total volumes of Al and Al₂O₃ are fixed as a function of the RMS value, therefore here the

only changing parameter is the surface roughness. In the spectrum of the smooth nanodisk (RMS 0 nm), two distinct peaks are observed: the peak at 262 nm corresponding to the quadrupolar mode Q and the peak at 334 nm corresponding to the dipolar mode D. By comparing with the spectrum of RMS 5 nm in Figure 4.7b, it is obvious that with increased top surface roughness, the dipolar peak is broadened and redshifted from 334 nm to 340 nm with decreased intensity due to the scattering losses on the roughened surface. Meanwhile, the peak of mode Q at 262 nm is greatly weakened with increasing surface roughness. In experiment, this peak at shorter wavelength is even more faded, although there is still an obvious Fano dip at 300 nm because of the lattice mode from the substrate side. By considering the top surface roughness of 5 nm, the calculated spectra become much closer to the experimental result. It is also reasonably deduced by comparing the spectra in Figure 4.7b that losses due to the surface roughness explain the disappeared peak of higher mode Q in the experimental spectrum. A discrepancy still exists between the calculated and experimental spectra. This can be ascribed to various reasons in the experiment like manufacturing error (e.g. the size distribution of nanodisks), and the suffering of grain boundaries inside NPs.

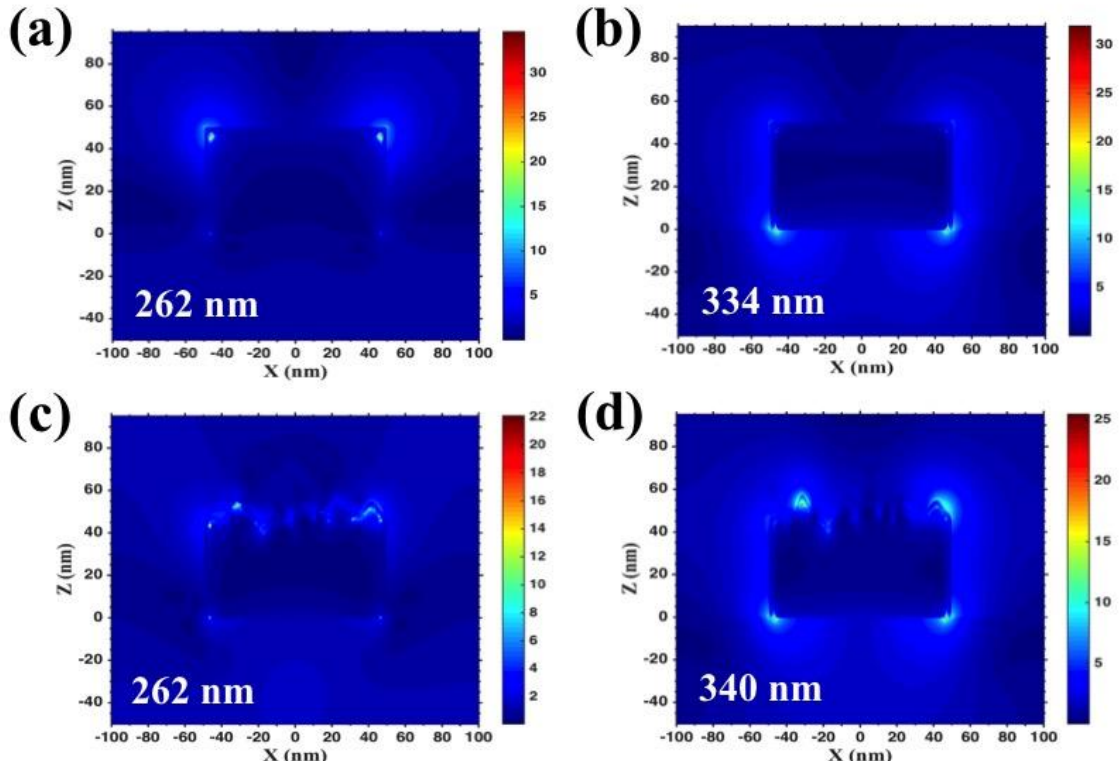


Figure 4.8. Calculated E-field distribution in the XZ plane of Al nanodisk array (diameter 100 nm and pitch 200 nm). Cross sections of E-field intensity with top surface roughness of RMS 0 nm (excited at 262 nm (a) and 334 nm (b)) and RMS 5 nm (excited

Chapter 4

at 262 nm (c) and 340 nm (d)). The polarization is along x direction, and the area below Z = 0 nm stands for the quartz substrate.

The calculated E-field distributions with (RMS 5 nm) and without (RMS 0 nm) roughness at two resonance wavelengths are displayed in [Figure 4.8](#). As shown in [Figure 4.8a](#), two top corners of the smooth nanodisk concentrate more energy than the corners near the substrate when excited at 262 nm corresponding to the mode Q. As for the rough nanodisk also excited at 262 nm, the hot spots on the top rough surface are no longer merely located at the corners. They are more dispersedly located on the randomly distributed sharp tips on the top rough surface. Meanwhile, the maximal electric field intensity is also reduced with the appearance of roughness, as comparing [Figure 4.8a](#) with [Figure 4.8c](#). Under the illumination at 334 nm corresponding to the dipolar mode D, hot spots are mostly focused on the bottom corners of the smooth nanodisk touching the substrate as shown in [Figure 4.8b](#). By introducing a 5 nm RMS value to the top surface ([Figure 4.8d](#)), more hot spots appear on the top surface, and the E-field maximal intensity is also diminished due to the roughness-induced losses.

Furthermore, hot spots are only located at corners of perfect nanodisk without the top surface roughness and the field distribution is more symmetric. By introducing a roughness of 5 nm RMS value to the top surface, hot spots on the top surface are randomly distributed with lower intensity and the electric field is distorted spatially by the roughness. The decreased maximal electric field intensity can be partially attributed to the rounded corners produced by the top roughness as shown in [Figure 4.8 b](#) and [d](#). However, due to the roughness, more hot spots on the top surface are created with enlarged active areas, which indicate the potential advantage of rough surface on near-field sensing. For example, for SERS applications, the area with enhanced electric filed of the dipolar mode ([Figure 4.8b](#)) is more located inside the substrate, which means more plasmonic losses. Moreover, there will be less enhancement to the Raman scattering of molecules due to the inaccessibility of molecules, which is mostly spreading on the surface of substrate, to the hot spots inside the substrate. Notwithstanding, the electric field intensity appears relatively stronger for flat nanodisk (1.3 times for mode D, shown in [Figure 4.8 b](#) and [d](#)). Therefore, it is probably not suitable for the SERS application. On the contrary, hot spots created on the top rough surface will be preferred for sensing ([Figure 4.8d](#)). At the same time, the large covering area of hot spots on the rough surface

would compensate the drawback of decreased E-field intensity. In fact, the first SERS phenomenon was obtained on a rough Ag electrode.¹⁰⁵ It is also the same principle to use an index-matching layer to reduce the energy confined in the substrate in the plasmonic sensors.¹⁰⁶

4.5.3. Experiments: pitch 250 nm

Results from different pitch (250 nm) also unveil the same mechanisms described above. The extinction spectra from calculations as the function of RMS value are plotted in Figure 4.9a, and the spectra are also compared with the experimental spectrum in Figure 4.9b. For the spectrum of the smooth disk (RMS 0 nm), two main peaks from lattice modes are observed: the peak at 270 nm of mode Q and the peak at 376 nm of mode D. By including the top surface roughness, the peak corresponding to higher mode around 270 nm is greatly weakened. Meanwhile, the peak around 376 nm is broadened and redshifted to 382 nm while experiencing a lowered intensity. Similar to the case of the 200 nm pitch, the calculated spectra become closer to the experimental results by considering the surface roughness in FDTD simulation, as compared in Figure 4.9b.

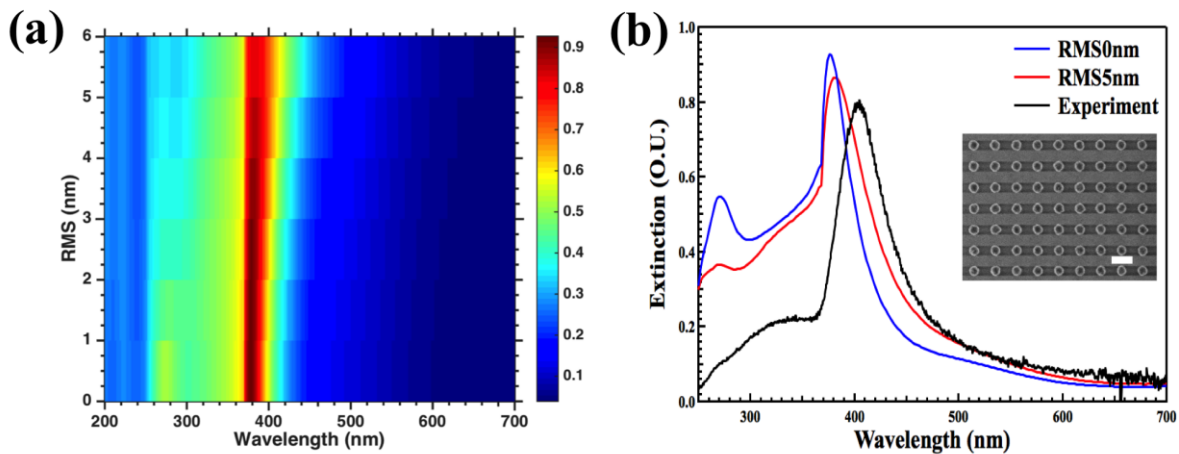


Figure 4.9. (a) Calculated extinction spectra of Al nanodisk array (diameter 100 nm and pitch 250 nm) as a function of RMS value. (b) Calculated extinction spectra of RMS 0 nm (blue) and RMS 5 nm (red) comparing with experimental result (black). Inset SEM image shows the fabricated array. Scale bar 250 nm.

The calculated E-field distributions with (RMS 5 nm) and without (RMS 0 nm) roughness at two resonance wavelengths are also displayed in Figure 4.10. The results are similar with the

case of pitch 200 nm, therefore we will omit the discussion here. Without the Al₂O₃ layer, the E-fields distributions are similar but with increased intensities.

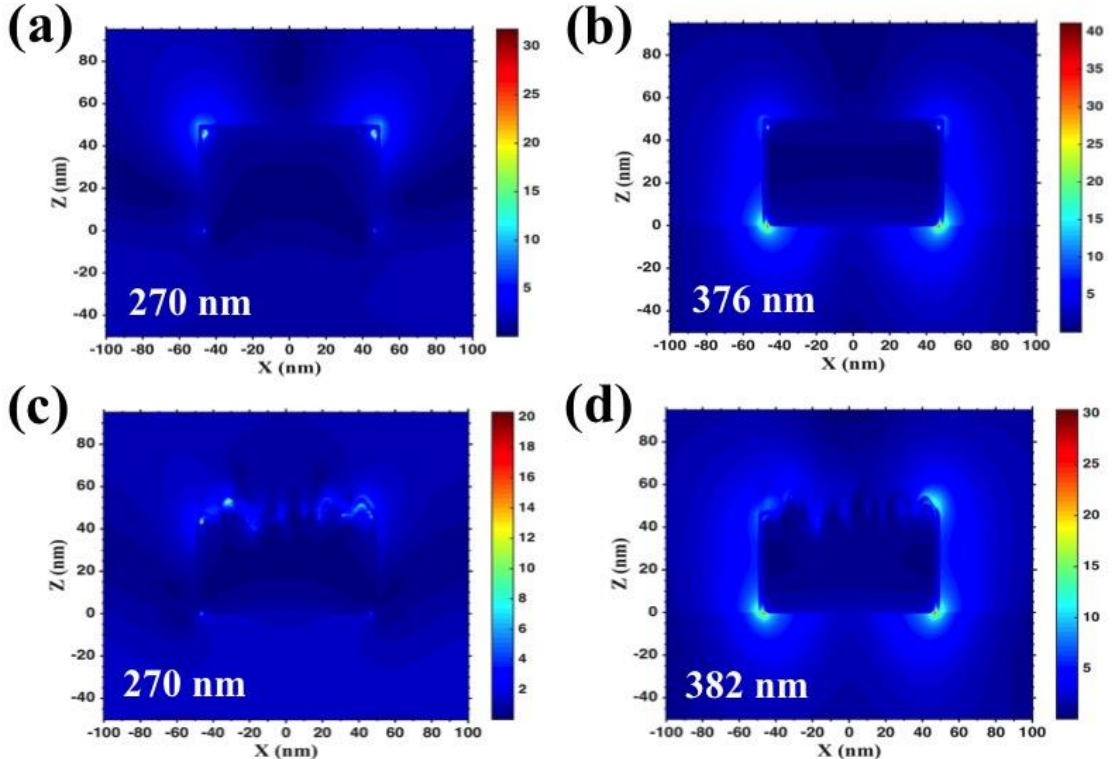


Figure 4.10. Calculated E-field distribution in the XZ plane of Al nanodisk array (diameter 100 nm and pitch 250 nm). Cross sections of E-field intensity with top surface roughness of RMS 0 nm (excited at 270 nm (a) and 376 nm (b)) and RMS 5 nm (excited at 270 nm (c) and 382 nm (d)). The polarization is along x direction, and the area below Z = 0 nm stands for the quartz substrate.

4.5.4. Experiments: pitch 400 nm

When the pitch is large, here for pitch 400 nm, the coupling between lattice modes and plasmonic resonances is low and results in the much weaker peaks both for mode Q and mode D, as already seen in [Figure 4.6](#). In this part, we are going to study the top roughness influence in the array with large pitch, so with lower extinction cross section. As proved in [Figure 4.11a](#), the mode Q around 250 nm experiences a continuously decreased intensity as obtained previously, although the peak intensity is relatively smaller. Due to the (1, 0) or (0, 1)

lattice modes from the air side at 400 nm and the (1, 1) lattice mode from the substrate side at 425 nm coupled with the plasmonic resonances, a peak with a flat top is produced in the extinction spectrum of smooth nanodisk. By comparing the peaks around 400 nm in Figure 4.11b, a broader peak without obvious diminution in the extinction intensity is acquired when the top surface roughness is included, possibly due to the much weaker intensity already in such large pitch. In experiments, the extinction spectrum shows even much lower intensity.

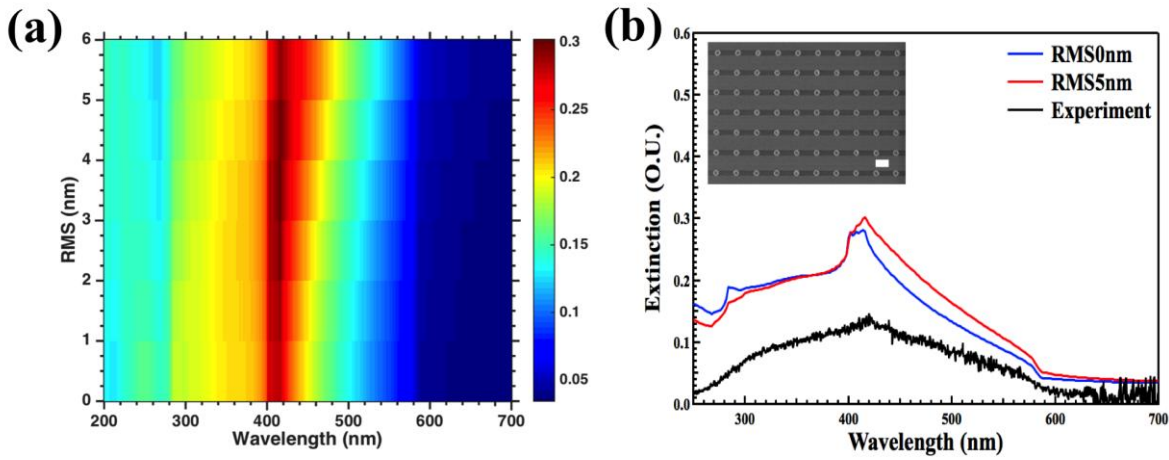


Figure 4.11. (a) Calculated extinction spectra of Al nanodisk array (diameter 100 nm and pitch 400 nm) as a function of RMS value. (b) Calculated extinction spectra of RMS 0 nm (blue) and RMS 5 nm (red) comparing with the experimental result (black). Inset SEM image shows the fabricated array. Scale bar 250 nm.

The calculated E-field maps in the vicinity of the Al NP with (RMS 5 nm) and without (RMS 0 nm) roughness at two resonance wavelengths are displayed in Figure 4.12. This time, the intensities of top hot spots and the ones of bottom hot spots display comparable values at the excitement of 400 nm, as shown Figure 4.12b. After roughening the top surface, the top hot spots even show a stronger intensity than the one of bottom hot spots. Generally speaking, the demonstrated tendency of the results is similar with the cases of other pitches that we already discussed above.

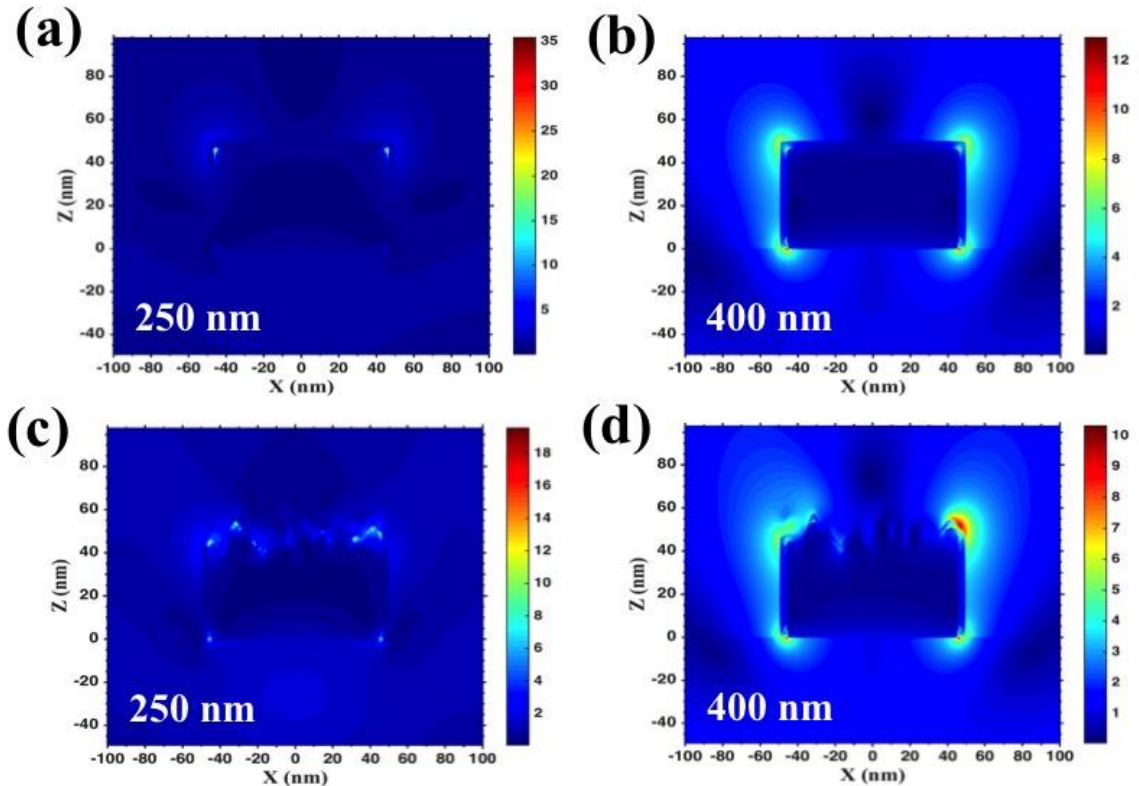


Figure 4.12. Calculated E-field distribution in the XZ plane of Al nanodisk array (diameter 100 nm and pitch 400 nm). Cross sections of E-field intensity with top surface roughness of RMS 0 nm (excited at 250 nm (a) and 400 nm (b)) and RMS 5 nm (excited at 250 nm (b) and 400 nm (d)). The polarization is along x direction, and the area below $Z = 0$ nm stands for the quartz substrate.

4.6. Conclusions

In conclusion, the nanoscale change induced by the roughness on the top surface of Al nanodisk with a uniform oxide layer were carefully studied by the FDTD calculation and the obtained results were confirmed by experiments on Al nanodisk arrays. The influence of top surface roughness on the Fano-shape plasmonic resonance of single Al nanodisk can be discussed on two main plasmonic modes: the substrate-induced quadrupolar mode Q and the dipolar mode D. The increased top surface roughness of Al nanodisk results in a broadened and redshifted dipolar peak of mode D with weakened intensity due to the roughness-induced plasmon losses. Meanwhile, the plasmonic resonance from mode Q at shorter wavelength is

greatly weakened with the appearance of top surface roughness. More hot spots are generated on the top rough surface and can be used, for instance, for Al based SERS in the near UV and visible region. In a closely packed periodic array, especially when the pitch (here 200 and 250 nm) is close to the wavelength of substrate-induced resonance, an intense peak corresponding to the higher mode Q emerges on the extinction spectrum. This peak is highly damped by the appearance of top surface roughness, which can be used to explain the disappeared peak in the experimental spectrum. Considering with the extreme sensitivity of mode Q in a closely packed array to the surface roughness, it might be applied as a signature to the quality of Al nanostructure top surface in the experiment. In the future, more features from Al surface roughness can be explored like plasmon waveguiding and the phase shifting for metasurface. Furthermore, the proposed modeling method can also be applied to various nanostructures with a shell in different geometries.

Chapter 5 Plasmonic resonances of uniformly disordered aluminium nanoparticle arrays

The different arrangements of constituents like atoms or ions in solid materials define the different states of matter. The long-range periodic arrangement brings crystals, while the amorphous solid is determined by a short-range order and a long-range disorder. Additionally, a third intermediate class known as quasicrystal resulted from the deterministic aperiodic structures has been found in recent years.^{107,108} Similarly, the optical properties of Localized Surface Plasmon Resonances (LSPR), which are collective oscillations of conduction electrons in the NPs (nano particles), can be engineered not only by the material, size, shape, and surrounding environment but also the arrangement of NPs. By positioning NPs into well-chosen periodic arrays, optical interferences in the array will result in a long-range radiative coupling and yield narrow LSPR known as lattice modes.¹⁰⁹ In contrast, when breaking the symmetry of the periodic array, difficulties and complexities arise both for theoretic and experimental analysis due to the suppression of unit cell, or apparition of disorder. However, owing to the rich physics and various potential applications, researches on the disordered photonic systems are now under active development.¹¹⁰

To date, various disordered structures have been studied, targeting applications like perfect focusing¹¹¹, light trapping¹¹², random laser¹¹³, and sensing¹¹⁴. Therefore, the impact of disorder on the plasmonic properties favored by metallic nanostructure arrays is an important issue, especially on aluminium nanostructures, which are less studied than noble metals. In practice, disorder will always be introduced to some content no matter in which method it is used for nanofabrications. Therefore, an improved insight into the influence of disorder to the plasmonic performance has been an important issue. Previous studies have proposed various methods to introduce a disorder like a random-walk method and giving part of NPs in a periodic array a random variation,^{115,116} however different results were observed. In this chapter, a simple algorithm is adopted to study

the influence of uniform disorder voluntarily created in Al nanoparticles arrays resorted to the flexibility and versatility of electron beam lithography.

5.1. How to generate uniform disorder?

The main idea is to give each NP in a periodic array a random parameter change, *i.e.* coordinate displacement, size variation, and rotation angle, thus these three kinds of uniformly disordered arrays were generated.

5.1.1. Sample fabrication

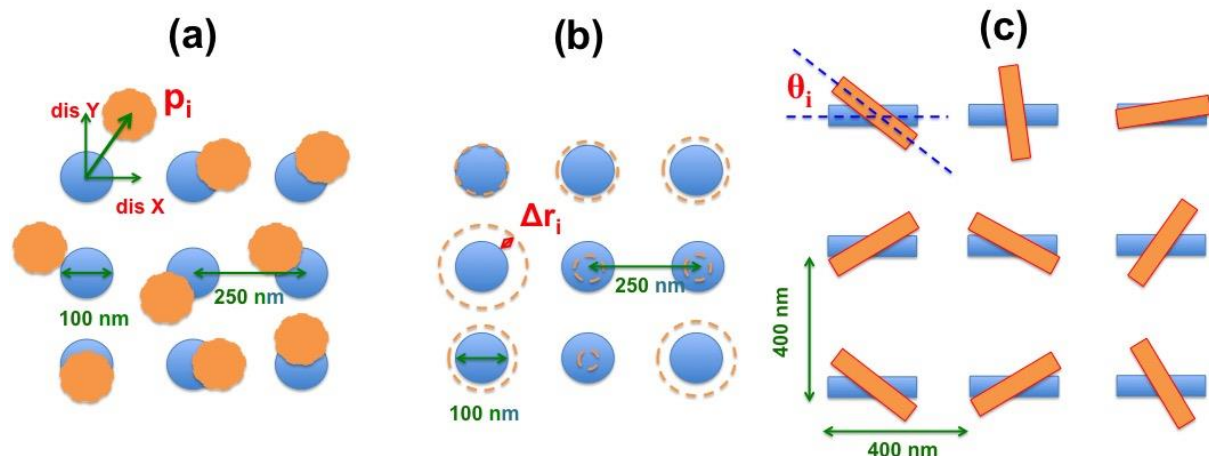


Figure 5.1. Schematic representation of the different approaches used to introduce randomness in a periodic array in term of (a) displacement, (b) size, and (c) rotation of nanostructures.

In experiment, the nanostructures (thickness is set to 50 nm) are arranged in $40 \times 40 \mu\text{m}^2$ square areas to facilitate subsequent optical measurements. Before the optical measurement, rapid thermal annealing has been done at 400 °C for 5 minutes in ambient air in order to increase the quality factor of plasmonic resonances.⁷⁹ For nanodisk arrays, the basic diameter was set to 100 nm with a center-to-center distance (or pitch) set to 250 nm or 400 nm. For the nanorod array, the width and length of nanorod are set to 50 nm and 140 nm respectively with a pitch of 400 nm for both the x and y axis.

Chapter 5

The schematic representation of the random generation based on a periodic array can be found in [Figure 5.1](#). Disordered patterns were generated by adding a random number to the basic parameter of each nanoparticle in the periodic array (movement both on the x and y direction for displacement disorder ([Figure 5.1a](#)), radius change on each nanodisk for size disorder ([Figure 5.1b](#)), and rotating angle along the long axis of each nanorod for rotation disorder ([Figure 5.1c](#))). The coordinates were obtained by the script of *Matlab* software and then inputted into the EBL system to generate designed patterns for experimental fabrications.

5.1.2. Rules to name the samples

Disordered maximal movement of each nanodisk increases from 0 nm to 100 nm with 25 nm interval for the periodic array with pitch 250 nm. The samples are named after **dis0nm**, **dis25nm**, **dis50nm**, **dis75nm** and **dis100nm** by the increasement of movement along the x and y axis from the original lattice position.

For size disorder, the radius of each nanodisk (basic radius 50 nm) in a periodic array is given a random change by a 10 nm step. The samples are named after **size0nm** (radius 50 nm), **size10nm** (radius varies from 40 nm to 60 nm), and **size20nm** (radius varies from 30 nm to 70 nm).

For rotation disorder, a maximum angle θ is chosen and each nanorod is randomly rotated along its long axis with an angle lying between $-\theta$ and θ . The samples were then named from θ ($=0, \pi/6, \pi/3, \pi/2$), i.e. **R0**, **R30**, **R60**, and **R90** with enhanced disorder.

5.2. Large-area FDTD Calculations

To rigorously model a uniformly disordered system, large-area FDTD simulations (about $10 \times 10 \mu\text{m}^2$) were done using the commercial software (*Lumerical FDTD solution*). A 4 nm thick uniform oxide layer of Al_2O_3 is included within each Al nanostructure in the array. For the nanodisk array with 250 nm pitch, 40 rows \times 40 columns (i.e. 1600 NPs) were simulated. For the nanorod array with 400 nm pitch, 25 rows \times 25 columns of NPs (i.e. 625 nanorods) were

placed in the simulation box. Perfectly matched layers (PML) are used at all boundaries and about 600 nm space was left between the PML boundaries in x and y directions and the domain of NPs to avoid artificial coupling. A minimum mesh of 1 nm was used in the whole simulation region. Normal incident plane wave (200-700 nm) was placed in the quartz substrate. Moreover, electric-field (E-field) distribution was achieved by the monitor placed at the interface between NPs and the substrate. In order to create a uniform disorder in the simulated nanostructure, we use the same procedure with the one described in the experimental method. Due to the large number of NPs involved in the calculation, the results obtained could ideally represent the disordered situation of our experiment. The author is grateful for the support provided by the ROMEO computing center of the University Reims Champagne-Ardenne (<https://romeo.univ-reims.fr/>).

5.2.1. Uniform disorder

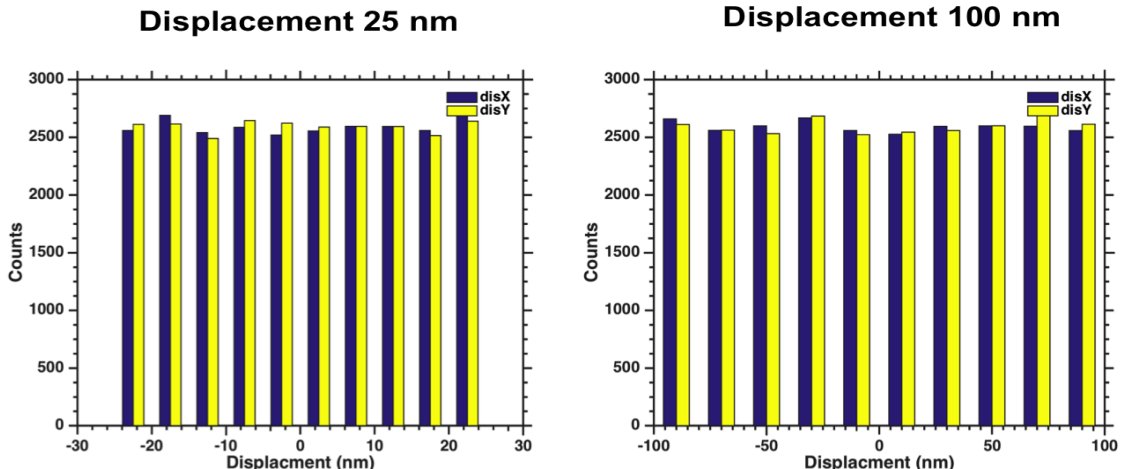


Figure 5.2. Examples of the statistical distributions of uniform random numbers used for the x and y displacement (disX and disY, as shown in Figure 5.1a) for 25 nm and 100 nm of maximum displacement of nanodisks in the experiment.

Here, we emphasize that the random numbers generated are uniformly spaced (i.e. the average value is zero), which is also the reason why the disorder introduced in our study is called uniform disorder. Statistics on the random number distribution used in the experiment for x and y coordinate displacement is presented in Figure 5.2. It is obvious that random numbers are equally distributed between the positive maximum and the negative maximum. Thus, it results in an arithmetic average close to zero. The mean square error (MSE) on the parameter

Chapter 5

variation both in the experiment and simulation has also been calculated and can be retrieved in [Table 5-1](#), where it is tabulated for each pattern. The MSE value increases with the degree of disorder although the average value is maintained around zero. Meanwhile, it is worth noting that these MSE values are rather stable as the array size changes due to the algorithm used for random number generation. This is also confirmed by comparing the MSE value of simulation with the one of experiment, since the size of array in simulation is actually smaller than the one in experiment while the two values are still comparative. Therefore, these MSE values in the experiment could be employed to define the degrees of disorder and compared with other random structures.

Table 5-1. The calculated mean-square-error value on the parameter variation both in experiment and simulation for (a) displacement disorder ($MSE = \sum_{i=1}^{i=N} (P_i)^2 / N$), (b) size disorder ($MSE = \sum_{i=1}^{i=N} (\Delta r_i)^2 / N$), and (c) rotation disorder ($MSE = \sum_{i=1}^{i=N} (\theta_i)^2 / N$). N is the total number of NPs in the array.

(a)

MSE ($\times 10^3 \text{ nm}^2$)	dis0nm	dis25nm	dis50nm	dis75nm	dis100nm
Experiment	0	0.42	1.67	3.76	6.70
Simulation	0	0.41	1.63	3.67	6.52

(b)

MSE (nm^2)	size0nm	size10nm	size20nm
Experiment	0	33.1	134.3
Simulation	0	32.3	134.1

(c)

MSE (square of radian)	R0	R30	R60	R90
Experiment	0	0.09	0.37	0.83
Simulation	0	0.09	0.35	0.86

5.3. Displacement disorder

5.3.1. Periodic array

Considering an ensemble of NPs separated with a varying gap, the induced varying interparticle coupling will lead to a shift on the plasmonic resonance.¹¹⁷ The simplest example to intuitively observe this phenomenon is a periodic array, which induces a strong diffracted mode (lattice mode or Rayleigh anomaly) depending on the periodicity.^{118,119} This feature is attributed to the strong coupling between the plasmonic resonance sustained by nanoparticles in the array and the grating effect, determined by the periodic arrangement of NPs. The broad peak of LSPR combined with the narrow bandwidth of the lattice mode results in the sharp lineshapes in extinction spectra, as depicted in Figure 5.3. Here, periodic nanodisk (diameter 100 nm) arrays with different pitches were simulated, and the corresponding spectra are shown in Figure 5.3a. The calculated spectrum of individual 100 nm nanodisk is also displayed in Figure 5.3a. Beside a peak around 250 nm due to the appearance of substrate, a broad peak centered at 390 nm, in the near UV range, is corresponding to the dipolar resonance of NPs. These are already fully investigated in Chapter 4. Meanwhile, the experimental spectra are given in Figure 5.3b for a comparison.

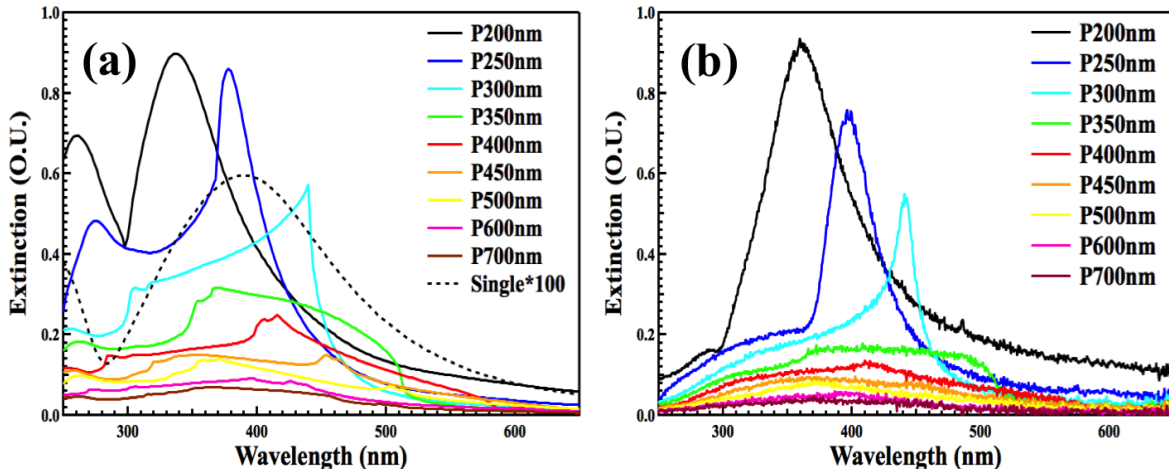


Figure 5.3. Simulated (a) and experimental (b) spectra of periodic Al nanodisk arrays with different pitches. Diameter is 100 nm and pitch (P) varies from 200 to 700 nm. The calculated spectrum of isolated nanodisk in 100 nm diameter is increased by 100 times.

The wavelengths of lattice modes with normal incident light are given by¹²⁰

$$\lambda = \frac{P \times n}{\sqrt{i^2 + j^2}} \quad (5-1),$$

Chapter 5

where P stands for the pitch of the array, n is the refractive index of air ($n=1$) or quartz ($n=1.5$), and (i, j) is the grating diffraction order. The first order lattice mode from the air side at short wavelength (300, 350, 400, and 450 nm) and from the substrate (quartz) side at long wavelength (375, 450, and 525 nm) are clearly observed.

For the peak at 260 nm (P200nm) and 276 nm (P250nm) in [Figure 5.3a](#), it is due to the strong coupling of NPs from a very closely packed periodic array to the substrate-induced mode. From the reduced peak intensity around 250 nm when the pitch is exceeding 300 nm, it could be deduced that this coupling effect is very sensitive to the pitch of the array. When the pitch is comparable to the peak wavelength (*i.e.* the quartz-induced Fano resonance around 250 nm from an isolated Al NP), the peak is slightly redshifted with increasing pitch (260 nm of P200nm to 276 nm of P250nm). However, when the pitch is beyond 300 nm, the decreasing coupling effect brings the peak back to 250 nm. As we have explained in the previous chapter, the disappeared peaks at shorter wavelength for pitch 200 and 250 nm in experiment could be attributed to the top surface roughness and the geometrical difference. From the well corresponded extinction spectra of simulations and experiments, it is meaningful to pay attention to several features. On the one hand, when the lattice modes match with the LSPR, peaks with enhanced intensities emerges in the extinction spectra due to the mentioned reasons. On the other hand, with increasing periodicity, the density of NPs per unit area is decreased. Thus, less light is scattered or absorbed in the array per unit area. This is the reason why all the extinction peak intensities fall as the function of pitch, as clearly shown in [Figure 5.3](#) both for simulation and experiment. For example, in the extinction spectra of the periodic array with 400 nm pitch (denoted as P400nm in [Figure 5.3a](#) and [Figure 5.3b](#)), although the first order lattice mode from the air side at 400 nm matches with the LSPR of single nanodisk, the peak intensity is still much weaker than the peaks measured for smaller pitches.

5.3.2. Radial distribution function

Lattice modes will eventually disappear if a displacement disorder is introduced in the NP array. In order to study the effect from this kind of disorder, we choose an initial periodic array with a pitch of 250 nm since it displays a strong lattice mode as shown above. To achieve different degrees of disorder, each nanoparticle of a particular sample is given a

uniform random displacement which varies from 0 nm to a maximal number lying between 0 (no disorder) to 100 nm (highest disorder) both at x and y direction simultaneously. Five samples with maximal random displacement of 0, 25, 50, 75 and 100 nm are shown in [Figure 5.4](#). With respect to the periodic structure dis0nm, the dis75nm and dis100nm samples have obviously lost their periodicities. Notice that some NPs may overlap when the displacement is larger than 75 nm. However, there are theoretically far less than 0.1% overlapped NPs for dis100nm.

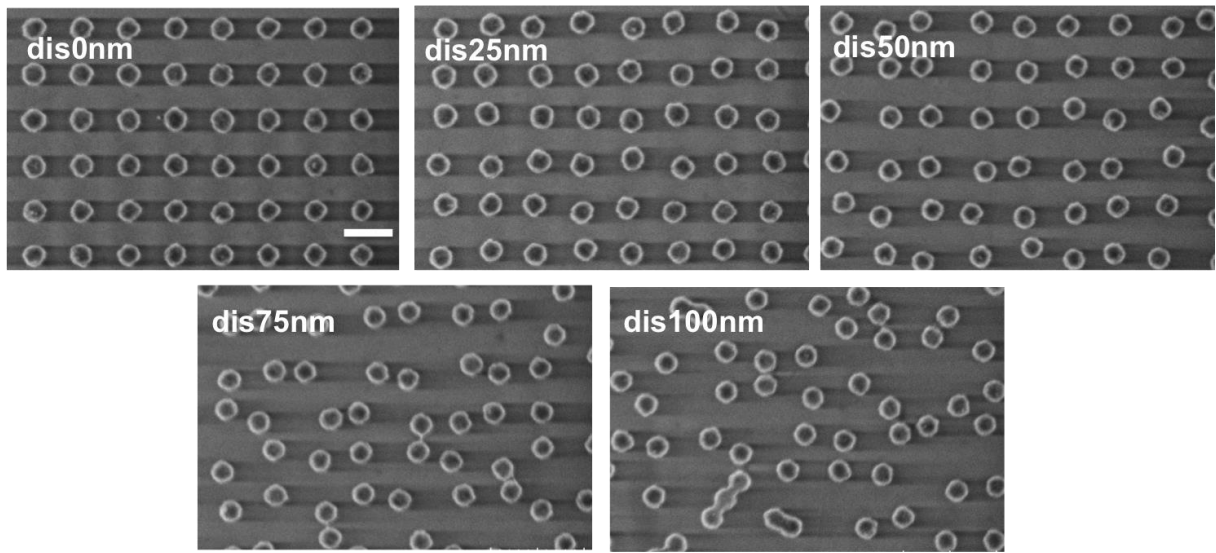


Figure 5.4. SEM images for nanodisk arrays (100 nm diameter, base pitch 250 nm) with different disorder. Scale bar 250 nm.

Radial distribution function $g(s)$ is usually used to describe the distribution of a random system¹²¹:

$$g(s) = 2\pi s \cdot \rho(s) \cdot ds$$

where s stands for the distance away from the center of a reference disk; ρ stands for the number density of nanostructures per unit area. A schematic representing its calculation is given in [Figure 5.5a](#). The averaged radial distribution function is calculated using the nanodisk coordinates generated for EBL fabrication, while its values are plotted in function of s/r (r is the radius of nanoparticles, *i.e.* 50 nm) for the five different samples in [Figure 5.5b](#). The g function of the periodic array (dis0nm) shows obvious regular peaks due to the lattice configuration. As the degree of displacement disorder increases, the g function becomes a linear relationship with the distance s . This indicates that the density ρ becomes constant through the whole area when the maximal random displacement of each nanodisk is set to 100 nm. Therefore, nanodisks get more and more homogeneously distributed in the spatial area with increasing displacement disorder.

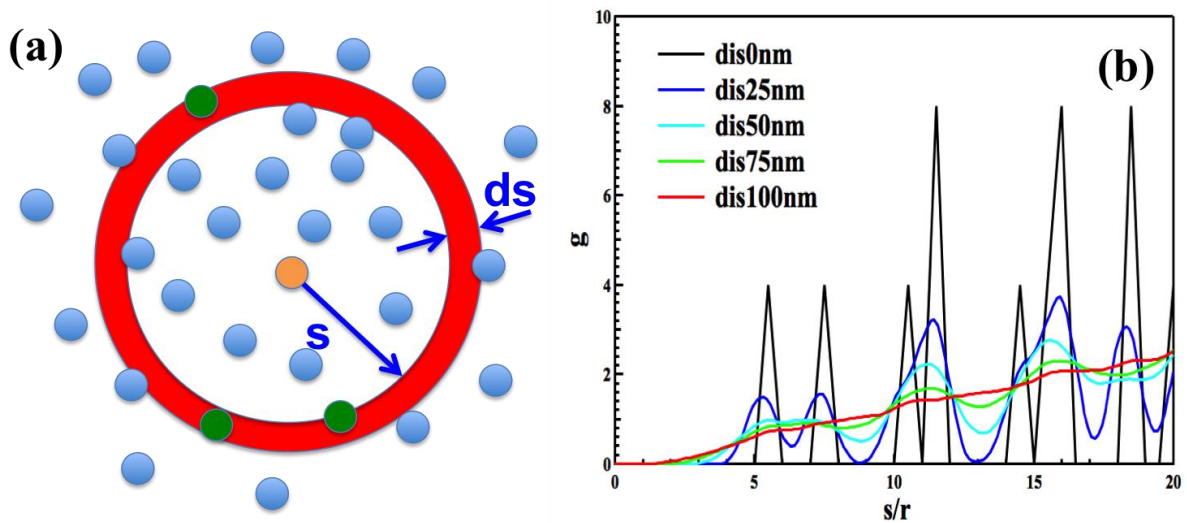


Figure 5.5 (a) Schematic representation of the approach used to calculate the radial distribution function. The orange disk stands for the reference disk, and the number of green disks stand for the value of g in the red area from the reference disk at a distance s . **(b)** Averaged radial distribution function for nanodisk array (100 nm diameter, 250 nm pitch) with different displacement disorder calculated from experimental coordinates. r is the radius of the nanodisk, i.e. 50 nm.

5.3.3. Influence on optical properties

Extinction spectra from both simulations and experiments are presented in Figure 5.6. As expected, the lattice modes are continuously weakened when introducing the uniform displacement disorder. Considering the peak at 276 nm in simulation (Figure 5.6a), it is slightly blueshifted due to its special nature as already explained in Figure 5.3. Indeed, this peak is extremely sensitive to the pitch of a periodic array. Whether the separation of NPs is beyond or below to 250 nm, the peak is always blueshifted towards to 250 nm. Therefore, when the collective oscillation is destroyed, the peak is trending to be blueshifted and depressed. By increasing the displacement disorder, the optical signature of lattice mode around 378 nm in simulation becomes broader and lower in intensity, while the resonance wavelength remains almost constant. In disordered samples, the coherent oscillation in the array is reduced. The varying interactions from continuously spaced NPs are linked to the reduction of the lattice effect. Moreover, besides the far-field coupling from far separated NPs,

near-field interactions between some nanodisks may occur on highly disordered samples. Nevertheless, the macroscopic effect from the blueshift and redshift effect around the dipolar resonance is balanced isotropically, thus results in no shift.

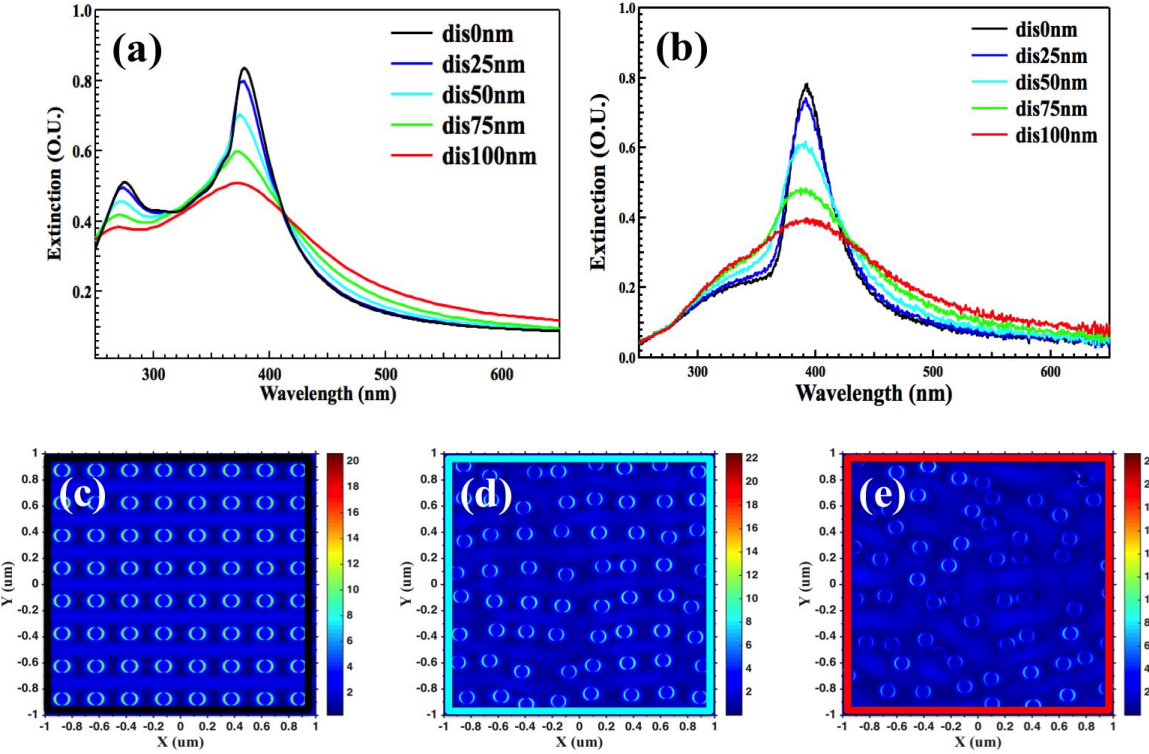


Figure 5.6 Calculated (a) and experimental (b) extinction spectra for nanodisks array (100 nm diameter, base pitch 250 nm) with different degrees of disorder. Electric field maps of three samples with different degrees of disorder under excitation at 378 nm are presented for dis0nm (c), dis50nm (d) and dis100nm (e).

The E-field distribution excited at 378 nm from FDTD calculation (with polarization excitation along x axis) is presented in Figure 5.6(c-e) for three samples with different degrees of disorder. As it is depicted in Figure 5.6c, the fully ordered array presents a highly symmetric E-field distribution. In Figure 5.6d and Figure 5.6e, where the periodicity of the pattern is broken by the introduction of displacement disorder, some dimers with random gaps are formed. This is particularly visible on the map in Figure 5.6e where tiny gaps are formed between nanodisks very close to each other. Consequently, the broadening of the extinction spectra can be also partially attributed to the contribution of dimers. Thanks to the large number of NPs involved in the FDTD simulation, the simulated results agree well with the spectra from experiments.

5.3.4. Investigation on the array with different pitch

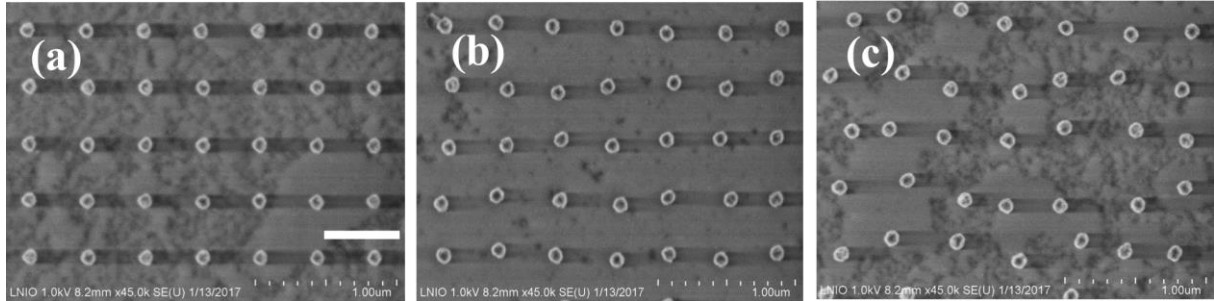


Figure 5.7. SEM images of nanodisk arrays (100 nm diameter, basic pitch 400 nm) with displacement disorder of (a) 0 nm, (b) 50 nm, and (c) 100 nm. Scale bar 500 nm.

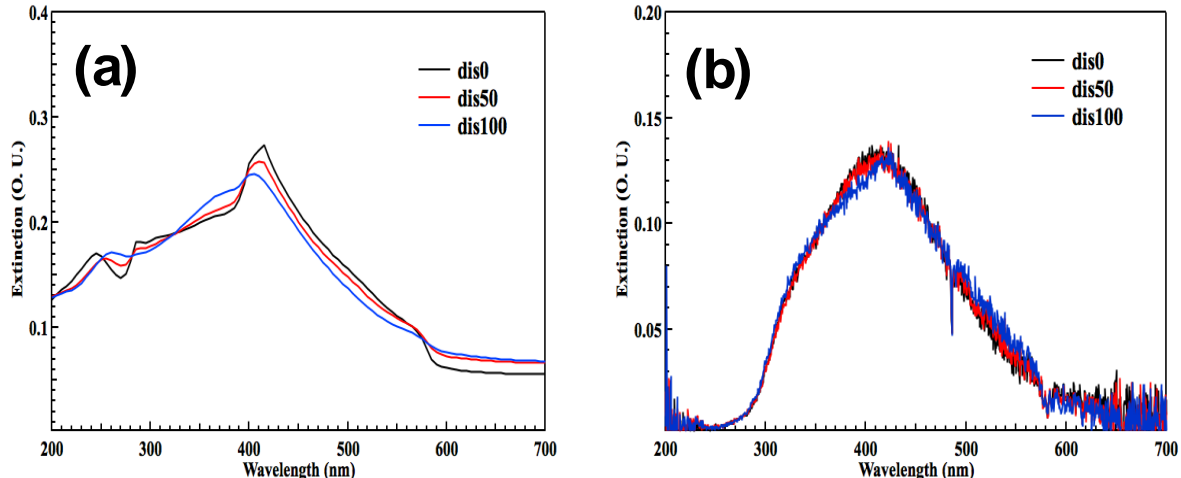


Figure 5.8. Calculated (a) and experimentally measured (b) extinction spectra for nanodisk arrays (100 nm diameter) with 400 nm pitch as a function of displacement disorder.

The array of nanodisks with a diameter of 100 nm and a pitch of 400 nm has also been studied both experimentally and theoretically for the comparison. A typical example of prepared samples can be found in Figure 5.7. Here, due to the large pitch of 400 nm, the extinction intensity is much lower than the array with a pitch of 250 nm. However, the observed tendency is consistent with our previous results although the effect of disorder is much less strong. Here, we should emphasize again that the average movement of NPs in the array is zero due to the uniform disorder. Thus, NPs are mixed more homogeneously with increasing displacement disorder at the same particle density. In conclusion, uniform displacement

disorder brings a broader and lower plasmonic resonance without shifting resulted from the unchanged average nanodisk density in the area and balanced interactions from different distances between aluminium plasmonic nanostructures.^{122,123}

5.4. Size disorder

5.4.1. Influence on optical properties

Unavoidably, the nanofabrication procedure will always introduce an undesired distribution of particle sizes. By designing a uniformly size-disordered array, we studied the influence of size configuration to the macroscopic extinction spectra. The fabricated samples and extinction spectra both from simulations and experiments are presented in [Figure 5.9](#). As we already discussed in the previous chapter, the peak around 276 nm is ascribed to the coupling between lattice mode and the mode due to the appearance of substrate which does not shift much with the size of Al nanodisk. Therefore, even if varying the sizes of NPs in an array while remaining the periodicity, the uniform size disorder does not influence much on the peak at 276 nm, as shown in [Figure 5.9\(b\)](#).

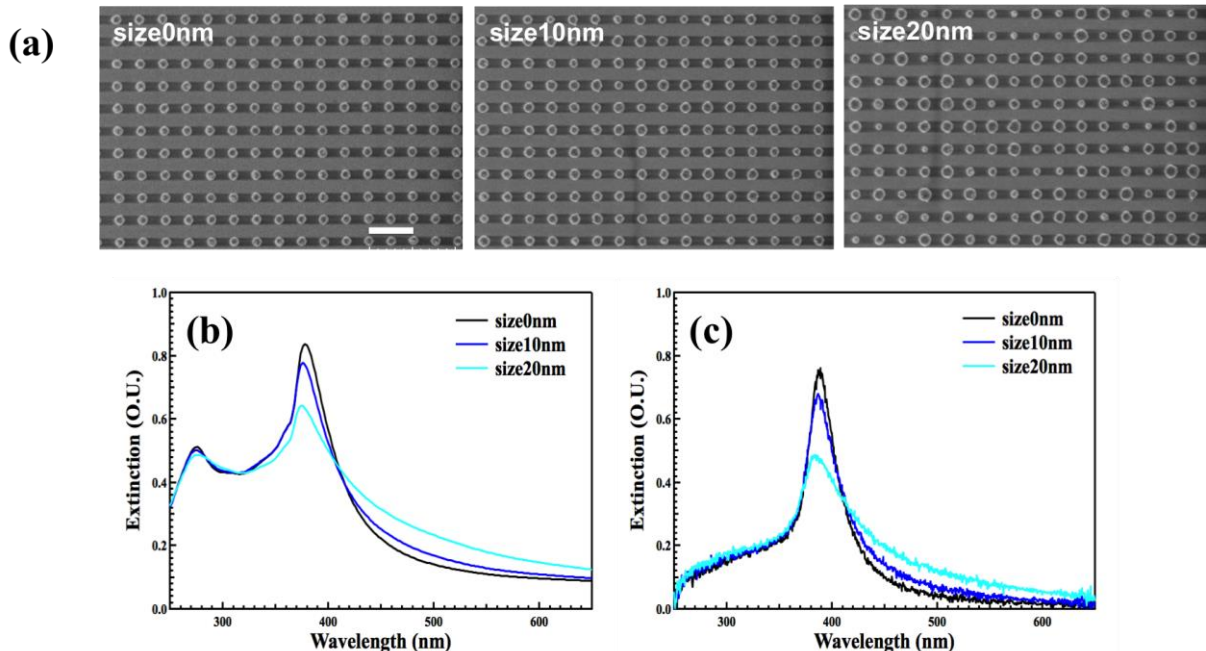


Figure 5.9 (a) SEM images of fabricated uniformly size-disordered arrays with pitch 250 nm. Scale bar 500 nm. Calculated (b) and experimental (c) extinction spectra for nanodisk array with different size disorder.

Chapter 5

As for the mode around 378 nm, it is attributed to the dipolar resonance and more influenced by the size of NP. Without changing the periodicity in the array, it still preserves the lattice effect. Therefore, as depicted in [Figure 5.9\(b\)](#) and [\(c\)](#), the size disorder brings a broadening of the plasmonic dipolar resonances much less pronounced than the displacement disorder observed previously. In the size-disorder array, the plasmonic resonances at shorter wavelength sustained by smaller NPs and the resonances at longer wavelength sustained by larger NPs superimpose together. Because of the uniform randomness introduced in the radius value, both redshifted and blueshifted resonances are equally distributed around the original peak. Therefore, a decrease in intensity and a broadening of the dipolar resonance are observed both from the simulation and experiment. Meanwhile, the central wavelength of the plasmonic peaks does not vary significantly. The E-field distribution is calculated at 378 nm as shown in [Figure 5.10](#). Due to the randomness of diameter, some Al nanoparticles are off-resonance as evidenced by their near-field electric field intensity diminution, thus confirming the above-mentioned assumption.

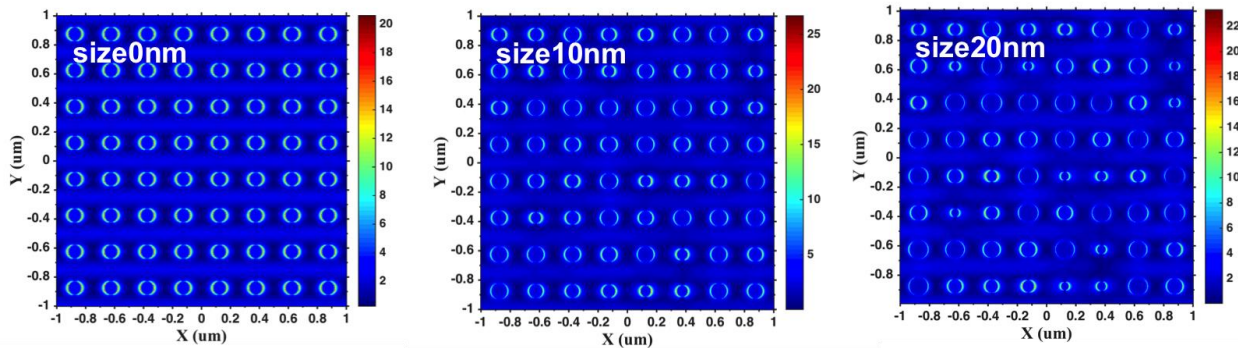


Figure 5.10. Calculated electric field for nanodisk array with different size variations at 378 nm. Polarization direction is along the x axis.

We conclude here that the uniformly disordered size distribution generates a broadened and reduced dipolar resonance without significantly shifting its wavelength. In this case, this effect is attributed to both the conservation of lattice effect and the overlapping of different resonances at different wavelengths.

5.4.2. Investigation on the array with different pitch

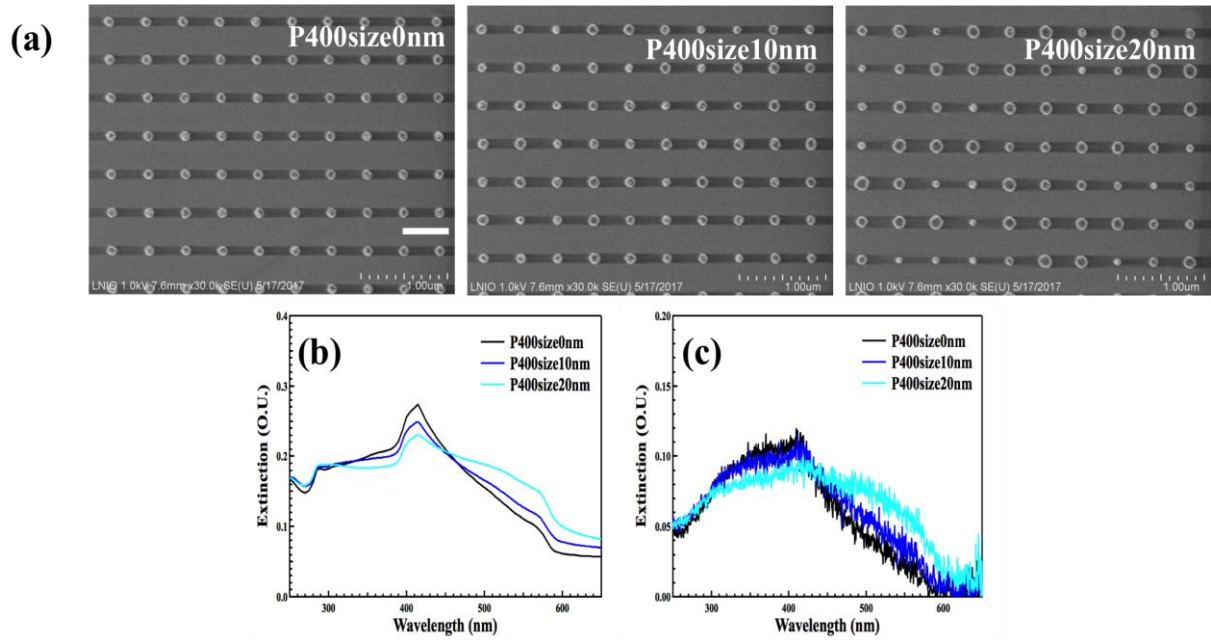


Figure 5.11. (a) SEM images of fabricated size-disordered arrays with pitch 400 nm (base diameter 100 nm). Scale bar 500 nm. Calculated (b) and experimental (c) extinction spectra for nanodisk arrays as a function of size disorder.

The uniform size disorder in the array with different pitch (400 nm) is also studied. The fabricated samples and extinction spectra from simulations and experiments are displayed in Figure 5.11. As it is already pointed out previously, the extinction peak intensity is much weaker due to the large pitch. However, the same tendency measured when introducing the size variation is observed. Moreover, the simulated spectra (Figure 5.11a) and experimental spectra (Figure 5.11b) show an excellent agreement.

5.5. Rotation disorder

A very interesting property of aluminium plasmonics is the possibility that both visible and ultraviolet resonances coexist on the same aluminium nanostructure. For instance, a well-designed aluminium nanorod is able to sustain a visible plasmonic resonance along its long axis while sustaining a near UV plasmonic resonance along its short axis. Changing the polarization of the illumination light is able to selectively excite these resonances.

5.5.1. Extinction spectra

Chapter 5

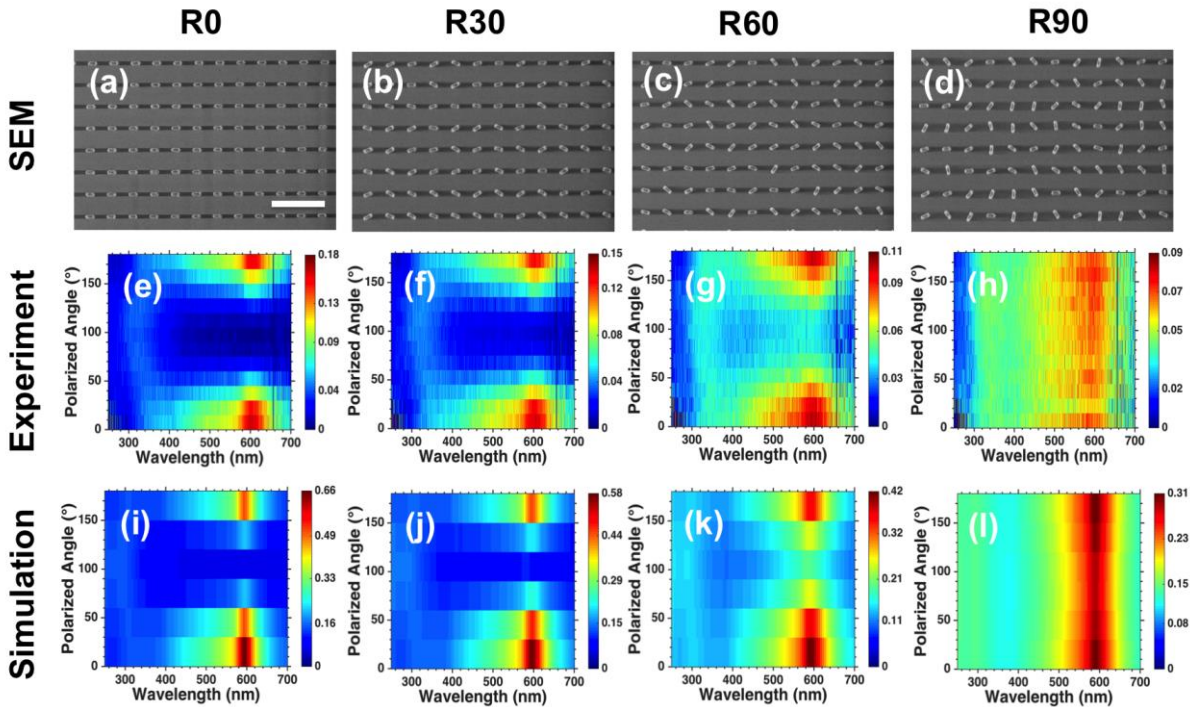


Figure 5.12. The top row (a-d) shows SEM images of aluminium nanorod arrays (short axis 50 nm, long axis 140 nm) in which nanorods have been progressively randomly rotated. Scale bar 1 μ m. Extinction spectra by normal incidence both from experiments (second row (e-h)) and FDTD calculations (third row (i-l)) of corresponding arrays with different polarization angles of incident illumination.

This possibility is illustrated in Figure 5.12 showing a SEM image of Al nanorod array (Figure 5.12(a)) and its corresponding polarization dependent extinction spectra both from experiments (Figure 5.12(e)) and calculation by FDTD (Figure 5.12(i)). Depending on the polarization illumination, the dipolar plasmonic mode along the short (centered at 300 nm in experiment) or the long axis (centered at 600 nm in experiment) can be selectively excited, as demonstrated experimentally and numerically. This result is interesting in itself and potential applications are numerous. For such nanostructures sensitive to the polarization, there is the possibility to introduce a random rotation angle. Here, a disorder is introduced by giving each nanorod in the periodic array a random angle of rotation. SEM images in the top row in Figure 5.12 (a-d) depict arrays with maximal rotating angle $\theta = 0, 30^\circ, 60^\circ$ and 90° respectively. Their corresponding polarization dependent extinction spectra both from experiments and FDTD calculations are presented on the two rows below, in Figure 5.12 (e-h) and Figure 5.12 (i-j), respectively.

When increasing rotation disorder, the spectra become less and less dependent of the polarization of incident light. For instance, for a polarization angle of 0° (along the long axis), the number of nanorods efficiently excited decreases with randomness, weakening the intensity of extinction peak at 600 nm in experiment. The same goes for the polarization angle of 90° (along the short axis), where the intensity of the resonance at 300 nm is weakened by the decreased number of nanorods efficiently excited along their short axis. For the highest rotation disorder (Figure 5.12 d, h, l), extinction spectra become insensitive to the polarization due to the equivalent amount of nanorods rotated at different angles in the array. This results in a broadband extinction spectrum from 300 to 700 nm for any polarization of the incident light. Both simulation and experiment confirm the same phenomenon.

5.5.2. Electric field distribution

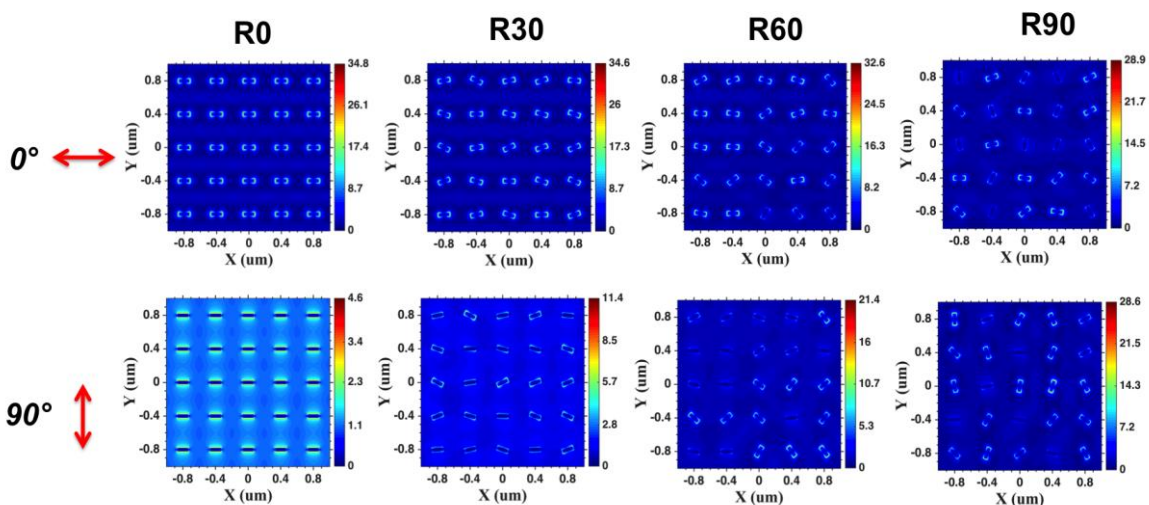


Figure 5.13. Calculated E-field maps of aluminium nanorod arrays with increasing degrees of rotation disorder for two different polarization states of the incident light at 590 nm.

As mapped in Figure 5.13, the electric field distributions in arrays with rotation disorder have been numerically calculated at 590 nm for 0° and 90° polarization, respectively. Without any rotation disorder, the electric field is equally distributed on each nanorod. It is located at the two extremities with the same intensity, along the short or the long axis, depending on the incident polarization. When a random rotation is applied to each nanorod, the electric field becomes differently distributed on each nanorod. As expected, the more the nanorod is

Chapter 5

perpendicular to the polarization of incident light, the less its near field is intense. The highest rotation disorder ensures that the array will match any polarization and wavelength of incident light at equal number of nanorods. This results in the insensitivity of nanorod array to the incident polarization and its broadband extinction spectrum from the near ultraviolet and visible region, as shown in [Figure 5.12](#).

5.6. Conclusions

To summarize, we studied numerically and experimentally the plasmonic properties of aluminium nanostructure arrays in which uniform disorder is introduced. Firstly, uniform displacement disorder in the nanodisk arrays reveals that the main signature of extinction spectrum is governed by the averaged number density distribution of nanoparticles. Meanwhile, decreased intensity and broadened resonance are brought due to the varying interaction from nanodisks at different separation. Secondly, the effect of another uniform disorder arising from variations on the particle size in the nanodisk array is also studied, and similar influence is obtained despite that the phenomenon is actually contributed by different resonances from nanoparticles in different sizes. Lastly, arrays of polarization-sensitive aluminium nanorods sustaining plasmonic resonances both in the near ultraviolet and the visible range are studied. By introducing a random rotating angle for each nanorod in the array, the polarization sensitivity is lowered and depends on the value of the maximum rotation allowed for nanorods. This results in a polarization insensitivity of the nanorod array with broad extinction spectrum from 300 to 700 nm. Considering the results, potential applications of uniformly disordered nanostructures reside in the nanophotonic systems requiring a broadband plasmonic resonance and insensitivity of polarization. For example, large-scale disordered nanostructures for the light harvesting could be developed by other robust and inexpensive fabrication methods like colloidal lithography with optimized parameters.

Chapter 6 Summary and outlook

Over the last decades, plasmonics has been almost exclusively studied by using gold or silver nanostructures, exhibiting plasmonic properties from the infrared to the visible spectral region. Due to inherent limitations related to their electronic structures, these metals do not sustain plasmonic resonances in the ultraviolet. Nevertheless, emerging applications will require the extension of plasmonics toward higher energies, particularly in the UV-range. For instance, plasmonic materials coupled with wide bandgap semiconductors, such as ZnO or GaN, could lead to more efficient light emission or harvesting devices. Aluminium has been therefore proposed as an alternative plasmonic material, as its electronic properties allow for sustaining plasmon resonances in the ultraviolet while keeping low losses. Aluminium is now widely regarded as one of the most promising metal for pushing the spectral limits of plasmonics towards high energies, up to 6 eV. Additionally, Al is cheap, abundant, non-toxic, and compatible with the complementary metal-oxide-semiconductor technology. Numerous other applications of Al plasmonics include nonlinear optics, enhanced fluorescence, UV-SERS, optoelectronics, plasmonic-assisted lasing, photocatalysis, and structural colors. Nevertheless, aluminium nanostructures with perfectly controlled geometry and good structural and surface quality are still difficult to produce in conventional electron beam lithography, especially with this metal, which tends to form large grains when evaporated. Therefore, the plasmonic properties (more precisely the localized surface plasmon resonances or LSPRs) of Al nanostructures suffer from broadening and are not scalable precisely if their parameters such as crystallinity, surface roughness or geometry are not well controlled. Moreover, even if a self-limited oxide layer protects Al nanoparticles due to passivation, their stability when exposed to various thermal processes such as varying temperature is an issue hindering their systematic use in industry.

In this thesis, we investigate how these various key parameters affect the optical properties of Al nanostructures. Numerical and experimental studies have therefore been performed on the plasmonic properties of Al nanostructures taking into account their oxidation, temperature, surface roughness, and uniformity. Firstly, in [Chapter 2](#) we study the natural stability of Al nanoparticles exposed to air and water environment. Al plasmonic resonances show about 90-days stability when Al nanoparticles are exposed to the ambient air. Secondly, in [Chapter 3](#)

Chapter 6

we study the influence of rapid thermal annealing on the plasmonic properties of Al nanostructures. An improvement of the plasmonic resonances resulting in a reduction of their full width at half maximum is found after the annealing at 400 °C for 5 minutes of Al nanostructures in ambient air. This effect is attributed to the decreased number of grain boundaries inside the Al nanoparticles as proved by TEM measurements. Thirdly, in [Chapter 4](#) we unveil the effect of surface roughness on the plasmonic properties sustained by Al nanostructures. The top surface roughness of Al nanodisk is found to cause the disappearance of the substrate-induced quadrupolar mode. At the same time, the roughness induces a weakening of the plasmonic dipolar mode. Finally, in [Chapter 5](#) we investigate numerically and experimentally the effect of uniform disorder introduced in aluminium nanoparticle arrays. By varying the displacement, size or rotation of each nanoparticle in the periodic arrays, influences of uniform disorder on the plasmonic resonances are studied in the near ultraviolet and visible region. Interesting properties of such arrays are revealed. For instance, aluminium nanorod arrays with rotation disorder are shown to provide polarization-independent plasmonic resonances both in the near ultraviolet and visible range. Such arrays may have applications in solar cells, which require a broadband absorption in the near ultraviolet and the visible range. Based on the obtained results in this thesis and previous research, there are lots of interesting topics for Al plasmonic to develop further.

1. During the fabricating procedure and the period of storage and usage, the stability of Al nanoparticle has a crucial role and need to be taken into account. For the commercial large-scale production in the future, further investigation should be done. And additional treatment could be studied and employed to prolong and stabilize the Al plasmonic properties.
2. By manipulating the location of hot spots on Al nanoparticles, we could enhance the SERS performance of Al in the visible range. Possible methods include introducing a buffer layer on the substrate to create a more symmetric environment, modifying the top surface topography, and designing a suitable shape of nanoparticle.
3. To fully use the wide spectral range of Al plasmonic, a color mixing method based on the research of uniform disorder is proposed. Firstly, we carefully choose three periodic nanodisk arrays for the RGB pixels: diameter 240 nm with pitch 468 nm for red pixel, diameter 150 nm

with pitch 364 nm for green pixel, and diameter 120 nm with pitch 290 nm for blue pixel. Here, the lattice mode is used to generate the red color at 700 nm, green color at 546.1 nm, and blue color at 435.8 nm according to the CIE standard. Then, by giving each nanodisk in the pixel a uniform displacement disorder, as we have already done previously, we can obtain a pixel with decreased scattering intensity. Finally, by combining the RGB pixels with different scattering intensities we could receive a mixing pixel in different color. To test the idea, a large pixel is chosen for better vision in three proposed color-mixing structures. The preliminary result is shown in [Figure 6.1](#).

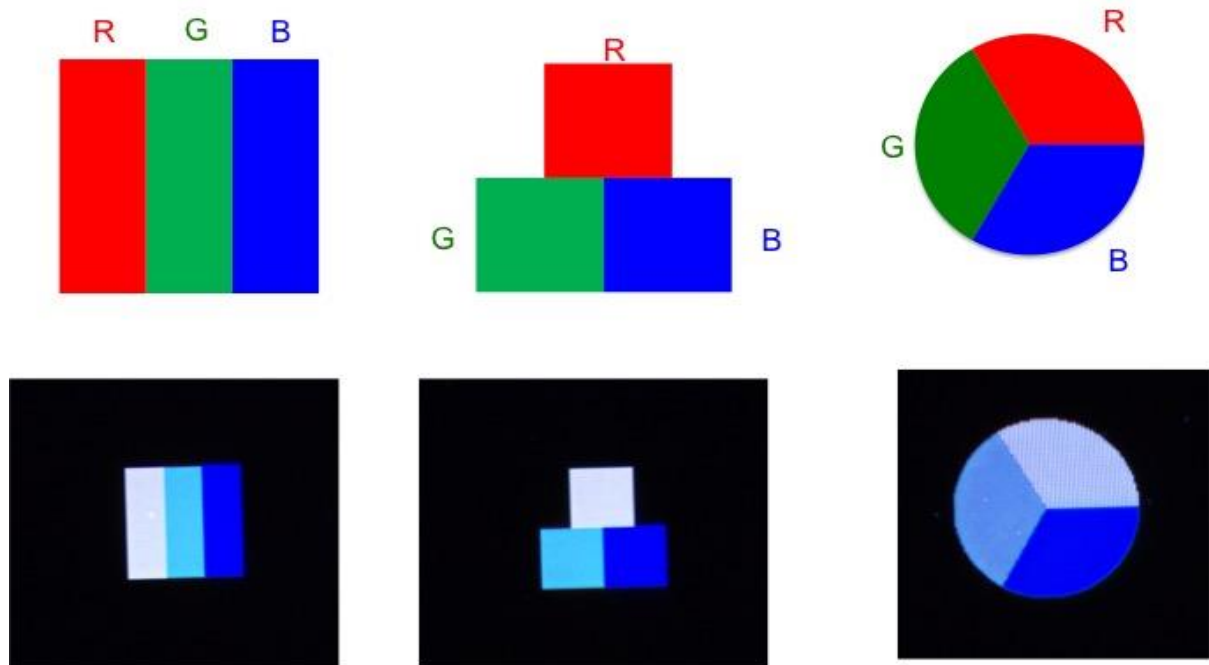


Figure 6.1. Three proposed color-mixing strategies. The upper images depict the schematic and the lower images show experimental darkfield images from periodic arrays. The strip pixel is $13.3 \times 40 \mu\text{m}^2$, the square pixel is $20 \times 20 \mu\text{m}^2$, and the radius of the circular mixing pixel is 20 μm .

The best result is easily obtained for the blue pixel, which is not surprising because of the excellent performance of Al plasmonic near UV. However, the designed green pixel appears as cyan color, and designed red pixel appears as white color. The mismatch is caused by the strong scattering at shorter wavelength in the spectrum of big Al nanodisk. An example can be checked in [Figure 2.6](#), where the spectrum of nanodisk in 160 nm diameter shows a particularly broad spectra from 200 to 700 nm. Therefore, to improve the purity of green and red pixel, one approach could be adopted. In the experimental results shown in [Figure 6.1](#), we set the height of nanodisk to 50 nm. When the height of nanoparticle is large, high modes

Chapter 6

trend to appear. Therefore, reducing the height of nanodisk will decrease the scattering at shorter wavelength and possibly improve the purity of color. Otherwise, we can fully exploit the usage of Al plasmonic as a white pixel or a broadband scatter.

Although we are not involved in this thesis, the potential applications of Al plasmonic such as metamaterial and structural color are tremendous. Meanwhile, Al plasmonics is still in its infancy now and there are massive fields waiting to be explored. In all, aluminium is a highly promising material for commercial applications in the field of nano optics from the infrared to UV range.

Methods

a. Electron beam lithography process

Electron beam lithography (EBL) is a fundamental technique of nanofabrication, which provide a precise and flexible control down to sub-10 nm scale. The EBL process for nanofabrication in our lab is described as follows. Firstly, the quartz substrates (AGAR reference L4465, thickness 250 μm) were rinsed by ultrasonic in diluted Decon 90 solution (5% + 95% distilled water) for 10 minutes and subsequently cleaned in distilled water for 10 minutes. The substrates were then degreased in the acetone and isopropanol (IPA) solution mixture (acetone:IPA = 1:1) for 10 minutes, and the final cleaning was done in IPA solution for 10 minutes. All the ultrasonic bathes were done at 40 °C. Finally, the quartz substrates were blown dry with Ar gas for the next procedures, as shown in [Figure M1](#).

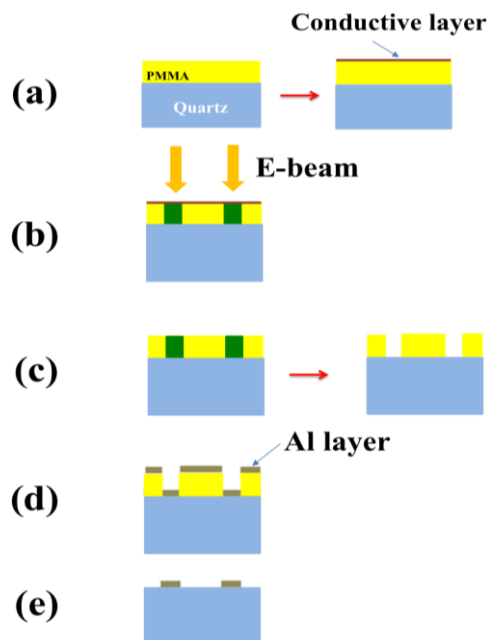


Figure M1. Standard EBL process.

(a) A PMMA (poly(methyl methacrylate)) layer (about 160 nm) was deposited on the quartz substrate by spin-coating, followed by baking at 180 °C on the hot plate for 10 mins. A conductive polymer (Spacer 300Z) layer (about 10 nm) was then spin-coated on the top of PMMA layer, followed by baking at 60 °C for 10 mins.

Experimental methods

- (b) The PMMA layer was exposed with the electron beam using Eline Raith to generate designed patterns (about $40 \times 40 \mu\text{m}^2$) with typical doses of $200 \mu\text{C}/\text{cm}^2$.
- (c) After removing the conductive layer in water, development was done for 1 min in a methyl isobutyl ketone/isopropanol solution (MIBK/IPA=1:3).
- (d) An aluminium layer (around 50 nm) was deposited at 0.2 \AA/s rate by electron beam evaporation (Plassys MEB 400) controlled by the calibrated quartz crystal microbalance in the 5×10^{-6} mbar vacuum.
- (e) The lift-off process was done in the acetone solution for more than 4 hours.

b. Rapid thermal annealing treatment

All rapid thermal annealing (RTA) processes were done in a JetFirst100/150 lamp-heated RTA furnace for 5 min in an ambient atmosphere (i.e., the external atmosphere was simply let into the furnace). The heating procedure set in the system follows as: one minute for raising the temperature of the chamber from 20°C to the designed annealing temperature, after maintaining at the annealing temperature for five minutes, then cooling the system to 20°C in one minute.

c. SEM and TEM measurement

Both SEM and TEM images have been acquired using an instrument FEG Hitachi SU8030. Because of the strong charge effect of alumina and quartz, the SEM images were normally obtained under 1 kV. For TEM measurements, Al nanoparticles have been lithographed on TEM-compatible substrates. The latter consists of 20 nm thick Si_3N_4 square membranes engraved in silicon circular wafers (NEYCO reference 4159SN-BA). TEM images were acquired operating at 30 kV.

d. Atomic force microscopy measurements

Atomic force microscopy (AFM) measurements were performed on an Agilent 5100 system in tapping mode. Commercial tips (*Nanosensor*, type PPP-NCLR-50) were used. Achieved results were analysed with the Gwyddion software.

e. Extinction spectra measurement

Extinction spectra are characterized using a homemade setup. The schematic of the setup is shown in [Figure M2](#). Light from an unpolarized UV-visible lamp (Oriel, Series Q Deuterium Light Sources) is collimated by lens and focused onto the sample with a spot about $20 \times 20 \mu\text{m}^2$. A removable polarizer can be used to generate polarized source for polarization tests. With a collecting lens, a 240 μm diameter optical fiber connected to the UV-VIS spectrometer (HR4000, Ocean Optics) was used to get the transmission signal with integral time of 1 second. Reference spectrum was taken in the area on the quartz substrates without nanostructures.

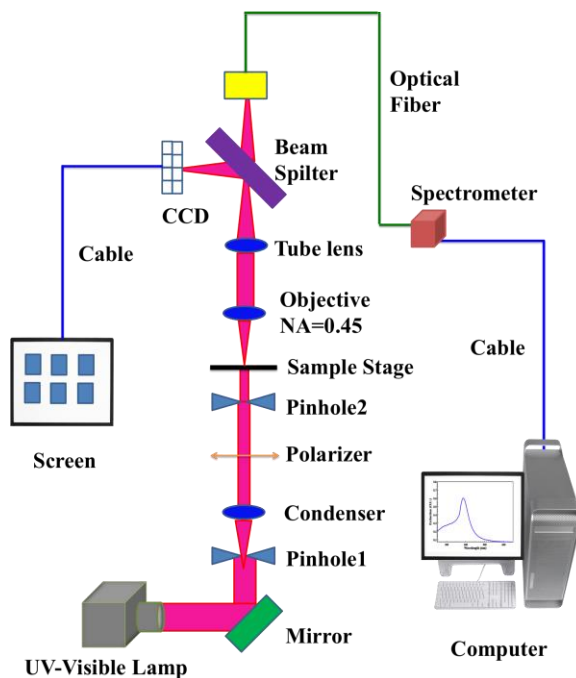


Figure M2. Schematic setup for extinction spectra measurement

f. FDTD simulation

Experimental methods

The commercial *Lumerical FDTD solution* software was used for the Finite-difference time-domain (FDTD) simulation. To simulate the periodic array, periodic boundary conditions in the x and y directions, and perfectly matched layer (PML) in the z directions were used. For each Al NP, 4 nm Al_2O_3 layer is assumed as the natural oxide layer. A finer mesh is used in the region of NP. The dielectric functions for the materials during the calculation were all from the database of Lumerical software database (Palik data for Al and Al_2O_3). Normal incident plane wave (200-700 nm) placed in the quartz substrate was chosen as the excitation source. The transmission spectra (Q_{tra}) were obtained directly by the field monitor over the NP, then extinction spectra (Q_{ext}) were calculated by $Q_{\text{ext}}=1-Q_{\text{tra}}$. A unit cell normally used for the periodic array is exemplified in [Figure M3](#).

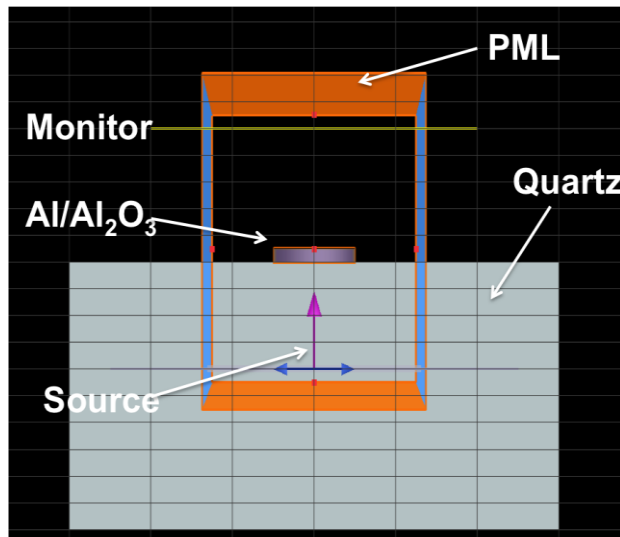


Figure M3. Schematic view of the periodic unit cell in simulation

Résumé

1. Introduction

Les électrons de conduction des nanoparticules métalliques (NPs) peuvent osciller de manière cohérente en réponse à la lumière incidente. Ces oscillations sont ce qu'on appelle les résonances plasmoniques de surface localisées (LSPR). Lorsque la longueur d'onde de la lumière incidente correspond à celle de la résonance plasmonique, le LSPR se traduit par une forte exaltation et d'un fort confinement du champ local autour de la NP. Ce phénomène permet de confiner et de manipuler les ondes électromagnétiques à l'échelle nanométrique, c'est la plasmonique. La longueur d'onde de résonance dépend du métal constituant la NP, de sa taille, de sa forme et de son milieu environnant. La plasmonique a mené à de nombreux domaines de recherche aboutissant sur des applications variées, telle que la détection d'indice de réfraction, le photovoltaïque, la spectroscopie Raman exaltée en surface (SERS) ou encore la fluorescence exaltée et le biomédical (tests de grossesse, pour donner un exemple concret).

Jusqu'à présent, pratiquement seules les NPs de métaux nobles d'or (Au) et d'argent (Ag) ont été étudiées, en raison de leurs excellentes performances plasmoniques dans les régions visible et infrarouge. Néanmoins, les futures applications nécessiteront l'extension des résonances plasmoniques vers des longueurs d'onde plus courtes, en particulier dans la gamme des ultraviolets (UV). Or l'or ne peut pas supporter de résonances plasmoniques à des longueurs d'onde inférieures à 520 nm en raison des transitions interbandes. Les nanostructures d'argent présentent des résonances plasmoniques jusque dans l'UV très proche (350 nm), mais souffrent d'une forte oxydation. L'aluminium possède quand à lui une constante diélectrique dont la partie réelle est négative aux longueurs d'onde UV (jusqu'à 80 nm) tout en gardant une partie imaginaire relativement faible, donc des pertes liées à l'absorption faibles également. Toutefois ce dernier présente une forte absorption dans une bande spectrale relativement étroite, autour de 800 nm, due à sa structure de bande particulière. L'aluminium est aujourd'hui considéré comme l'un des métaux les plus attrayants pour pousser la nanoplasmonique jusqu'aux énergies UV. Un autre intérêt majeur de l'aluminium en tant que matériau plasmonique réside dans sa nature "large bande": à part une petite région autour de λ

Résumé

= 800 nm (correspondant à la transition interbande proche de 1.4 ev), l'aluminium présente des résonances plasmoniques de l'infrarouge aux UV profonds. En outre, l'aluminium est bon marché et abondant, car il est le troisième élément le plus abondant sur la terre. Parallèlement, l'aluminium est industriellement recyclable et sa non-toxicité lui confère un bon potentiel dans les bio-applications. Dernier point mais non le moindre, sa compatibilité avec la technologie CMOS (métal-oxyde-semi-conducteur) est également un facteur clé, qui ouvre la voie à la production industrielle massive de composants à base d'aluminium nanostructuré. Certes, l'aluminium subit également de l'oxydation comme l'Ag, mais par contre il ne s'oxyde pas en profondeur car il forme naturellement une couche d'oxyde auto-protectrice de quelques nanomètres d'épaisseur, ce qui le rend chimiquement plus stable dans le temps.

Néanmoins, les nanostructures en aluminium à géométrie parfaitement contrôlée et avec de bonnes qualité structurelle (cristallinité) et de surface (rugosité la plus faible possible) sont encore difficiles à réaliser en lithographie électronique classique, notamment car ce métal tend à former de gros grains lorsqu'il est évaporé. Par conséquent, les résonances plasmoniques supportées par les nanostructures Al souffrent d'élargissement spectral et ne sont pas réglables finement si ces paramètres tels que la cristallinité, la rugosité de surface ou la géométrie ne sont pas bien contrôlés. De plus, même si une couche d'oxyde autolimitée protège les nanoparticules d'Al en raison de sa passivation chimique, leur stabilité lorsqu'elles sont exposées à divers processus thermiques tels qu'une température élevée est un problème qui entrave leur utilisation systématique dans l'industrie.

Dans cette thèse, nous étudions comment ces différents paramètres clés affectent les propriétés optiques des nanostructures d'Al. Des études numériques et expérimentales ont donc été réalisées sur les propriétés plasmoniques des nanostructures Al en tenant compte de leur oxydation, de leur rugosité de surface, de l'élévation de la température environnante ou encore de leur uniformité. Dans un premier temps, nous étudions la stabilité naturelle des nanoparticules d'aluminium exposées à l'air et à l'eau. Les propriétés plasmoniques des nanostructures d'Al faites par lithographie électronique montrent ainsi une stabilité d'environ 90 jours lorsqu'elles sont exposées à l'air ambiant. Deuxièmement, nous étudions l'influence du recuit thermique rapide sur les propriétés plasmoniques des nanostructures d'Al. Une amélioration des résonances plasmoniques se traduisant par à une réduction de leur largeur à

mi-hauteur est constatée après un recuit à 400 °C pendant 5 minutes des nanostructures. Cet effet est attribué à la diminution du nombre de joints de grains à l'intérieur des nanoparticules d'aluminium, comme le prouvent les mesures TEM. Troisièmement, nous dévoilons l'effet de la rugosité de surface sur les propriétés plasmoniques des nanostructures d'Al. Ainsi la rugosité de surface des nanodisques en Al provoque la disparition du mode quadrupolaire induit par le substrat, mode supporté par les nanodisques déposés sur substrat. En même temps, la rugosité induit un affaiblissement du mode dipolaire plasmonique supporté également dans les nanodisques. Enfin, nous étudions numériquement et expérimentalement l'effet du désordre uniforme introduit dans des réseaux de nanoparticules d'aluminium. En faisant varier le déplacement, le rapport d'aspect ou la rotation de chaque nanoparticule dans les réseaux périodiques, l'influence du désordre uniforme sur les résonances plasmoniques est étudiée dans la région du proche ultraviolet et du visible. Les propriétés plasmoniques UV-Vis de tels réseaux désordonnés sont révélées. Par exemple, il est montré que les réseaux de nano-bâtonnets d'aluminium présentent des résonances plasmoniques dépendantes de (et contrôlable) la polarisation de la lumière incidente à la fois dans le domaine du proche ultraviolet et du visible. De tels réseaux peuvent avoir des applications dans les cellules solaires, qui nécessitent une absorption à la fois dans le proche ultraviolet et dans toute la plage visible.

2. Stabilité des nanoparticules d'aluminium

Le processus d'oxydation est un phénomène très important à prendre en compte dans l'étude de la plasmonique à base d'aluminium. En raison de leur rapport surface sur volume élevé, la stabilité naturelle des NP d'Al est différente de celle de film d'Al. Dans cette partie, une étude sur les propriétés plasmoniques de réseaux de nanodisques d'Al a été réalisée sur une longue période de temps.

2.1 Modèle pour simuler l'oxydation des nanostructures en aluminium

Un modèle d'oxydation simplifié est adopté, est schématisé sur la [Figure R1](#). En supposant que la forme géométrique ne change pas pendant l'oxydation, une couche uniforme d'oxyde en alumine ou d' Al_2O_3 d'épaisseur L croissante et d'indice de réfraction $n=1,5$ est ajoutée en

Résumé

remplaçant progressivement le noyau d'Al. Pour une certaine masse d'Al, un effet d'extension de volume lors de l'oxydation se produit (V_{Al} : $V_{Al_2O_3} \approx 80\%$). En considérant cet effet et en supposant qu'une couche d'oxyde uniforme est formée de manière isotrope et sans déformation (la hauteur et le rayon ont le même incrément lors de l'oxydation), une couche d' Al_2O_3 plus épaisse est introduite dans le modèle. Au stade initial de l'oxydation, pour le nanodisque de diamètre 100 nm et de hauteur 50 nm, (rayon de noyau métallique diminué de 10 nm), la différence d'épaisseur de couche d'oxyde entre les deux modèles (c'est à dire en prenant ou non en compte l'expansion de volume due à l'oxydation) est calculée et vaut environ 1,5 nm. Même si le noyau métallique est complètement oxydé, les calculs montrent que la différence n'est que d'environ 4 nm. De plus, pour prendre en compte l'expansion de volume, un maillage beaucoup plus fin sera exigé dans la simulation FDTD avec une exigence croissante de calcul de la mémoire et du temps. Enfin, les spectres d'extinction simulés du modèle simplifié (sans augmentation de volume du à l'oxydation) son en bon accord avec les résultats expérimentaux. Donc, à partir de maintenant, le modèle sera utilisé pour simuler l'oxydation de nanostructures d'Al.

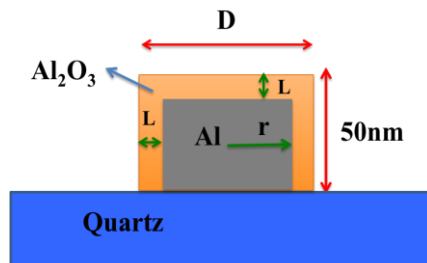


Figure R1. Schéma du modèle pour simuler par FDTD l'oxydation des NPs d'Al de diamètre D , d'épaisseur de 50 nm, de rayon de noyau métallique r et d'épaisseur de couche d'oxyde L .

2.2 Résultats de la simulation

D'après les résultats présentés sur la [Figure R2a](#), on s'aperçoit que les nanodisques avec les plus petits diamètres perdent plus rapidement leur propriétés plasmoniques, même avec une couche d'oxyde relativement mince (D50), alors que les nanodisques de plus grands diamètres conservent leurs propriétés plasmoniques avec une couche d'oxyde de plus de 30 nm d'épaisseur (D160). Sur la [Figure R2 \(b\) et \(c\)](#), on aperçoit que les résonances des réseaux de nanodisques (D50, D70 et D100) subissent dans un premier temps un décalage vers le rouge

avec l'augmentation de la couche d'oxyde, puis dans un deuxième temps un décalage vers le bleu en même temps qu'une décroissance de plus en plus marquée de leur intensité jusqu'à disparition de la résonance, lorsque la couche d'oxyde est maximale (disparition du cœur en métal).

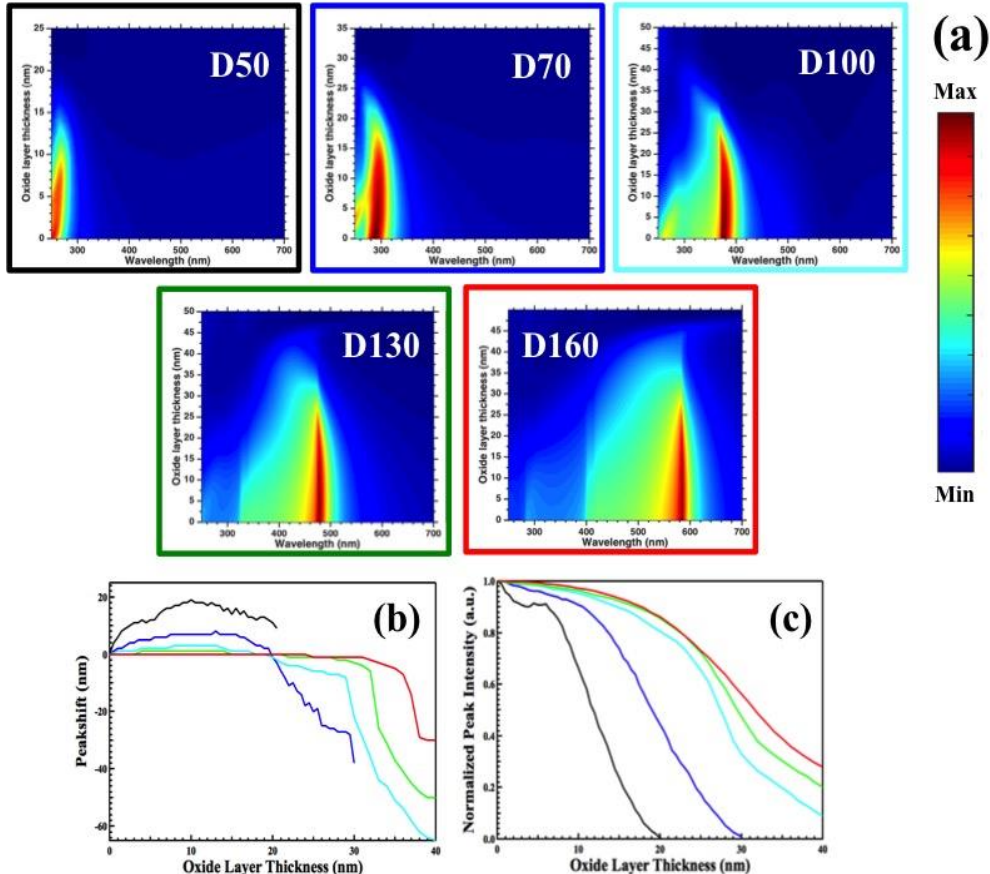


Figure R2. (a) Spectres d'extinction calculés sur des réseaux de nanodisques d'Al (diamètre $D = 50, 70, 100, 130, 160$ nm, hauteur 50 nm, pas 2.5D) avec une couche d'oxyde croissante. La barre d'échelle représente l'intensité d'extinction. Le décalage (b) et l'intensité (c) du pic de résonance (comparativement au spectre de chaque NP sans couche d'oxyde) sont tracés en fonction de l'épaisseur de la couche d'oxyde. La couleur de chaque boîte de (a) correspond à la couleur de la ligne indiquant la taille de NP dans (b) et (c).

De plus, le maximum de décalage vers le rouge (red shift) diminue avec l'augmentation de la taille du nanodisque. Durant l'oxydation, la diminution de la taille du noyau en Al entraîne certainement un décalage de la résonance vers le bleu (blue shift), tandis que l'augmentation de la couche d' Al_2O_3 entraîne un décalage vers le rouge. Ce sont ces deux effets combinés qui auront des poids différents selon la taille des nanostructures d'Al. Pour les nanodisques de petite taille, le red shift domine le processus jusqu'à une épaisseur pour la couche d'oxyde de

Résumé

15 nm environ (D50, D70 et D100). Le rétrécissement du noyau en Al prend le dessus au-delà de cette épaisseur entraînant ensuite un blue shift jusqu'à ce que la couche d' Al_2O_3 élimine complètement la résonance plasmonique. Dans le cas des grands nanodisques (D130 et D160), le red shift n'est pas visible mais seul le blue shift apparaît lorsque la couche d'oxyde devient conséquente. Ceci peut être attribué au fait que le noyau métallique reste grand devant l'épaisseur d'oxyde au début du processus d'oxydation. La résonance plasmon supportée par le gros noyau est dès lors peu influencée par la couche d'oxyde très fine devant la particule de grand diamètre. Seul une grosse oxidation donne ainsi un blue shift lorsque la partie métallique est bien diminuée.

Comme le montre la [Figure R2c](#), l'intensité de pic diminue de façon continue avec l'augmentation de l'épaisseur de la couche d' Al_2O_3 , indépendamment des diamètres. Cependant, les nanodisques plus petits montrent des décroissances beaucoup plus rapides que les grands nanodisques avec l'épaisseur de la couche d'oxyde. L'étude numérique montre que lors du processus d'oxydation, les variations des propriétés optiques des NPs d'Al n'ont pas les mêmes dynamiques, dépendamment de leurs tailles, donc du ratio oxyde/metal à l'intérieur.

2.3 Résultats expérimentaux sur la stabilité

Des réseaux de nanodisques ont été fabriqués par lithographie par faisceau d'électrons (EBL, Electron Beam Lithography). Après fabrication, les échantillons ont été exposés à l'air ambiant en salle blanche ($T = 21^\circ\text{C}$, humidité relative de l'ordre de 40 %) et les spectres d'extinction ont été mesurés quotidiennement sur une longue période. Ces résultats sont présentés sur la [Figure R3](#), pour plusieurs diamètres. Une légère augmentation de l'intensité d'extinction est observée sur la [Figure R3c](#), qui pourrait être attribuée à l'auto-recuit de nanodisques Al. L'auto-recuit est un phénomène commun largement observé dans différents matériaux avec différentes méthodes de fabrication (les références à ce sujet sont données dans le manuscrit de thèse). Les échantillons issus du procédé EBL pourraient présenter plus de défauts, tandis que l'évaporation thermique pourrait induire une forte déformation à l'intérieur des NP sous forme de joints de grains dans une structure très polycristalline, ce qui se traduirait par un état d'enthalpie plus élevé. Par conséquent, ces défauts, peuvent induire dans les NP à libérer de l'énergie en diminuant la taille des grains de façon naturelle,

conduisant à un lent recuit à température ambiante sur une longue période de temps. Globalement, les résultats révèlent une compétition entre auto-recuit et oxydation.

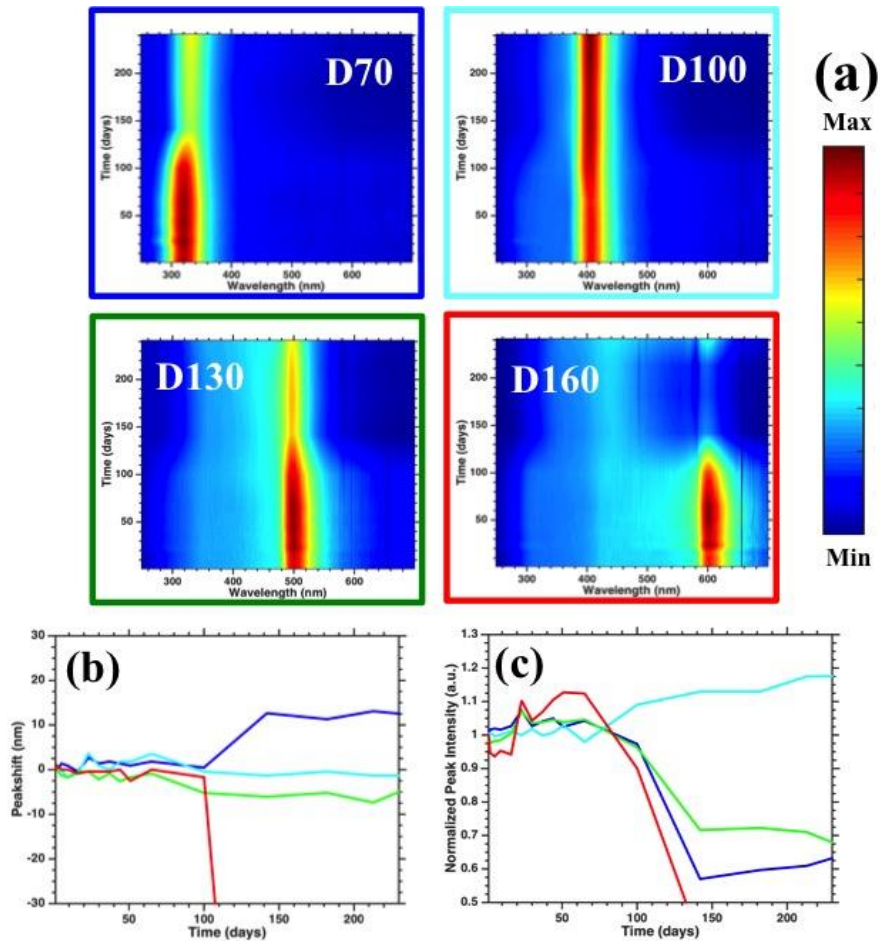


Figure R3. (a) Spectres d'extinction expérimentaux des réseaux de nanodisques en Al laissés à l'air libre (diamètre $D = 70, 100, 130, 160$ nm, hauteur 50 nm, pas $2.5D$) en fonction du temps (90 jours). La barre d'échelle représente l'intensité d'extinction. Le décalage spectral (b) et l'intensité maximale (c) sont normalisés avec le spectre du premier jour. La couleur de chaque boîte de (a) correspond à la couleur de ligne dans (b) et (c) indiquant la taille des NP. La fluctuation résulte de légères différences dans l'alignement au cours des mesures individuelles.

Après une stabilité de 90 jours, le petit nanodisque (D70) montrent clairement un spectre d'extinction décalé vers le rouge et une intensité diminuée due à l'oxydation. Les nanodisques plus petits avec des rapports de surface sur volume plus importants pourraient favoriser le taux d'oxydation, comme nous avons discuté dans l'étude numérique ci-avant. Pour les nanodisques plus gros (D130 et D160), la longueur d'onde maximale de la résonance prédictive est presque constante pendant l'oxydation sur 90 jours, sans baisse d'intensité notable. Ces dernières ont pendant ce temps des propriétés optiques stables, comme le montre la simulation

Résumé

de la [Figure R2b](#), et confirmé par les résultats expérimentaux présents sur la [Figure R3b](#). Cependant, les particules de gros diamètres D130 et D160 montrent une oxydation accrue après environ 90 jours, confirmée par des résonances qui se décalent vers le bleu avec des intensités continuellement diminuées. La diffusion du processus d'oxydation est susceptible de se produire le long des joints de grains et des défauts à l'intérieur des NPs. Par conséquent, plus de défauts étant présents à l'intérieur des nanodisques plus gros faciliteront l'oxydation. L'équilibre se produit pour le diamètre intermédiaire D100 qui conserve une résonance plasmonique étonnamment stable potentiellement due au phénomène d'auto recuit qui pourrait compenser une oxydation relativement faible.

3. Amélioration des propriétés plasmoniques de NP d'Aluminium par recuit rapide

Même si une couche d'oxyde native de 3 nm environ protège les nanostructures d'Al, leur stabilité, lorsqu'elles sont exposées à divers processus industriels est un point critique pour leur utilisation systématique dans les systèmes commerciaux. Par exemple, il est pertinent d'étudier l'effet de l'élévation de la température sur les propriétés optiques des nanoparticules d'aluminium, car elles peuvent connaître un fort échauffement local dans les futurs dispositifs ou lors des processus de fabrication utilisés dans l'industrie. Pour ces raisons, il est important d'étudier l'effet du recuit thermique sur les nanostructures en Al. Dans cette partie, des réseaux de nanodisques de diamètre 80, 100 et 120 nm et de hauteur 40 nm ont été fabriqués par EBL. Le pas entre les nanostructures est fixé à 250 nm. Un recuit thermique rapide (RTA pour Rapid Thermal Annealing) à l'air ambiant pendant 5 minutes a été effectué à différentes températures.

3.1 Spectres d'extinction

Comme représenté sur la [Figure R4](#) pour trois diamètres différents, une tendance claire est discernable: les résonances plasmoniques (mode dipolaire) subissent un décalage vers le bleu croissant accompagné d'une réduction de leur FWHM pour des températures de 300 et 400 °C. À 400 °C, la FWHM est réduite d'environ 1,5 pour chaque diamètre et le décalage bleu est

maximal, comme le montre la [Figure R4 d-f](#). Au-dessus de cette température, les résonances se comportent différemment. Avec un RTA à 500 °C, les résonances subissent alors ensuite un décalage vers le rouge plus ou moins marqué et une diminution de l'intensité; cet effet est plus prononcé pour les plus petits diamètres. Pour des températures égales ou supérieures à 600 °C, l'intensité des résonances diminue encore tandis qu'elles subissent un léger décalage vers le bleu. Cet effet est particulièrement prononcé pour les petits diamètres où les résonances dipolaires disparaissent presque, entraînant un pic faible et asymétrique. Pour les diamètres plus grands (≥ 100 nm), la signature optique reste homogène pour les RTA à 700 et 800 °C et conserve une intensité et une forme presque constantes.

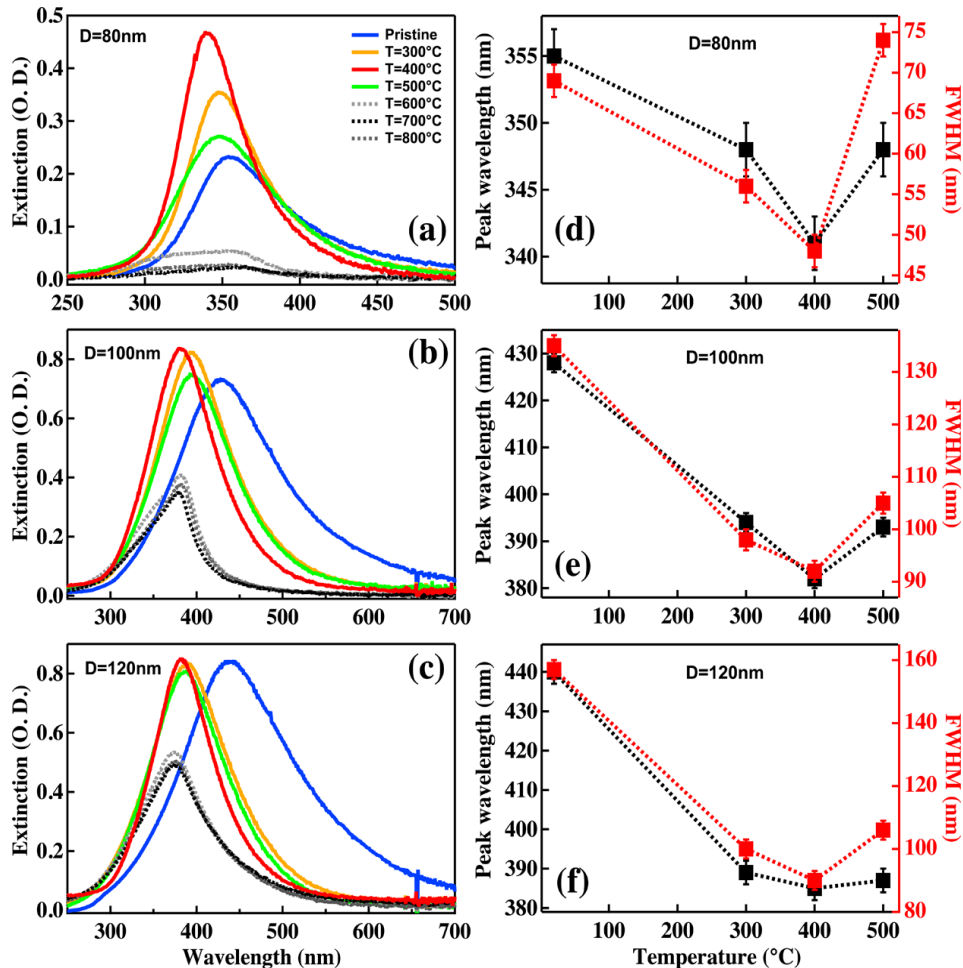


Figure R4. Colonne gauche, pour chaque boîte: spectres d'extinction mesurés sur des nanoparticules d'Al de diamètre fixe après des traitements RTA successifs à température croissante. Colonne droite: évolution de la longueur d'onde maximale et de la largeur à mi-hauteur (FWHM) avec différents traitement RTA. La FWHM et la valeur de la longueur d'onde maximale ne sont pas tracées pour le RTA aux températures les plus élevées (de 600 à 800 °C).

3.2 Interprétation des spectres d'extinction

Résumé

Nous attribuons l'évolution des propriétés plasmoniques des nanodisques d'Al lors des traitements par RTA à deux mécanismes principaux: (i) la diminution du nombre de joints de grains à l'intérieur du métal et (ii) son oxydation. Le premier est dominant à des températures plus basses (jusqu'à 400 °C) lorsque l'oxydation est extrêmement faible et induit la réduction de la FWHM ainsi qu'un décalage bleu de la résonance. Le second effet, dominant à des températures plus élevées (supérieures à 400 °C), augmente l'épaisseur de l'enveloppe d'alumine au détriment du noyau métallique. Aux températures supérieures à 400°C, l'augmentation de la couche d'oxyde devient alors non négligeable. Cela conduit à un comportement plus complexe où un décalage vers le rouge suivi d'un décalage bleu des résonances est mesuré, ainsi qu'une diminution progressive de leur intensité. Ce phénomène est expliqué plus loin par des calculs FDTD.

3.3 Réduction du nombre de joints de grains

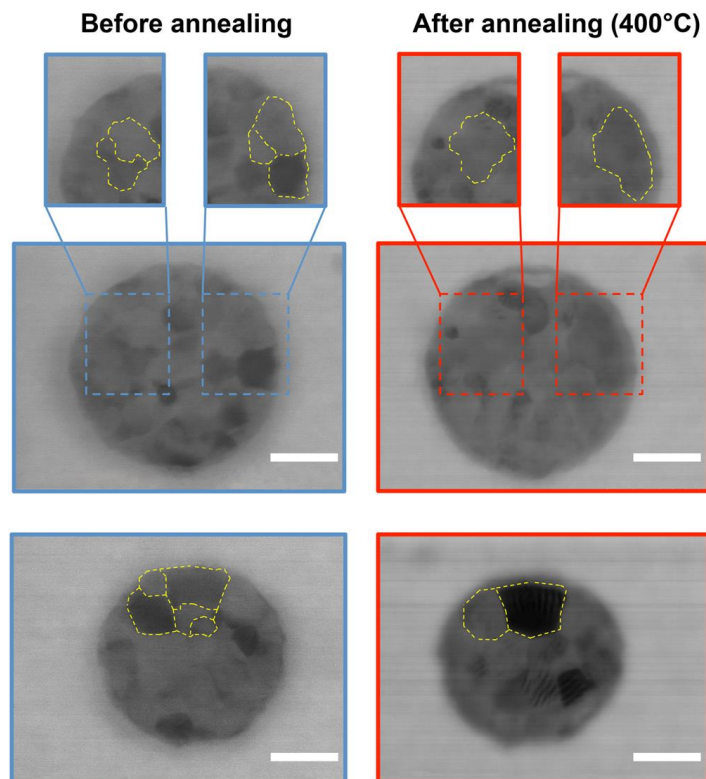


Figure R5. Images TEM sur les mêmes nanoparticules d'Al de diamètre 150 nm (boîtes du haut) et 120 nm (boîtes du bas) avant (boîtes bleues) et après traitement RTA à 400 °C (boîtes rouges). Barres d'échelle = 50 nm.

La polycristallinité des structures vierges est mise en évidence dans grâce à l'imagerie TEM et les grains sont mis en évidence par les lignes jaunes en pointillés sur la Figure R5. Les mêmes nanoparticules après le recuit à 400 °C présentent moins de joints de grains, probablement en raison de la migration des ces derniers à des températures élevées. Certains grains apparaissent alors coalescés sur les images TEM. La réduction du nombre de joints de grain conduit à un nombre plus faible de centres de diffusion pour les électrons, augmentant leur libre parcours moyen et par la suite la durée de vie des résonances plasmoniques. Ceci se traduit également par l'abaissement de la partie imaginaire de la fonction diélectrique du noyau métallique d'aluminium.

3.4 Amélioration du facteur de qualité

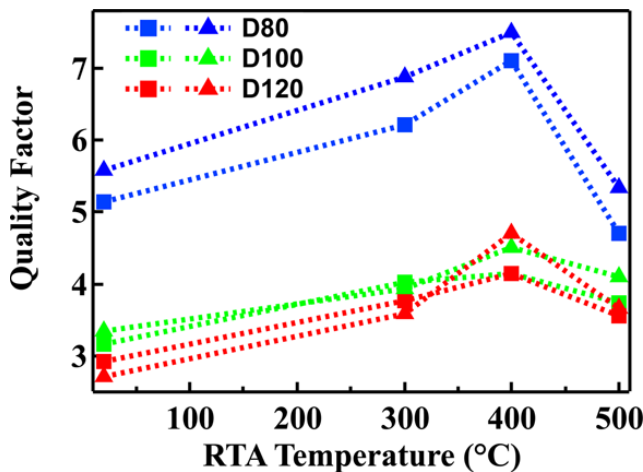


Figure R6. Facteurs de qualité des résonances dipolaires calculées à partir des spectres expérimentaux en fonction de la température du traitement RTA.

Le facteur de qualité Q ($Q = \frac{\lambda_{LSPR}}{FWHM}$) est calculés à partir des spectres expérimentaux pour plusieurs nanoparticules sont représentés sur la Figure R6 en fonction de la température du recuit RTA. Pour chaque nanoparticule, une nette amélioration de Q à 400 ° C est mise en évidence, avec une augmentation relative d'un facteur de 1,4. Pour les nanoparticules plus petites, même si l'amélioration relative est la même, les valeurs absolues de Q sont globalement plus élevées. Nous attribuons cela aux pertes intrinsèques de l'aluminium, qui sont plus faibles pour les longueurs d'onde plus courtes (par exemple, $\varepsilon_2 (\lambda = 450 \text{ nm}) \approx 2\varepsilon_2 (\lambda = 350 \text{ nm})$). Quel que soit le diamètre des nanoparticules, le facteur Q diminue pour le RTA à des températures supérieures à 500 °C en raison de l'augmentation de l'oxydation et de la déformation, phénomènes discutés ci-après.

3.5 Recuit à haute température ($> 400^{\circ}\text{C}$)

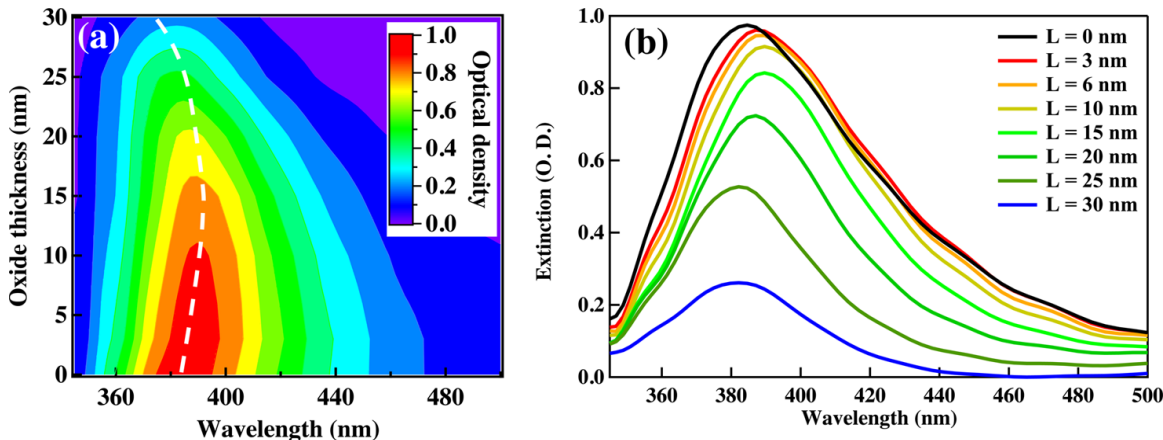


Figure R7. (a) Spectres d'extinction calculés avec FDTD (logiciel OptiFDTD, Optiwave Company) pour un réseau carré de nanoparticules d'Al de diamètre $d = 100$ nm et d'épaisseur $h = 40$ nm pour des rapports différents entre le volume de Al et le volume de couche d'oxyde (de l'épaisseur d'oxyde $L = 0$ nm, pas d'oxydation, à $L = 30$ nm). (b) Spectres d'extinction correspondants pour plusieurs épaisseurs d'oxyde.

Comme le montre la Figure R7, la résonance dipolaire subit d'abord un décalage vers le rouge dû à l'oxydation (en raison de l'indice de réfraction élevé de l'alumine) jusqu'à ce que le noyau métallique atteigne un diamètre de 80 nm correspondant à une couche d'oxyde de 10 nm. À ce stade, la valeur de décalage vers le rouge est d'environ 8 nm. Si le diamètre métallique diminue davantage, alors le décalage vers le bleu dû à la réduction de la taille du noyau métallique prend le dessus sur le red shift du à l'augmentation de la couche d'alumine, entraînant un blue shift net de la position de la résonance ainsi qu'une diminution de son intensité. Enfin, lorsque le noyau métallique atteint un diamètre de 40 nm, on obtient un décalage maximum vers le bleu de la résonance dipolaire ainsi qu'une intensité nettement réduite, diminuée d'un facteur 5. Pour les diamètres inférieurs du noyau métallique, la signature de la résonance dipolaire diminue encore et finit par disparaître. Ces calculs expliquent le comportement des données expérimentales de la Figure R4 pour le RTA de 400 à 800 °C.

3.6 Caractérisation par MEB

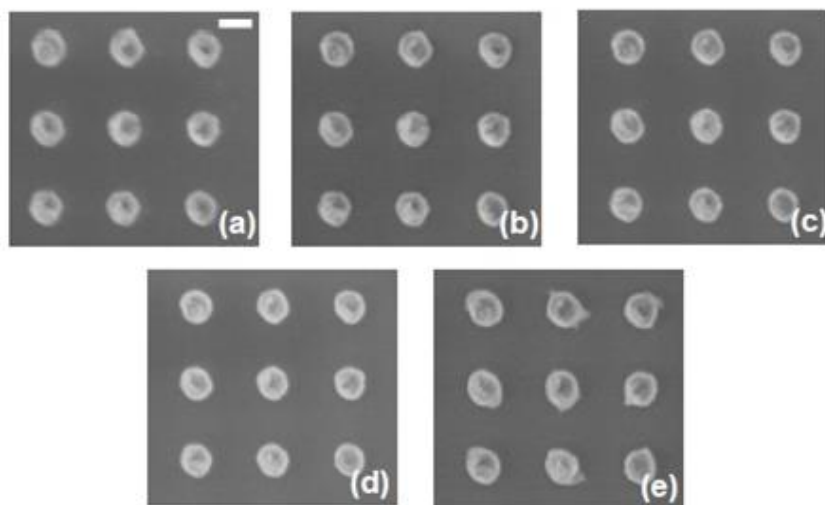


Figure R8. Images au MEB des mêmes nanoparticules d'Al (diamètre 100 nm) vierges (a) et après les procédés RTA ($300\text{ }^{\circ}\text{C}$ (b), $400\text{ }^{\circ}\text{C}$ (c), $500\text{ }^{\circ}\text{C}$ (d), $600\text{ }^{\circ}\text{C}$ (e)). Barre d'échelle 100 nm.

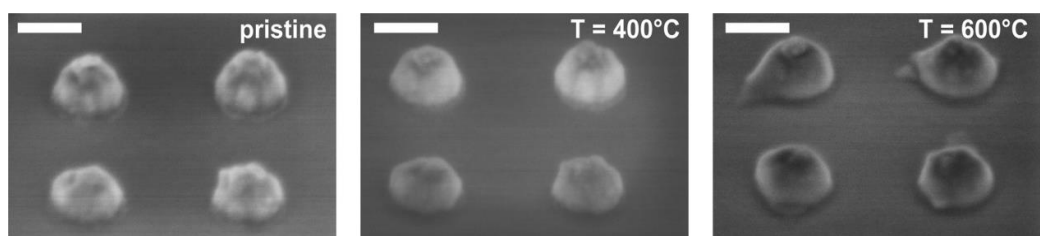


Figure R9. Images MEB inclinées à 45° des réseaux de nanoparticules d'Al avant et après recuits RTA à $T = 400$ et $600\text{ }^{\circ}\text{C}$. Barre d'échelle = 100 nm.

Dans les images MEB (Microscopie Electronique à Balayage) représentées sur la [Figure R8](#), aucun changement significatif de la forme des nanoparticules d'Al n'est observé lors des recuits RTA, sauf celui à $600\text{ }^{\circ}\text{C}$. A cette température et au-dessus, les nanodisques sont déformés, indiquant des changements structurels majeurs tels qu'une forte oxydation déformant leur surface, ce qui explique la détérioration des propriétés plasmoniques après les recuits à haute température. Pour déterminer si un démouillage s'est produit à l'interface substrat-particule, les images MEB ont également été réalisées sous un angle incliné (45°), et sont visibles sur la [Figure R9](#). La même tendance est observée, et aucun démouillage des nanoparticules n'a lieu.

4. Influence de la rugosité de surface les résonances plasmoniques de NP d'aluminium

Résumé

Indépendamment des méthodes expérimentales, les défauts géométriques des NP, tels que de la déformation de forme ou la rugosité de surface sont souvent inévitables. Avec les méthodes classiques de fabrication, à savoir lithographie puis évaporation, la rugosité de surface est un paramètre à prendre en compte particulièrement avec l'aluminium.

4.1 Rugosité sur une nanoparticule isolée

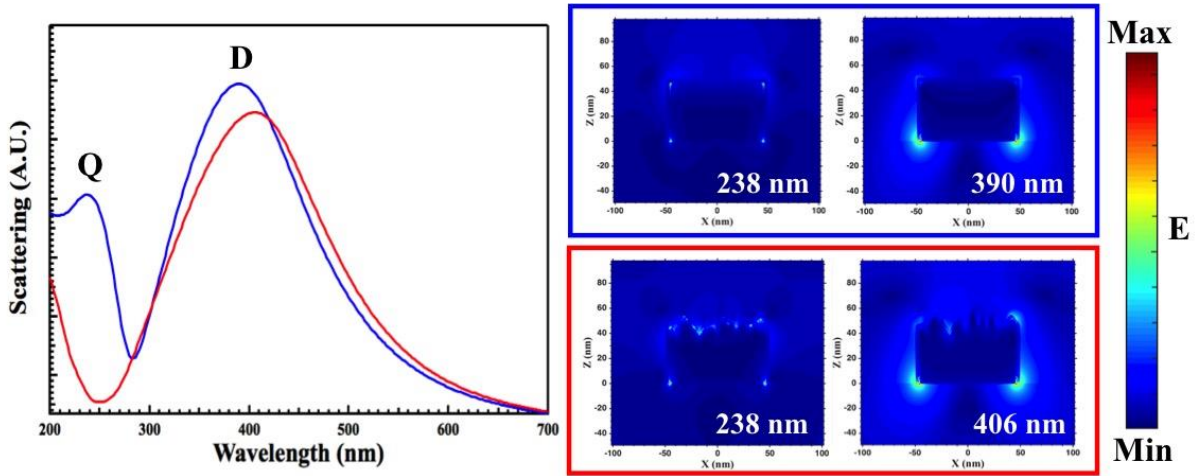


Figure R10. (Gauche) Spectres de diffusion calculés par FDTD d'un nanodisque isolé (diamètre 100 nm, hauteur centrale 50 nm) d'Al avec une rugosité de surface RMS de 0 nm (bleu) et de 5 nm (rouge). (Droite) Distribution du champ électrique autour du nanodisque avec une rugosité de surface RMS de 0 nm (boîte bleue) et de 5 nm (boîte rouge). La longueur d'onde d'excitation est donnée dans l'encart.

Sur la Figure R10 sont représentés les spectres de diffusion calculés pour un nanodisque d'aluminium sans et avec une rugosité de surface de 5 nm (RMS), ainsi que le champ électrique autour de la structure à deux longueurs d'onde excitatrices différentes correspondant au maximum de la résonance dans les deux cas.

Pour le nanodisque sans rugosité, deux pics évidents apparaissent à 238 nm (noté mode Q) et 390 nm (noté mode D). Lorsque la rugosité est incluse (c'est-à-dire RMS 5 nm, ligne rouge sur la Figure R10), le mode D est décalé vers le rouge et affaibli tandis que le mode Q est fortement diminué. Sans rugosité de surface, deux points chauds vifs et intenses orientés côté air sont observés pour le mode Q (238 nm), tandis que les points chauds sont orientés près du substrat pour le mode D (390 et 406 nm). En revanche, une multitude de points chauds

apparaissent sur le dessus de la surface rugueuse, et aucun effet n'est observé sur la distribution des points chauds situés près du substrat. Avant de discuter de l'influence de la rugosité observée ci-dessus, nous allons déterminer par le calcul la nature de ces deux modes de résonance dans la partie qui suit.

4.2 Effet du substrat sur les résonances d'un nanodisque isolé

En analysant les cartes de champs et notamment les localisation des points chauds du champ électrique pour les deux modes Q et D et le profil de leur courbe de diffusion de type Fano sur la [Figure R10 \(courbe bleue\)](#), on peut en déduire que le mode Q est en réalité une résonance quadrupolaire induite par le substrat, et le mode D le mode dipolaire. La distribution de charges de ces modes est cartographiée sur la [Figure R11](#) ci dessous. Cette figure n'est qu'une représentation schématique mais les calculs par FDTD ont été effectués et sont disponibles dans le manuscrit de thèse.

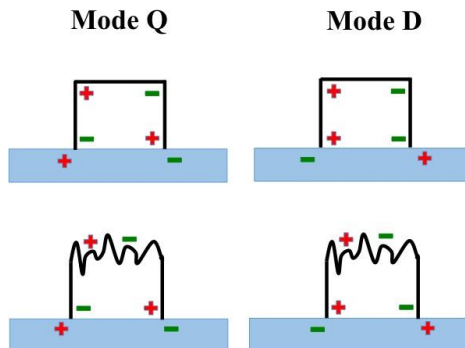


Figure R11. Distribution de charge du mode Q et du mode D sur un nanodisque d'Al avec et sans la rugosité de la surface supérieure.

Pour confirmer cette hypothèse, (qui a déjà été affirmée pour les nanocylindres d'or dans la littérature, référence dans la thèse en anglais) les spectres de diffusion de nanodisques isolés avec ou sans substrat en fonction de leur diamètre sont calculés sur la [Figure R12](#). Sans le substrat, le spectre de diffusion du nanodisque d'Al (trait noir) ne montre qu'un pic correspondant au mode dipolaire connu D. En prenant en compte le substrat, le nouveau mode Q émerge sur des longueurs d'onde plus courtes que celle du mode D, donnant au spectre de diffusion un profil asymétrique de type Fano. De plus, avec le substrat la résonance du mode D est décalée vers le rouge (visible grâce à la ligne pointillée verte de la [Figure R12](#)) et atténuee. En ce qui concerne le mode Q autour de 240 nm, on constate que la longueur d'onde

Résumé

maximale varie peu lorsque le diamètre du nanodisque augmente de 50 nm à 160 nm, comme le confirme la ligne pointillée rouge de la Figure R12. Le creux apparaissant typique d'une résonance Fano est également révélé par la ligne pointillée orange de la Figure R12.

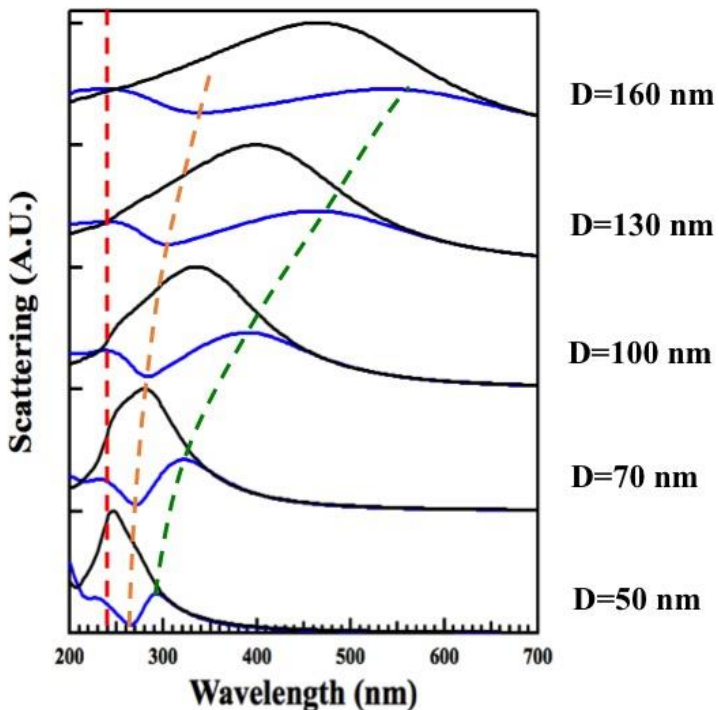


Figure R12. Spectres de diffusion calculés pour des nanodisques d'Al isolés (RMS 0 nm, hauteur 50 nm) en fonction du diamètre avec (bleu) et sans (noir) substrat. Les spectres pour des nanodisques de différentes tailles sont décalés pour une meilleure lisibilité. Les diamètres correspondants sont indiqués sur la droite. Ligne de guidage pour le mode Q (ligne pointillée rouge verticale), le mode D (ligne pointillée verte) et le point de repère (ligne pointillée orange).

4.3 Effet de la rugosité de surface

En raison de la rugosité lors de l'évaporation de l'Al, les charges de surface supérieure ne sont plus entièrement localisées sur le bord du nanodisque, elles sont réparties plus dispersées sur la surface rugueuse sous forme de " hot spots ", bien connus dans la domaine de la plasmonique. Cette rugosité de surface entraîne des pertes par diffusion entraînant une diminution du facteur de qualité des résonances. De plus, si l'on prend en compte cette rugosité, les différents modes supports par les nanocylindres vont être affectés de manières différentes. Comme le montre la Figure R10 (courbe rouge), lorsqu'on inclut la rugosité sur la surface supérieure du nanodisque, le moment dipolaire les modes Q et D sont affectés

différemment. C'est ce qui est discuté dans ce qui suit, à la fois numériquement et expérimentalement sur des réseaux de nanocylindres d'Al.

4.4 Réseau de nanocylindres d'Al avec un pas de 200 nm

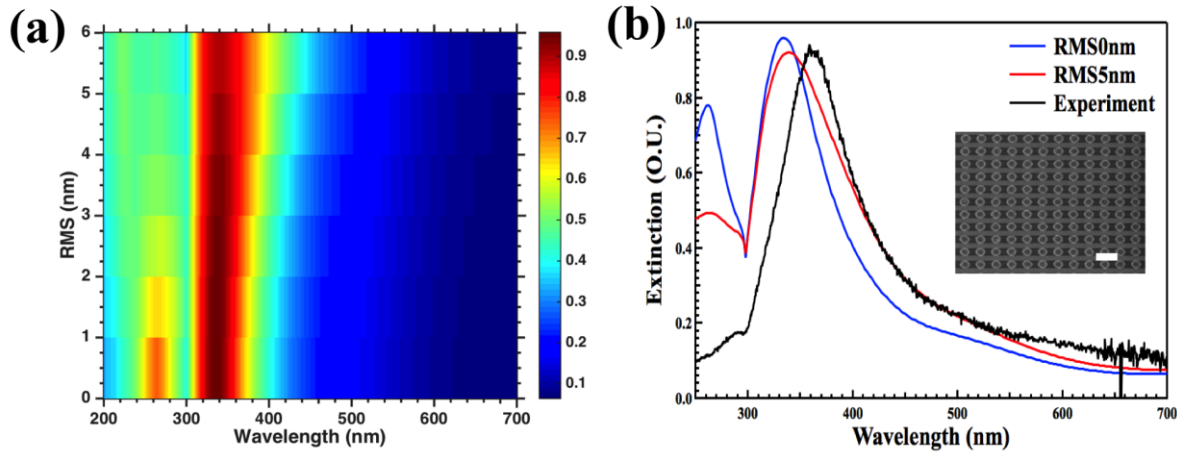


Figure R13. (a) Spectres d'extinction calculés par FDTD du réseau de nanodisques en Al (diamètre 100 nm, hauteur 50 nm et pas de réseau 200 nm) en fonction de la valeur RMS de la rugosité de surface. (b) Spectres d'extinction calculés (RMS 0 nm (bleu) et RMS 5 nm (rouge)) et expérimental (noir, RMS mesurée = 5 nm). L'image SEM insérée montre l'échantillon fabriqué. Barre d'échelle 250 nm.

Dans cette partie, nous étudions l'effet de la rugosité de la surface sur les propriétés optiques des réseaux périodiques de nanodisques d'Al. Les réseaux de nanodisques ont été fabriquées selon la procédure EBL standard sur des substrats de quartz, suivie d'un traitement de recuit à 400 °C pendant 5 minutes pour améliorer le facteur de qualité des résonances. Les spectres d'extinction du réseau périodique (diamètre 100 nm, pas de réseau de 200 nm) en fonction de la valeur RMS de la rugosité de surface sont simulés et représentés sur la Figure R13a. Dans le spectre du disque sans rugosité (RMS 0 nm), deux pics intenses sont observés: le pic à 262 nm correspondant au mode Q et le pic dipolaire à 334 nm correspondant au mode D. Etant donné qu'il s'agit ici d'un réseau, il existe un mode (à l'ordre 1) de réseau ou encore appelé anomalie de Rayleigh aux longueurs d'onde égale à λ (nm) = 200 n, avec n l'indice soit du substrat (quartz) ou du superstrat (air) et 200 le pas du réseau. Cette anomalie de Rayleigh du réseau (0,1) ou (1,0) se situe du côté quartz à environ 300 nm (en prenant n = 1,5 pour le quartz) et du côté air à 200 nm. Dans notre cas, un mode hybride apparaît autour de 200 nm dans la région spectrale du mode Q, qui se traduit par un couplage de ce dernier avec le mode

Résumé

de réseau (0,1) dans l'air, donnant un profil spectral très piqué typique du mode hybride. De même, on peut remarquer un couplage entre le mode dipolaire (mode D) et l'anomalie de Rayleigh à 300 nm, engendrant une légère asymétrie de la résonance dipolaire vers 300 nm. De ces deux effets combinés résultent ainsi le profil du spectre d'extinction très piqué calculé (courbe bleue) pour le réseau de nanodisques d'Al sans rugosité sur substrat de quartz.

Avec une valeur de rugosité non nulle, le calcul montre que la résonance dipolaire est élargie et décalée vers le rouge de 334 nm à 340 nm avec une intensité réduite. Aussi, la résonance correspondant au mode Q à 262 nm est fortement atténuée et disparait même pour une rugosité supérieur à 4 nm. Cet effet peut être attribué aux pertes due à la rugosité qui augmentent l'amortissement de la résonance autour de la nanoparticule d'Al. Dans le spectre expérimental (courbe noire), le pic à la plus courte longueur d'onde est très atténué, bien qu'il y ait toujours un creux Fano évident à 300 nm. Ce résultat est cohérent avec les mesures de rugosité des nanoparticules d'Al fabriquées qui est de 5 nm. Le mode Q du réseau est ainsi fortement atténué. Le mode D est quant à lui bien visible expérimentalement, bien qu'il existe un écart entre celui-ci et sa valeur donnée par calcul pour une même rugosité. Cet écart peut être expliqué par les incertitudes de fabrication, notamment sur les diamètres des nanodisques d'Al, qui présentent nécessairement une certaine distribution.

Les distributions calculées du champ électrique avec (RMS 5 nm) et sans rugosité (RMS 0 nm) aux deux longueurs d'onde de resonance (mode Q et D) sont affichées sur la [Figure R14](#). Les points chauds du nanodisque parfait sans rugosité sont localisées sur les bords de la nanostructure et les champs présent des symétries évidentes. En introduisant une rugosité de 5 nm RMS sur la surface supérieure du nanodisque, les points chauds sur la surface supérieure sont décalés spatialement et les champs sont déformés par la rugosité, avec l'apparition de multiples points chauds répartis aléatoirement sur la surface du nanodisque. En même temps, l'intensité du champ électrique est également diminuée avec la rugosité, ce qui peut être partiellement attribué aux coins arrondis produits par la rugosité supérieure, comme le montrent les [Figures R14 b et d](#). Cependant, l'apparition de ces multiples points chauds sur la surface rugeuse peut être utilisés pour le SERS (Surface Enhanced Raman Scattering) aux courtes longueurs d'onde. Ceci est une piste très intéressante à explorer pour des applications potentielles en détection dans les ultraviolets par spectroscopie Raman exaltée.

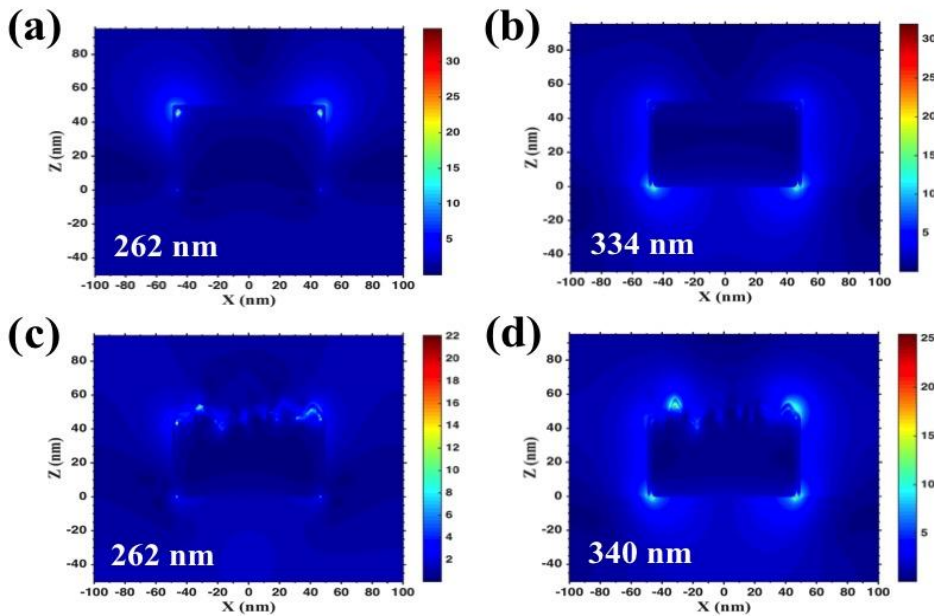


Figure R14. Cartographies du champ électrique calculé par FDTD dans le plan XZ du réseau de nanodisques d’Al (diamètre 100 nm et pas de réseau 200 nm). La polarisation incidente est le long de la direction x et la zone en dessous de Z = 0 nm représente le substrat de quartz. Nanodisque avec une rugosité RMS de 0 nm (excitation à 262 nm (a) et 334 nm (b)) et 5 nm (excitation à 262 nm (c) et 340 nm (d)).

5. Résonances plasmoniques de réseaux de nanoparticules d’Al uniformément désordonnées

En positionnant les NPs dans des réseaux périodiques, les interférences optiques dans le réseau conduisent à un couplage radiatif en champ lointain et donneront des LSPR étroits connus sous le nom de modes de réseau, discutés succinctement ci-dessus. En revanche, en rompant la symétrie du réseau, des complexités surgissent de par le désordre introduit. L’idée dans ce chapitre et d’étudier l’influence de certains désordres de degré contrôlé dans les réseaux de nanoparticules d’Al afin d’étudier l’influence sur les propriétés plasmoniques UV-visibles de ces derniers.

5.1 Méthode pour introduire le désordre

Résumé

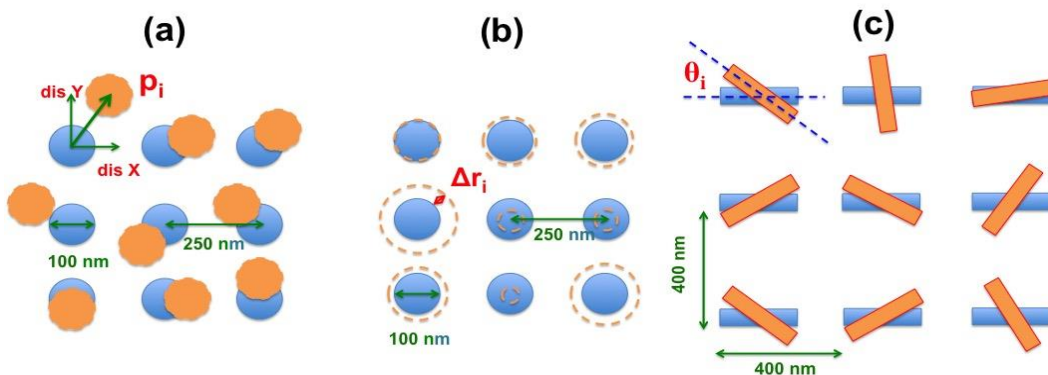


Figure R15. Schémas pour introduire du désordre dans les réseaux en terme de (a) déplacement, (b) taille et (c) rotation des nanostructures.

Des motifs désordonnés ont été générés en ajoutant un nombre aléatoire à certains paramètres de base (position en x et y pour le désordre de déplacement ([Figure R15a](#)), changement de rayon sur chaque nanodisque ([Figure R15b](#)) et angle de rotation sur chaque nano-bâtonnet ([Figure R15c](#))) dans le réseau périodique. Les coordonnées de chaque objet dans le réseau sont obtenues par un programme codé sous Matlab, puis entrées dans le système de lithographie électronique. Pour les réseaux de nanodisques, le diamètre de base a été fixé à 100 nm. Pour le réseau de nano-bâtonnets, la largeur et la longueur du nanorod sont fixées à 50 nm et 140 nm respectivement avec un pas de 400 nm à la fois pour les axes x et y. Dans l'expérience, les nanostructures (d'épaisseur 50 nm) sont disposées dans des zones carrées de $40 \times 40 \mu\text{m}^2$ pour faciliter les mesures optiques ultérieures sur le banc d'extinction. Avant la mesure optique, un recuit thermique rapide a été effectué à 400 °C pendant 5 minutes. Les calculs FDTD sont effectués sur une zone de $10 \times 10 \mu\text{m}^2$ avec ou sans une couche d'oxyde de 4 nm pour chaque nanostructure d'Al. Grâce au grand nombre de NP prises en compte dans les calculs, les résultats numériques concordent bien avec les spectres des expériences de réseau de grandes dimensions dans le plan de l'échantillon comme nous allons le voir.

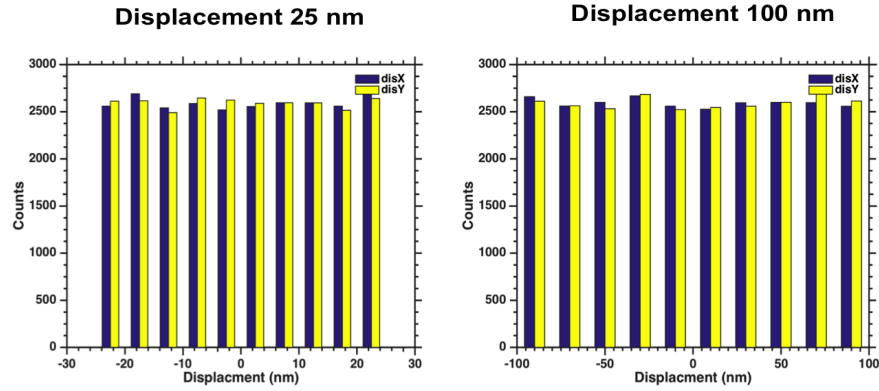


Figure R16. Distribution statistique uniforme des nombres aléatoires utilisés pour le déplacement x et y (nommés disX et disY, comme le montre la figure R15a) des nanodisques d'Al, pour 25 nm et 100 nm de déplacement maximal.

Les distributions des nombres aléatoires générées illustrées la Figure R16 montrent que les nombres aléatoires sont uniformément répartis entre le maximum positif et le maximum négatif autour d'une moyenne arithmétique de zéro. C'est aussi la raison pour laquelle le désordre introduit dans le réseau est uniforme. L'erreur quadratique moyenne (MSE) sur la variation de paramètre à la fois dans l'expérience et la simulation a également été calculée. La valeur MSE augmente avec le degré de désordre.

5.2 Etude du désordre sur la position de nanostructures

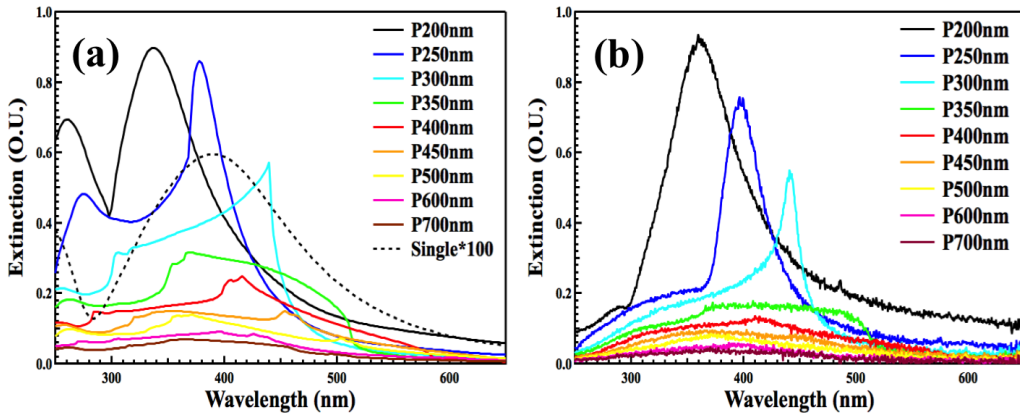


Figure R17. Spectres d'extinction simulés (a) et expérimentaux (b) de réseaux de nanodisques d'Al avec des pas différents. Le diamètre est de 100 nm et le pas (P) varie de 200 à 700 nm. Le spectre calculé pour un nanodisque isolé (pointillé) avec un diamètre de 100 nm est augmenté de 100 fois.

Les anomalies de Rayleigh présentes dans les réseaux périodiques, discutées brièvement au

Résumé

chapitre précédent apparaissent, pour une lumière incidente normale aux longueurs d'ondes :

$$\lambda = \frac{P \times n}{\sqrt{i^2 + j^2}}$$

où P représente le pas du réseau, n est l'indice de réfraction de l'air ($n = 1$) ou du quartz ($n = 1,5$), et i, j est l'ordre de diffraction du réseau bidimensionnel. Ces anomalies peuvent se coupler plus ou moins efficacement aux résonances plasmoniques des nanostructures métalliques du réseau donnant naissance aux fameux mode de réseaux hybrides. Ces modes hybrides présentent en général un profil plus asymétrique de type Fano et un meilleur facteur de qualité que les résonances plasmoniques en l'absence de couplage. Ces modes hybrides sont retrouvés par le calcul comme il est illustré dans la [Figure R17](#). Les spectres expérimentaux sont en assez bon accord avec la théorie, excepté pour certains pas de réseau et aux courtes longueurs d'onde. Comme expliqué dans le texte précédent, les spectres expérimentaux présentent une résonance bien moins marquée à 250 nm (mode Q) ce qui peut être attribué à la rugosité de la surface. Dans la suite, nous avons choisi de travailler avec des réseau d'un pas de 250 nm, qui présentent une asymétrie faible et une résonance dipolaire assez fine autour de 400 nm afin de faciliter l'étude sur le déplacement aléatoire des nanostructures.

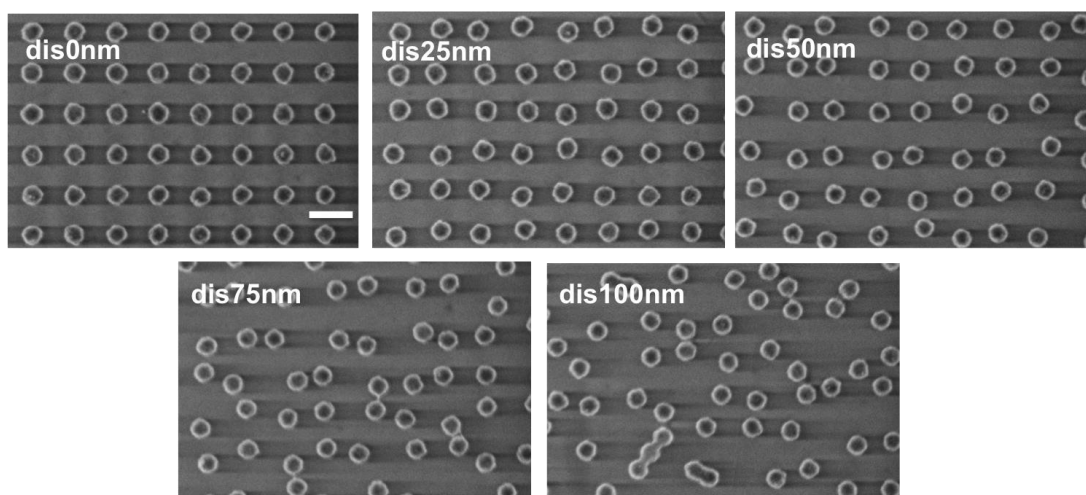


Figure R18. Images MEB de réseaux de nanodisques (diamètre 100 nm, pas de base 250 nm) avec des désordres différents. Barre d'échelle 250 nm.

Cinq échantillons avec un déplacement aléatoire maximal de 0, 25, 50, 75 et 100 nm sont montrés sur la [Figure R18](#), nommés dis0nm, dis25nm, dis50nm, dis75nm et dis100nm respectivement. On remarque que certains nanodisques peuvent se chevaucher lorsque le déplacement maximum est supérieur à 75 nm. Cependant, il y a théoriquement moins de 0,1%

de nanostructures qui se chevauchent. La fonction de distribution radiale d'autocorrélation $g(s)$ est généralement utilisée pour décrire la distribution d'un système aléatoire:

$$g(s) = 2\pi s \cdot \rho(s) \cdot ds$$

où s représente la distance par rapport au centre d'un disque de référence; ρ représente la densité de nanostructures par unité de surface. Un schéma représentant le calcul de $g(s)$ est donné sur la [Figure R19a](#). La fonction $g(s)$ devient une relation linéaire avec la distance s lorsque le degré de désordre augmente. Ceci indique que la densité ρ devient constante dans toute la zone lorsque le déplacement aléatoire maximal est fixé à 100 nm. Par conséquent, les nanodisques sont répartis de manière de plus en plus homogène dans la zone spatiale avec un désordre croissant.

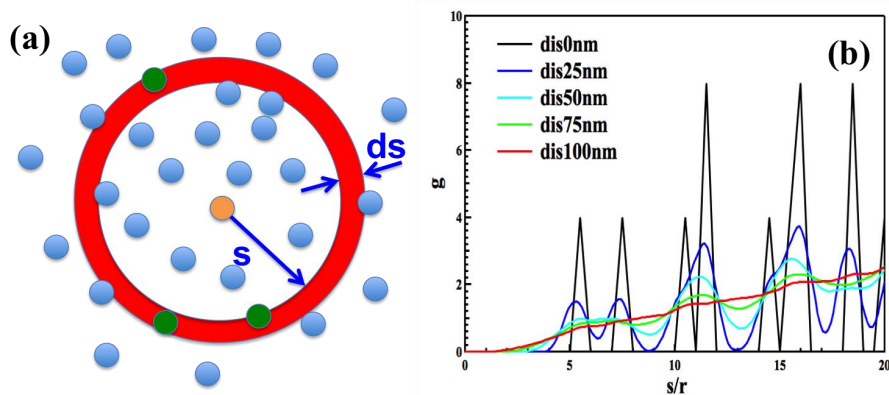


Figure R19. (a) Schéma du calcul de la fonction de distribution radiale. (b) Fonction de distribution radiale moyenne pour le réseau de nanodisques (diamètre de 100 nm, pas de 250 nm) avec un désordre différent calculé à partir des coordonnées expérimentales. r est le rayon du nanodisque, c'est-à-dire 50 nm.

Les spectres d'extinction calculés et mesurés expérimentalement sont présentés sur la [Figure R20](#). Il s'agit de réseaux de nanodisques d'Al (100 nm, pas de 250 nm) avec divers degrés de désordre présentés sur les images MEB de la figure R18 précédente. Un bon accord est visible entre l'expérience et le calcul, particulièrement pour la résonance plasmonique dipolaire centrée aux alentours de 400 nm. La position de la résonance est très peu affectée par le désordre croissant. Cependant, son intensité va en diminuant avec le désordre, le tout accompagné par une forte augmentation de sa largeur à mi hauteur. Cet effet est attribué d'une part à l'annulation progressive du mode hybride. Plus le désordre est élevé, moins l'anomalie de Rayleigh est présente et plus le profil de la résonance s'éloigne d'un profil Fano pour se rapprocher de celui d'une résonance individuelle, plus large. De plus, comme les cartographie de champs électrique le confirment dans la [Figure R20 \(c-e\)](#), avec une désordre élevé, certains nanodisques se retrouvent très rapprochés, ayant pour conséquence l'apparition

Résumé

de résonance dans les gap des dimères, connues pour être légèrement décalées vers les plus grandes longueurs d'onde par rapport à des particules seules. L'apparition de dimères aléatoires avec un gap aléatoire également apporte donc une distribution plus grande de longueurs d'ondes de résonances plasmoniques contribuant à l'élargissement global du spectre d'extinction.

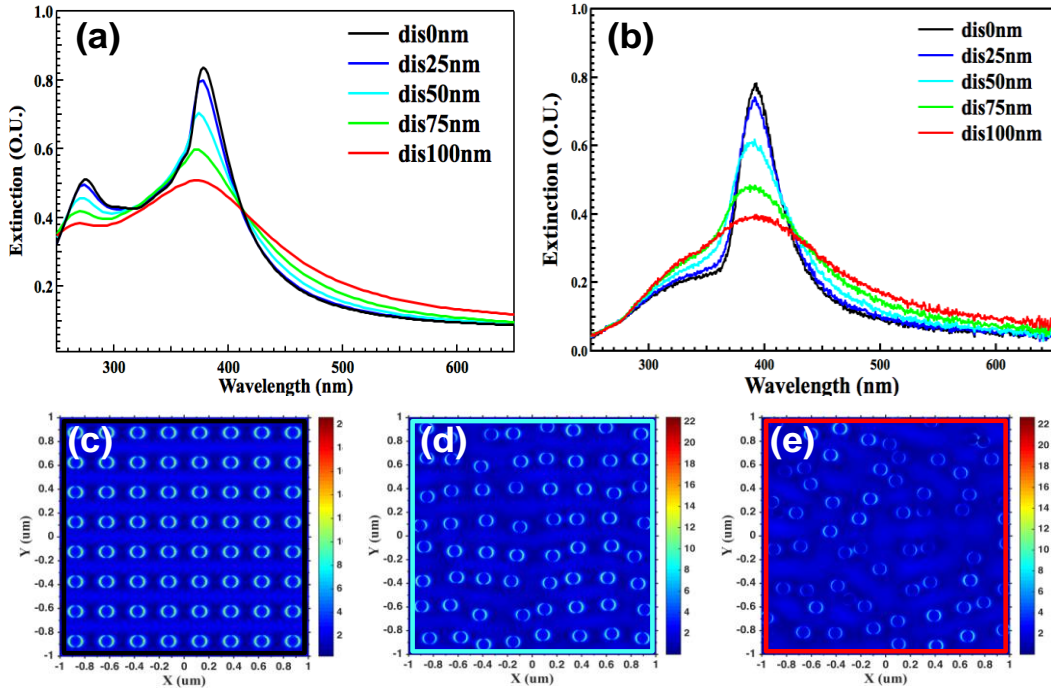


Figure R20. Spectres d'extinction calculés (a) et expérimentaux (b) pour un réseau de nanodisques (diamètre 100 nm, pas de base 250 nm) avec différents degrés de désordre. Des cartes de champs électriques de trois degrés de désordre sous excitation à 378 nm sont données pour dis0nm (c), dis50nm (d) et dis100nm (e).

5.3 Etude du désordre sur les dimensions des nanostructures

Le rayon de chaque nanodisque (rayon de base 50 nm) dans un réseau périodique est ici modifié en ajoutant un nombre aléatoire. Les échantillons sont nommés de la manière suivante: size0nm (rayon 50 nm, sans désordre), size10nm (rayon variant aléatoirement de 40 nm à 60 nm) et size20nm (rayon variant aléatoirement de 30 nm à 70 nm). Les spectres d'extinction calculés et expérimentaux de ces réseaux sont montrés sur les [Figures R21 \(a\)](#) et [\(b\)](#), respectivement. Comme nous l'avons déjà exposé précédemment, la résonance autour de 276 nm sur la [Figure R21b](#) est attribuée au couplage entre le mode réseau et le mode Q dû à

l'apparition de substrat qui ne varie pas beaucoup avec la taille du nanodisque. Par conséquent, même en faisant varier la taille de NP tout en conservant la périodicité, la variation aléatoire du diamètre affecte peu la signature optique à 276 nm, comme le montre la Figure R21b, car la périodicité du réseau est conservée. Quant au mode autour de 378 nm, attribué à la résonance dipolaire, celui-ci est plus influencé par le diamètre des NP d'Al.

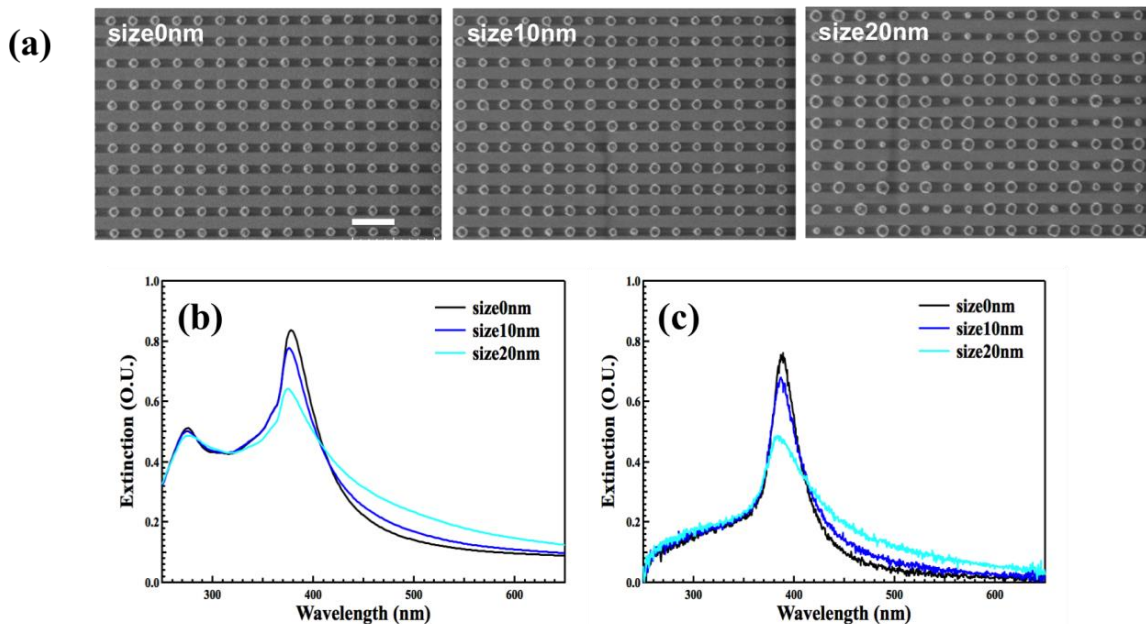


Figure R21. (a) Images MEB de réseaux (pas 250 nm) avec des nanodisques de diamètres uniformément désordonnées. Barre d'échelle 500 nm. Spectres d'extinction calculés (b) et expérimentaux (c) pour un réseau de nanodisques avec trois degrés de désordre.

Sans changer la périodicité dans le tableau, il préserve toujours l'effet réseau et le couplage avec l'anomalie de Rayleigh. Par conséquent, le désordre introduit sur la répartition en taille, conservant la nature hybride du mode, conserve également un facteur de qualité amélioré typique du mode hybride, et donc la réponse spectrale subit un élargissement des résonances dipolaires plasmoniques beaucoup moins prononcé que pour le désordre sur la position des nanodisques, observé précédemment. Cela dit, en raison du caractère aléatoire uniforme introduit dans la valeur du rayon, les résonances dipolaires des différents nanodisques sont réparties également autour de la résonance moyenne. Ainsi la somme des contributions de chaque nanodisque d'Al de différents diamètres aboutit à un spectre d'extinction du réseau qui s'élargit avec le désordre croissant, tout en diminuant en intensité.

5.4 Etude du désordre sur la rotation des nanostructures

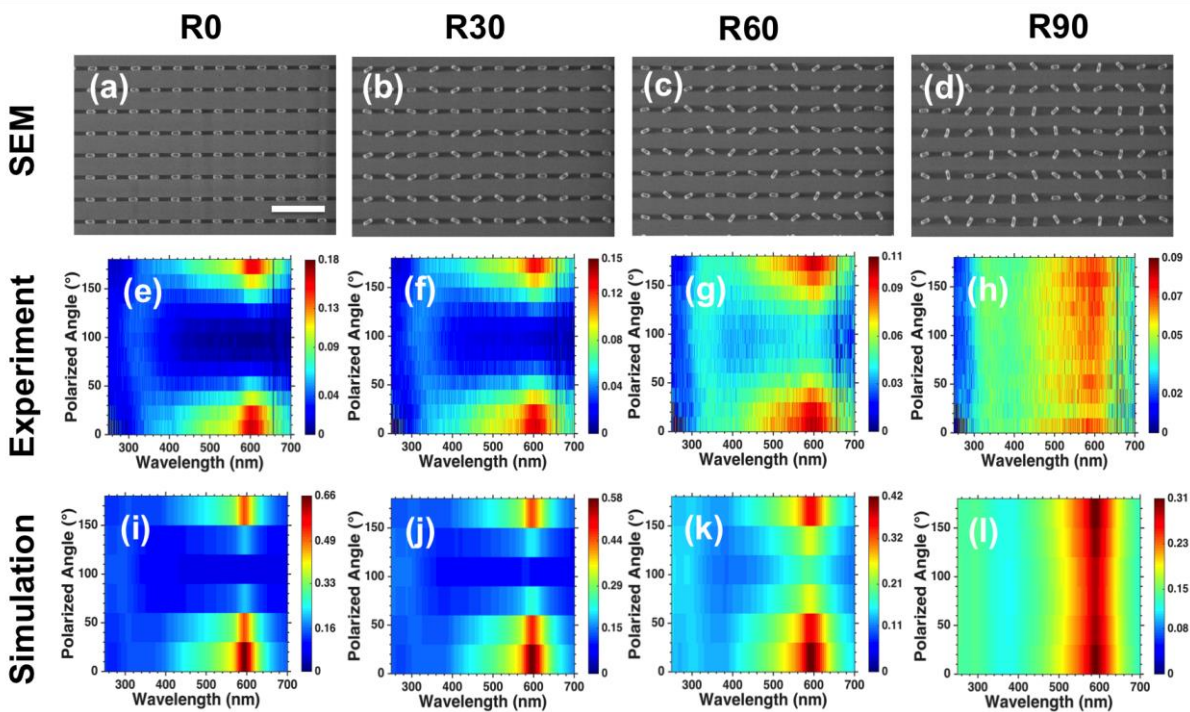


Figure R22. La rangée supérieure (a-d) montre des images MEB de réseaux de nano-bâtonnets d'aluminium (axe court 50 nm, axe long 140 nm) dans lesquels ces derniers ont été progressivement mis en rotation de manière aléatoire. Spectres d'extinction en incidence normale expérimentaux (deuxième rangée (e-h)) et calculés (troisième rangée (i-l)) de réseaux correspondants avec différents angles de polarisation de l'illumination incidente.

Un nano-bâtonnet en aluminium bien conçu peut avoir une résonance plasmonique dans le visible le long de son grand axe tout en ayant une résonance plasmonique dans le proche UV le long de son petit axe. Pour de telles nanostructures sensibles à la polarisation, il est possible d'introduire un angle de rotation aléatoire. Un angle maximum θ est choisi et chaque nanorod est tourné de manière aléatoire le long de son grand axe avec un angle compris entre $-\theta$ et θ . Les échantillons ont ensuite été nommés R0, R30, R60 et R90, respectivement pour $\theta = 0, 30^\circ, 60^\circ$ et 90° . Les images MEB dans la rangée supérieure de la Figure R22 (a-d) représentent des réseaux de nano-bâtonnets d'Al avec $\theta = 0, 30^\circ, 60^\circ$ et 90° respectivement. Leurs spectres d'extinction respectifs calculés par FDTD et obtenus expérimentalement sont visibles également. Pour un angle de polarisation de 0° (le long de l'axe long), le nombre de nano-bâtonnets excités efficacement diminue avec le caractère aléatoire, affaiblissant l'intensité du pic d'extinction à 600 nm dans l'expérience. Pour le désordre de rotation le plus élevé (Figure R22 d, h, l), les spectres d'extinction deviennent insensibles à la polarisation en raison de la quantité équivalente de nano-bâtonnets tournés à différents angles dans le réseau.

Il en résulte un spectre d'extinction large et homogène, de 300 à 700 nm pour toute polarisation de la lumière incidente. Le même raisonnement peut être établi pour la résonance selon le petit axe, à 300 nm visible sur les spectres d'extinction. La simulation et l'expérience confirment le même phénomène.

6. Conclusion

Dans cette thèse, nous avons étudié numériquement et expérimentalement les propriétés plasmoniques de réseaux de nano-structures d'aluminium. Plusieurs paramètres cruciaux pour le contrôle des propriétés plasmoniques des ces réseaux tel que l'oxydation des nanostructures, leur réaction aux élévations de température, leur rugosité de surface, ou encore les effets de réseaux ordonnés ou au contraire désordonnés ont été étudiés. Sur la base des résultats obtenus dans cette thèse et des recherches antérieures, il apparaît que les propriétés plasmoniques des réseaux de nanostructures d'aluminium lithographiés laissent entrevoir de nombreuses fonctionnalités dans tout le spectre visible et proche ultraviolet.

Au cours de la procédure de fabrication et de la période de stockage et d'utilisation des nanostructures lithographiées dans ce travail de thèse, il apparaît que la stabilité de tels réseaux est assez longue, de 90 jours, ce qui pose toutefois de véritables questions sur l'utilisation pérennes de telles structures et de leur utilisation industrielle. En effet, pour la production commerciale à grande échelle à l'avenir, des études sur la stabilisation de ces structures devra être effectuée. Un traitement supplémentaire pourrait être étudié et utilisé pour prolonger et stabiliser les résonances plasmoniques de l'aluminium nanostructuré.

Deuxièmement, nous étudions l'influence du recuit thermique rapide sur les propriétés plasmoniques des nanostructures d'Al. Une amélioration des résonances plasmoniques se traduisant par une réduction de leur largeur à mi-hauteur est constatée après un recuit à 400 °C pendant 5 minutes des nanostructures. Cet effet est attribué à la diminution du nombre de joints de grains à l'intérieur des nanoparticules d'aluminium, comme le prouvent les mesures TEM.

Troisièmement, nous dévoilons l'effet de la rugosité de surface sur les propriétés plasmoniques des nanostructures d'Al. Ainsi la rugosité de surface des nanodisques en Al

Résumé

provoque la disparition du mode quadrupolaire induit par le substrat, mode supporté par les nanodisques déposés sur substrat. En même temps, la rugosité induit un affaiblissement du mode dipolaire plasmonique supporté également dans les nanodisques.

Enfin, nous étudions numériquement et expérimentalement l'effet du désordre uniforme introduit dans des réseaux de nanoparticules d'aluminium. En faisant varier le déplacement, le rapport d'aspect ou la rotation de chaque nanoparticule dans les réseaux périodiques, l'influence du désordre uniforme sur les résonances plasmoniques est étudiée dans la région du proche ultraviolet et du visible. Les propriétés plasmoniques UV-Vis de tels réseaux désordonnés sont révélées. Par exemple, il est montré que les réseaux de nano-bâtonnets d'aluminium présentent des résonances plasmoniques dépendantes de (et contrôlable) la polarisation de la lumière incidente à la fois dans le domaine du proche ultraviolet et du visible. De tels réseaux peuvent avoir des applications dans les cellules solaires, qui nécessitent une absorption à la fois dans le proche ultraviolet et dans toute la plage visible.

References

- ¹ Griffiths D J. Introduction to Electrodynamics, 3rd ed [M]. Prentice Hall, 1999.
- ² Ross M B, Schatz G C. Aluminum and indium plasmonic nanoantennas in the ultraviolet [J]. The Journal of Physical Chemistry C, 2014, 118(23): 12506-12514.
- ³ Maier S A. Plasmonics: fundamentals and applications [M]. Springer Science & Business Media, 2007.
- ⁴ Norek M, Włodarski M, Stępiński W J. Tailoring of UV/violet plasmonic properties in Ag, and Cu coated Al concaves arrays [J]. Applied Surface Science, 2014, 314: 807-814.
- ⁵ Murray W A, Barnes W L. Plasmonic materials [J]. Advanced materials, 2007, 19(22): 3771-3782.
- ⁶ Giannini V, Fernández-Domínguez A I, Heck S C, et al. Plasmonic nanoantennas: fundamentals and their use in controlling the radiative properties of nanoemitters [J]. Chemical reviews, 2011, 111(6): 3888-3912.
- ⁷ Stockman M I. Nanoplasmonics: The physics behind the applications [J]. Phys. Today, 2011, 64(2): 39-44.
- ⁸ Barnes W L, Dereux A, Ebbesen T W. Surface plasmon subwavelength optics [J]. Nature, 2003, 424(6950): 824.
- ⁹ Ditlbacher H, Hohenau A, Wagner D, et al. Silver nanowires as surface plasmon resonators [J]. Physical review letters, 2005, 95(25): 257403.
- ¹⁰ Tang F, Adam P M, Boutami S. Theoretical investigation of SERS nanosensors based on hybrid waveguides made of metallic slots and dielectric strips [J]. Optics express, 2016, 24(19): 21244-21255.
- ¹¹ Akimov A V, Mukherjee A, Yu C L, et al. Generation of single optical plasmons in metallic nanowires coupled to quantum dots [J]. Nature, 2007, 450(7168): 402.
- ¹² Le Ru E, Etchegoin P. Principles of Surface-Enhanced Raman Spectroscopy: and related plasmonic effects [M]. Elsevier, 2008.
- ¹³ Powell C J, Swan J B. Origin of the characteristic electron energy losses in aluminum [J]. Physical Review, 1959, 115(4): 869.
- ¹⁴ Gérard D, Gray S K. Aluminium plasmonics [J]. Journal of Physics D: Applied Physics, 2014, 48(18): 184001.

References

- ¹⁵ Picardi G, Colas F J, Gillibert R, et al. Spectral Shift of the Plasmon Resonance Between the Optical Extinction and Absorption of Gold and Aluminum Nanodisks [J]. *The Journal of Physical Chemistry C*, 2016, 120(45): 26025-26033.
- ¹⁶ McMahon J M, Schatz G C, Gray S K. Plasmonics in the ultraviolet with the poor metals Al, Ga, In, Sn, Tl, Pb, and Bi [J]. *Physical Chemistry Chemical Physics*, 2013, 15(15): 5415-5423.
- ¹⁷ Sanz J M, Ortiz D, Alcaraz De La Osa R, et al. UV plasmonic behavior of various metal nanoparticles in the near-and far-field regimes: geometry and substrate effects [J]. *The Journal of Physical Chemistry C*, 2013, 117(38): 19606-19615.
- ¹⁸ Langhammer C, Schwind M, Kasemo B, et al. Localized surface plasmon resonances in aluminum nanodisks [J]. *Nano letters*, 2008, 8(5): 1461-1471.
- ¹⁹ Li Y, Kalia R K, Nakano A, et al. Size effect on the oxidation of aluminum nanoparticle: Multimillion-atom reactive molecular dynamics simulations [J]. *Journal of Applied Physics*, 2013, 114(13): 134312.
- ²⁰ Foley T J, Johnson C E, Higa K T. Inhibition of oxide formation on aluminum nanoparticles by transition metal coating [J]. *Chemistry of materials*, 2005, 17(16): 4086-4091.
- ²¹ Meziani M J, Bunker C E, Lu F, et al. Formation and properties of stabilized aluminum nanoparticles [J]. *ACS applied materials & interfaces*, 2009, 1(3): 703-709.
- ²² Zhou L, Zhang C, McClain M J, et al. Aluminum nanocrystals as a plasmonic photocatalyst for hydrogen dissociation [J]. *Nano letters*, 2016, 16(2): 1478-1484.
- ²³ Firmansyah D A, Sullivan K, Lee K S, et al. Microstructural behavior of the alumina shell and aluminum core before and after melting of aluminum nanoparticles [J]. *The Journal of Physical Chemistry C*, 2011, 116(1): 404-411.
- ²⁴ Nylund, A., Mizuno, K., & Olefjord, I. (1998). Influence of Mg and Si on the oxidation of aluminum. *Oxidation of Metals*, 50(3-4), 309-325.
- ²⁵ Coulet M V, Rufino B, Esposito P H, et al. Oxidation Mechanism of Aluminum Nanopowders [J]. *The Journal of Physical Chemistry C*, 2015.
- ²⁶ Ding T, Sibley D, Zhang L, et al. Controllable Tuning Plasmonic Coupling with Nanoscale Oxidation [J]. *ACS nano*, 2015.
- ²⁷ Tinguely J C, Sow I, Leiner C, et al. Gold nanoparticles for plasmonic biosensing: the role of metal crystallinity and nanoscale roughness [J]. *BioNanoScience*, 2011, 1(4): 128-135.

- ²⁸ Macias G, Alba M, Marsal L F, et al. Surface roughness boosts the SERS performance of imprinted plasmonic architectures [J]. *Journal of Materials Chemistry C*, 2016, 4(18): 3970-3975.
- ²⁹ Zhang Q, Li G, Liu X, et al. A room temperature low-threshold ultraviolet plasmonic nanolaser [J]. *Nature communications*, 2014, 5: 4953.
- ³⁰ Chung Y C, Cheng P J, Chou Y H, et al. Surface roughness effects on aluminium-based ultraviolet plasmonic nanolasers [J]. *Scientific reports*, 2017, 7: 39813.
- ³¹ Ning T, Gao S, Huo Y, et al. Third-harmonic generation from gold nanowires of rough surface considering classical nonlocal effect [J]. *Optics Express*, 2017, 25(6): 6372-6382.
- ³² Zhu X, Zhang Y, Zhang J, et al. Ultrafine and smooth full metal nanostructures for plasmonics [J]. *Advanced Materials*, 2010, 22(39): 4345-4349.
- ³³ Nagpal P, Lindquist N C, Oh S H, et al. Ultrasmooth patterned metals for plasmonics and metamaterials [J]. *Science*, 2009, 325(5940): 594-597.
- ³⁴ Thyagarajan K, Santschi C, Langlet P, et al. Highly improved fabrication of Ag and Al nanostructures for UV and nonlinear plasmonics [J]. *Advanced Optical Materials*, 2016, 4(6): 871-876.
- ³⁵ Mahapatro A K, Scott A, Manning A, et al. Gold surface with sub-nm roughness realized by evaporation on a molecular adhesion monolayer [J]. *Applied Physics Letters*, 2006, 88(15): 151917.
- ³⁶ De Angelis F, Gentile F, Mecarini F, et al. Breaking the diffusion limit with superhydrophobic delivery of molecules to plasmonic nanofocusing SERS structures [J]. *Nature Photonics*, 2011, 5(11): 682-687.
- ³⁷ Sigle D O, Perkins E, Baumberg J J, et al. Reproducible deep-UV SERRS on aluminum nanovoids [J]. *The journal of physical chemistry letters*, 2013, 4(9): 1449-1452.
- ³⁸ Tian S, Neumann O, McClain M J, et al. Aluminum Nanocrystals: a sustainable substrate for quantitative SERS-based DNA detection [J]. *Nano Lett*, 2017, 17(8): 5071-5077.
- ³⁹ Yang Z L, Li Q H, Ren B, et al. Tunable SERS from aluminium nanohole arrays in the ultraviolet region [J]. *Chemical Communications*, 2011, 47(13): 3909-3911.
- ⁴⁰ Jha S K, Ahmed Z, Agio M, et al. Deep-UV surface-enhanced resonance Raman scattering of adenine on aluminum nanoparticle arrays [J]. *Journal of the American Chemical Society*, 2012, 134(4): 1966-1969.

References

- ⁴¹ Jha S K, Ekinci Y, Agio M, et al. Towards deep-UV surface-enhanced resonance Raman spectroscopy of explosives: ultrasensitive, real-time and reproducible detection of TNT [J]. Analyst, 2015, 140(16): 5671-5677.
- ⁴² Sharma B, Cardinal M F, Ross M B, et al. Aluminum Film-Over-Nanosphere Substrates for Deep-UV Surface-Enhanced Resonance Raman Spectroscopy [J]. Nano letters, 2016, 16(12): 7968-7973.
- ⁴³ Li X M, Bi M H, Cui L, et al. 3D Aluminum Hybrid Plasmonic Nanostructures with Large Areas of Dense Hot Spots and Long- Term Stability [J]. Advanced Functional Materials, 2017, 27(10).
- ⁴⁴ Gillibert R, Colas F, Yasukuni R, et al. Plasmonic Properties of Aluminum Nanocylinders in the Visible Range [J]. The Journal of Physical Chemistry C, 2017, 121(4): 2402-2409.
- ⁴⁵ Mogensen K B, Gühlke M, Kneipp J, et al. Surface-enhanced Raman scattering on aluminum using near infrared and visible excitation [J]. Chemical Communications, 2014, 50(28): 3744-3746.
- ⁴⁶ Goffard J, Gérard D, Miska P, et al. Plasmonic engineering of spontaneous emission from silicon nanocrystals [J]. Scientific reports, 2013, 3: 2672.
- ⁴⁷ Okamoto K, Niki I, Shvartser A, et al. Surface-plasmon-enhanced light emitters based on InGaN quantum wells [J]. Nature materials, 2004, 3(9): 601.
- ⁴⁸ Cho C Y, Zhang Y, Cicek E, et al. Surface plasmon enhanced light emission from AlGaN-based ultraviolet light-emitting diodes grown on Si (111) [J]. Applied Physics Letters, 2013, 102(21): 211110.
- ⁴⁹ Kannegulla A, Liu Y, Wu B, et al. Aluminum ultraviolet-visible plasmonic arrays for broadband and wavelength-selective enhancements of quantum dot emission [J]. Applied Physics Letters, 2017, 111(8): 081106.
- ⁵⁰ Forestiere C, Handin A, Dal Negro L. Enhancement of molecular fluorescence in the UV spectral range using aluminum nanoantennas [J]. Plasmonics, 2014, 9(3): 715-725.
- ⁵¹ Jiao X, Peterson E M, Harris J M, et al. UV fluorescence lifetime modification by aluminum nanoapertures [J]. ACS Photonics, 2014, 1(12): 1270-1277.
- ⁵² Chowdhury M H, Ray K, Gray S K, et al. Aluminum nanoparticles as substrates for metal-enhanced fluorescence in the ultraviolet for the label-free detection of biomolecules [J]. Analytical chemistry, 2009, 81(4): 1397.

- ⁵³ Ray K, Chowdhury M H, Lakowicz J R. Aluminum nanostructured films as substrates for enhanced fluorescence in the ultraviolet-blue spectral region [J]. *Analytical chemistry*, 2007, 79(17): 6480.
- ⁵⁴ Eizner E, Avayu O, Dicovski R, et al. Aluminum nanoantenna complexes for strong coupling between excitons and localized surface plasmons [J]. *Nano letters*, 2015, 15(9): 6215-6221.
- ⁵⁵ Gérard D, Wenger J, Bonod N, et al. Nanoaperture-enhanced fluorescence: Towards higher detection rates with plasmonic metals [J]. *Physical Review B*, 2008, 77(4): 045413.
- ⁵⁶ Tan S J, Zhang L, Zhu D, et al. Plasmonic color palettes for photorealistic printing with aluminum nanostructures [J]. *Nano letters*, 2014, 14(7): 4023-4029.
- ⁵⁷ Li Z, Clark A W, Cooper J M. Dual color plasmonic pixels create a polarization controlled nano color palette [J]. *ACS Nano*, 2016, 10 : 492–498.
- ⁵⁸ Wen L, Chen Q, Hu X, et al. Multifunctional Silicon Optoelectronics Integrated with Plasmonic Scattering Color [J]. *ACS nano*, 2016, 10(12): 11076-11086.
- ⁵⁹ Roberts A S, Pors A, Albrektsen O, et al. Subwavelength plasmonic color printing protected for ambient use [J]. *Nano letters*, 2014, 14(2): 783-787.
- ⁶⁰ Cheng F, Gao J, Stan L, et al. Aluminum plasmonic metamaterials for structural color printing [J]. *Optics express*, 2015, 23(11): 14552-14560.
- ⁶¹ Olson J, Manjavacas A, Basu T, et al. High chromaticity aluminum plasmonic pixels for active liquid crystal displays [J]. *ACS nano*, 2015, 10(1): 1108-1117.
- ⁶² James T D, Mulvaney P, Roberts A. The plasmonic pixel: large area, wide gamut color reproduction using aluminum nanostructures [J]. *Nano letters*, 2016, 16(6): 3817-3823.
- ⁶³ Zhou L, Tan Y, Wang J, et al. 3D self-assembly of aluminium nanoparticles for plasmon-enhanced solar desalination [J]. *Nature Photonics*, 2016, 10(6): 393-398.
- ⁶⁴ Temple T L, Bagnall D M. Optical properties of gold and aluminium nanoparticles for silicon solar cell applications [J]. *Journal of Applied Physics*, 2011, 109(8): 084343.
- ⁶⁵ Lee M, Kim J U, Lee K J, et al. Aluminum nanoarrays for plasmon-enhanced light harvesting [J]. *ACS nano*, 2015, 9(6): 6206-6213.
- ⁶⁶ Krause D, Teplin C W, Rogers C T. Optical surface second harmonic measurements of isotropic thin-film metals: Gold, silver, copper, aluminum, and tantalum [J]. *Journal of applied physics*, 2004, 96(7): 3626-3634.

References

- ⁶⁷ Lawrie B J, Kim K W, Norton D P, et al. Plasmon-exciton hybridization in ZnO quantum-well Al nanodisc heterostructures [J]. *Nano letters*, 2012, 12(12): 6152-6157.
- ⁶⁸ Honda M, Kumamoto Y, Taguchi A, et al. Plasmon-enhanced UV photocatalysis [J]. *Applied Physics Letters*, 2014, 104(6): 061108.
- ⁶⁹ Chen Y, Xin X, Zhang N, et al. Aluminum- Based Plasmonic Photocatalysis [J]. *Particle & Particle Systems Characterization*, 2017.
- ⁷⁰ Miao L, Stoddart P R, Hsiang T Y. Novel aluminum near field transducer and highly integrated micro-nano-optics design for heat-assisted ultra-high-density magnetic recording [J]. *Nanotechnology*, 2014, 25(29): 295202.
- ⁷¹ Nakamura, R., Tokozakura, D., Nakajima, H., Lee, J. G., & Mori, H. (2007). Hollow oxide formation by oxidation of Al and Cu nanoparticles. *Journal of applied physics*, 101(7), 074303
- ⁷² Knight, M. W., King, N. S., Liu, L., Everitt, H. O., Nordlander, P., & Halas, N. J. (2013). Aluminum for plasmonics. *ACS nano*, 8(1), 834-840.
- ⁷³ Chan G H, Zhao J, Schatz G C, et al. Localized surface plasmon resonance spectroscopy of triangular aluminum nanoparticles [J]. *The Journal of Physical Chemistry C*, 2008, 112(36): 13958-13963.
- ⁷⁴ Dahlin A B, Sannomiya T, Zahn R, et al. Electrochemical crystallization of plasmonic nanostructures [J]. *Nano letters*, 2011, 11(3): 1337-1343.
- ⁷⁵ Stangl M, Militzer M. Modeling self-annealing kinetics in electroplated Cu thin films [J]. *Journal of Applied Physics*, 2008, 103(11): 113521.
- ⁷⁶ Pavelescu E M, Jouhti T, Dumitrescu M, et al. Growth-temperature-dependent (self-) annealing-induced blueshift of photoluminescence from 1.3 μm GaInNAs/GaAs quantum wells [J]. *Applied physics letters*, 2003, 83(8): 1497-1499.
- ⁷⁷ Gubicza J, Chinh N Q, Lábár J L, et al. Principles of self-annealing in silver processed by equal-channel angular pressing: The significance of a very low stacking fault energy [J]. *Materials Science and Engineering: A*, 2010, 527(3): 752-760.
- ⁷⁸ Shao L, Tao Y, Ruan Q, et al. Comparison of the plasmonic performances between lithographically fabricated and chemically grown gold nanorods [J]. *Physical Chemistry Chemical Physics*, 2015, 17(16): 10861-10870.

- ⁷⁹ Zhang F, Proust J, Gérard D, et al. Reduction of plasmon damping in aluminum nanoparticles with rapid thermal annealing [J]. *The Journal of Physical Chemistry C*, 2017, 121(13): 7429-7434.
- ⁸⁰ Twardowski M, Nuzzo R G. Chemically mediated grain growth in nanotextured Au, Au/Cu thin films: Novel substrates for the formation of self-assembled monolayers [J]. *Langmuir*, 2002, 18(14): 5529-5538.
- ⁸¹ Rai A, Park K, Zhou L, et al. Understanding the mechanism of aluminium nanoparticle oxidation [J]. *Combustion Theory and Modelling*, 2006, 10(5): 843-859.
- ⁸² Litrico G, Proulx P, Gouriet J B, et al. Controlled oxidation of aluminum nanoparticles [J]. *Advanced Powder Technology*, 2015, 26(1): 1-7.
- ⁸³ Maidecchi G, Duc C V, Buzio R, et al. Electronic Structure of Core–Shell Metal/Oxide Aluminum Nanoparticles [J]. *The Journal of Physical Chemistry C*, 2015, 119(47): 26719-26725.
- ⁸⁴ Schwab P M, Moosmann C, Dopf K, et al. Oxide mediated spectral shifting in aluminum resonant optical antennas [J]. *Optics express*, 2015, 23(20): 26533-26543.
- ⁸⁵ Schwind M, Langhammer C, Kasemo B, et al. Nanoplasmonic sensing and QCM-D as ultrasensitive complementary techniques for kinetic corrosion studies of aluminum nanoparticles [J]. *Applied Surface Science*, 2011, 257(13): 5679-5687.
- ⁸⁶ Ikenoya Y, Susa M, Shi J, et al. Optical resonances in short-range ordered nanoholes in ultrathin aluminum/aluminum nitride multilayers [J]. *The Journal of Physical Chemistry C*, 2013, 117(12): 6373-6382.
- ⁸⁷ Bosman M, Zhang L, Duan H, et al. Encapsulated annealing: enhancing the plasmon quality factor in lithographically-defined nanostructures [J]. *Scientific reports*, 2014, 4: 5537.
- ⁸⁸ Jung Y S, Sun Z, Kim H K, et al. Blueshift of surface plasmon resonance spectra in anneal-treated silver nanoslit arrays [J]. *Applied Physics Letters*, 2005, 87(26): 263116.
- ⁸⁹ Gutierrez Y, Ortiz D, Sanz J M, et al. How an oxide shell affects the ultraviolet plasmonic behavior of Ga, Mg, and Al nanostructures [J]. *Optics express*, 2016, 24(18): 20621-20631.
- ⁹⁰ Cheng F, Su P H, Choi J, et al. Epitaxial growth of atomically smooth aluminum on silicon and its intrinsic optical properties [J]. *ACS nano*, 2016, 10(11): 9852-9860.
- ⁹¹ Martin J, Kociak M, Mahfoud Z, et al. High-resolution imaging and spectroscopy of multipolar plasmonic resonances in aluminum nanoantennas [J]. *Nano letters*, 2014, 14(10): 5517-5523.

References

- ⁹² Handbook of Optical Constants of Solids; Palik, E. D., Ed.; Academic Press, 1985.
- ⁹³ Maidecchi G, Gonella G, Proietti Zaccaria R, et al. Deep ultraviolet plasmon resonance in aluminum nanoparticle arrays [J]. ACS Nano, 2013, 7(7): 5834-5841.
- ⁹⁴ Martin J, Plain J. Fabrication of aluminium nanostructures for plasmonics [J]. Journal of Physics D: Applied Physics, 2014, 48(18): 184002.
- ⁹⁵ Moosmann C, Sigurdsson G S, Wissert M D, et al. Investigating the influences of the precise manufactured shape of dipole nanoantennas on their optical properties [J]. Optics express, 2013, 21(1): 594-604.
- ⁹⁶ Wang H, Goodrich G P, Tam F, et al. Controlled texturing modifies the surface topography and plasmonic properties of Au nanoshells [J]. The Journal of Physical Chemistry B, 2005, 109(22): 11083-11087.
- ⁹⁷ Trügler A, Tinguely J C, Krenn J R, et al. Influence of surface roughness on the optical properties of plasmonic nanoparticles [J]. Physical Review B, 2011, 83(8): 081412.
- ⁹⁸ Cerjan B, Yang X, Nordlander P, et al. Asymmetric aluminum antennas for self-calibrating surface-enhanced infrared absorption spectroscopy [J]. ACS Photonics, 2016, 3(3): 354-360.
- ⁹⁹ McPeak K M, Jayanti S V, Kress S J P, et al. Plasmonic films can easily be better: rules and recipes [J]. ACS photonics, 2015, 2(3): 326-333.
- ¹⁰⁰ Zhang S, Bao K, Halas N J, et al. Substrate-induced Fano resonances of a plasmonic nanocube: a route to increased-sensitivity localized surface plasmon resonance sensors revealed [J]. Nano letters, 2011, 11(4): 1657-1663.
- ¹⁰¹ Nicolas R, Lévêque G, Marae-Djouda J, et al. Plasmonic mode interferences and Fano resonances in Metal-Insulator-Metal nanostructured interface [J]. Scientific reports, 2015, 5:14419.
- ¹⁰² Albella P, Garcia-Cueto B, González F, et al. Shape matters: plasmonic nanoparticle shape enhances interaction with dielectric substrate [J]. Nano letters, 2011, 11(9): 3531-3537.
- ¹⁰³ Raether H. Surface plasmons on smooth surfaces [M]//Surface plasmons on smooth and rough surfaces and on gratings. Springer Berlin Heidelberg, 1988.
- ¹⁰⁴ Fano U. The theory of anomalous diffraction gratings and of quasi-stationary waves on metallic surfaces (Sommerfeld's waves) [J]. JOSA, 1941, 31(3): 213-222.
- ¹⁰⁵ Fleischmann M, Hendra P J, McQuillan A J. Raman spectra of pyridine adsorbed at a silver electrode [J]. Chemical Physics Letters, 1974, 26(2): 163-166.

- ¹⁰⁶ Lin L, Zheng Y. Engineering of parallel plasmonic–photonic interactions for on-chip refractive index sensors [J]. *Nanoscale*, 2015, 7(28): 12205-12214.
- ¹⁰⁷ Shechtman D, Blech I, Gratias D, et al. Metallic phase with long-range orientational order and no translational symmetry [J]. *Physical review letters*, 1984, 53(20): 1951.
- ¹⁰⁸ Vardeny Z V, Nahata A, Agrawal A. Optics of photonic quasicrystals [J]. *Nature Photonics*, 2013, 7(3): 177-187.
- ¹⁰⁹ Khlopin D, Laux F, Wardley W P, et al. Lattice modes and plasmonic linewidth engineering in gold and aluminum nanoparticle arrays [J]. *JOSA B*, 2017, 34(3): 691-700.
- ¹¹⁰ Wiersma D S. Disordered photonics [J]. *Nature Photonics*, 2013, 7(3): 188-196.
- ¹¹¹ Vellekoop I M, Lagendijk A, Mosk A P. Exploiting disorder for perfect focusing [J]. *Nature photonics*, 2010, 4(5): 320-322.
- ¹¹² Vynck K, Burresi M, Riboli F, et al. Photon management in two-dimensional disordered media [J]. *Nature materials*, 2012, 11(12): 1017-1022.
- ¹¹³ Schokker A H, Koenderink A F. Lasing in quasi-periodic and aperiodic plasmon lattices [J]. *Optica*, 2016, 3(7): 686-693.
- ¹¹⁴ Dal Negro L, Boriskina S V. Deterministic aperiodic nanostructures for photonics and plasmonics applications [J]. *Laser & Photonics Reviews*, 2012, 6(2): 178-218.
- ¹¹⁵ Nishijima Y, Rosa L, Juodkazis S. Surface plasmon resonances in periodic and random patterns of gold nano-disks for broadband light harvesting [J]. *Optics Express*, 2012, 20(10): 11466-11477.
- ¹¹⁶ Auguié B, Barnes W L. Diffractive coupling in gold nanoparticle arrays and the effect of disorder [J]. *Optics letters*, 2009, 34(4): 401-403.
- ¹¹⁷ Lamprecht B, Schider G, Lechner R T, et al. Metal nanoparticle gratings: influence of dipolar particle interaction on the plasmon resonance [J]. *Physical review letters*, 2000, 84(20): 4721.
- ¹¹⁸ Humphrey A D, Barnes W L. Plasmonic surface lattice resonances on arrays of different lattice symmetry [J]. *Physical Review B*, 2014, 90(7): 075404.
- ¹¹⁹ Kravets V G, Schedin F, Grigorenko A N. Extremely narrow plasmon resonances based on diffraction coupling of localized plasmons in arrays of metallic nanoparticles [J]. *Physical review letters*, 2008, 101(8): 087403.
- ¹²⁰ Chu Y, Schonbrun E, Yang T, et al. Experimental observation of narrow surface plasmon resonances in gold nanoparticle arrays [J]. *Applied Physics Letters*, 2008, 93(18): 181108.

References

- ¹²¹ Quint S B, Pacholski C. Getting real: influence of structural disorder on the performance of plasmonic hole array sensors fabricated by a bottom-up approach [J]. Journal of Materials Chemistry C, 2014, 2(36): 7632-7638.
- ¹²² Jenkins J A, Zhou Y, Thota S, et al. Blue-shifted narrow localized surface plasmon resonance from dipole coupling in gold nanoparticle random arrays [J]. The Journal of Physical Chemistry C, 2014, 118(45): 26276-26283.
- ¹²³ De Zuani S, Rommel M, Vogelgesang R, et al. Large-Area Two-Dimensional Plasmonic Meta-Glasses and Meta-Crystals: a Comparative Study [J]. Plasmonics, 2017, 12(5): 1381-1390.

Feifei ZHANG

Doctorat : Matériaux, Mécanique, Optique et Nanotechnologie
Année 2018

Fabrication de nanostructures d'aluminium pour la plasmonique dans le visible et l'ultraviolet

L'aluminium (Al) est à ce jour largement considéré comme l'un des métaux les plus prometteurs pour pousser les limites spectrales de la plasmonique vers l'ultraviolet. De plus, l'Al est bon marché, abondant, non toxique et compatible avec la technologie métal-oxyde-semi-conducteur. Dans cette thèse, nous étudions numériquement et expérimentalement l'influence de divers paramètres clés sur les propriétés optiques des nanostructures d'Al. Dans un premier temps, nous étudions la stabilité naturelle des nanoparticules d'aluminium, qui montrent une stabilité d'environ 90 jours lorsqu'elles sont exposées à l'air ambiant. Deuxièmement, nous étudions l'influence du recuit thermique rapide sur les propriétés plasmoniques des nanostructures d'Al. En raison de la réduction du nombre de joints de grains à l'intérieur du métal, une amélioration du facteur de qualité des résonances plasmoniques est trouvée avec un recuit dans des conditions optimales. Troisièmement, nous dévoilons l'effet crucial de la rugosité de surface présente sur les nanostructures lithographiées d'Al. Entre autres, La rugosité de surface provoque la disparition du mode quadripolaire induit par le substrat et l'affaiblissement du mode dipolaire plasmonique. Enfin, nous étudions l'effet de trois types de désordre uniforme (déplacement, taille et rotation sur des structures de types nano-bâtonnets) sur les propriétés plasmoniques de réseaux de nanoparticules d'aluminium. La possibilité d'ajuster leurs propriétés plasmoniques dans le visible et le proche ultraviolet en contrôlant le désordre est étudiée.

Mots clés : aluminium - spectres ultraviolets - plasmons - nanoparticules - oxydation - rugosité - ordre et désordre (physique).

Fabrication of Aluminum Nanostructure for Visible to Ultraviolet Plasmonics

Aluminum (Al) is now widely regarded as one of the most promising metals for pushing the spectral limits of plasmonics towards the ultraviolet range. Additionally, Al is cheap, abundant, non-toxic, and compatible with the complementary metal-oxide-semiconductor technology. In this thesis, we investigate numerically and experimentally the influence of various key parameters on the optical properties of Al nanostructures. Firstly, we study the natural stability of Al nanoparticles, which show about 90-days stability when totally exposed to the ambient air. Secondly, we study the influence of rapid thermal annealing on the plasmonic properties of Al nanostructures. Due to the reduction of the number of grain boundaries inside the metal, an improvement of the plasmonic resonances quality factor is found with annealing at optimal conditions. Thirdly, we unveil the crucial effect of the surface roughness of Al lithographed nanostructures. The surface roughness is found to cause the disappearance of the substrate-induced quadrupolar mode and the weakening of the plasmonic dipolar mode. Finally, we investigate the effect of three kinds of uniform disorder (displacement disorder, size disorder, and rotation disorder) on the plasmonic resonances of Al nanoparticle arrays. The possibility to tune their plasmonic properties in the visible and near ultraviolet range by controlling the disorder is studied.

Keywords: aluminum - ultraviolet spectra - plasmons – nanoparticles – oxidation – roughness - order-disorder models.

Thèse réalisée en partenariat entre :



Ecole Doctorale "Sciences pour l'Ingénieur"